Ernst Plesiutschnig, Dipl.-Ing.

Microstructure improvement of Boron containing 9% Cr martensitic steels

DOCTORAL THESIS

to achieve the university degree of

Doktor der technischen Wissenschaften

submitted to

Graz University of Technology

Univ.-Prof. Dipl.-Ing. Dr.techn. Christof Sommitsch

Faculty of Mechanical Engineering and Economic Sciences

Institute of Materials Science, Joining and Forming

Dr. Master Coline Beal

Faculty of Mechanical Engineering and Economic Sciences

Institute of Materials Science, Joining and Forming

Graz, January 2017

This thesis started in April 2012 and was financially supported by the Austrian Research Promotion Agency (FFG) (Contract Number: 831995) and Böhler Edelstahl GmbH & Co KG.

AFFIDAVIT

I declare that I have authored this thesis independently, that I have not used other than the declared sources/resources, and that I have explicitly indicated all material which has been quoted either literally or by content from the sources used. The text document uploaded to TUGRAZonline is identical to the present doctoral thesis.

Date	Signature

Acknowledgements

I would like to thank a number of people for supporting me within this interesting world of high Cr steels. I am grateful to:

Atousa for her encouragement and patience throughout the countless hours and years.

Christof Sommitsch for having a great time, his guidance, trust and patience to figure the things out the way we wanted to.

Stefan PAUL and Günter Zeiler for the support and the trust in new ideas.

Coline Beal throughout the years.

Horst Cerjak for building confidence on a new topic.

Peter Mayr for being my second assessor and expert.

Rudolf Vallant as an expert and an unresting resource of everything.

Norbert Enzinger as an expert and colleague with a different view.

Stefan Mitsche for his skills on the SEM, his flexibility and realistic estimations.

Bernhard Sonderegger for seeing things from a more kinetic perspective.

Ernst Kozeschnik and his group for creating MatCalc.

Kazuhiro Kimura for exploring different views on Japan and martensitic transformation.

Ernst Gamsjäger and Siegfried Schider for the skills on the laser scanning confocal microscope.

Mihaela Albu for her flexibility and skills at the TEM.

Aleksandra Czyrska-Filemonowicz, Gregorz Cempura for being nice hosts at the AGH in Krakow.

My office colleagues Claudia, Martina, Cecilia, Stojan, Ozan, Christian, Dragan, Johannes, Patrick and Fernando.

The IWS secretary with Manuela, Isabella, Claudia, Sandra and Bettina for organizing.

Last but not least the laboratory with Kurt, Thomas, Gernot, Leander, Herbert, Daniel and Mirjam.

All supportive colleagues and friends for the positive atmosphere at the IWS which made each working day enjoyable.

All my life I've been searching for something
Something never comes never leads to nothing
Nothing satisfies but I'm getting close
Closer to the prize at the end of the rope
All night long I dream of the day
When it comes around then it's taken away
Leaves me with the feeling that I feel the most
Feel it come to life when I see your ghost

Dave Grohl

Abbreviations and Nomenclature

As-heat-treated	AHT
Austenite	γ
Austenite grain size	AGS
Austenite to α or β Ferrite	A_{r3}
Austenite to α-Ferrite and carbide	A_{r1}
Body-centred-cubic	bcc
Body-centred-tetragonal	bct
Cooperation in the field of science and technology	COST
Ductile brittle transition temperature	DBTT
Electron back scatter diffraction	EBSD
Electron energy loss spectroscopy	EELS
Equivalent circle diameter	ecd
European collaborative creep committee	ECCC
Face-centred-cubic	fcc
Heat treatment(s)	HT
High-temperature laser scanning confocal microscopy	HTLSCM
Homologous temperature	T_H
Inverse pole figure	IPF
Kernel average misorientation	KAM
Light optical microscopy	LOM
Martensite	α'
Martensite formed from austenitization	α_1'
Martensite formed after tempering	α_2'
Martensite start temperature	M_s
M_s when cooling from tempering temperature	M_{s2}
Martensite finish temperature	M_f
Materials Calculator (Software)	MatCalc
National Institute of Materials Science (Japan)	NIMS
NIMS Peter Mayr	NIMS-PM or NPM
Orientation-relationship	OR
Prior austenite grain(s)	PAG
Prior austenite grain boundary	PAGB
Prior austenite grain size	PAGS
Sub-grain boundary(ies)	sgb
Ultimate tensile strength	UTS

Transmission electron microscopy	TEM
Quenching and tempering	Q&T
Quenching and partitioning	Q&P
Quality heat treatment	QHT
Residual austenite	RA
Room temperature	RT
Scanning electron microscopy	SEM

1 Introduction

1.1 General

In the world system analysis, Wallerstein [1] explained the historical development of the modern western society and capitalism or capitalist society during the medieval ages of feudalism (9th till 17th century). The feudal crisis (1300-1450 AD) led to the establishment of a capitalist world order with continuous expansion and economic growth through international division of labour determining the interdependencies among regions and labour conditions within these countries […][1].

In Fig. 1, Wallerstein [2] categorizes the world according to socio-economic aspects into four different regions:

a.) Core: The core benefits the most from the capitalist world economy, which led historically to the development of strong central governments, extensive bureaucracies and large mercenary armies [2].
b.) Periphery: Peripheral countries lack of strong central governments, export raw materials to the core countries, rely on coercive labour practices and/or are controlled by other countries [2].
c.) Semi-Periphery: These countries are between core and peripheries, i.e. countries either in decline or attempting to improve their relative position in the world economy. Often these countries exhibit tensions between the government and specific classes of people inside the country. Their limited access to the international banking system and their production of high cost and high-quality manufactured goods fail to predominate in international trade [2].
d.) Other: Some countries maintain their own economic system and tend to remain outside the modern world economy [2].

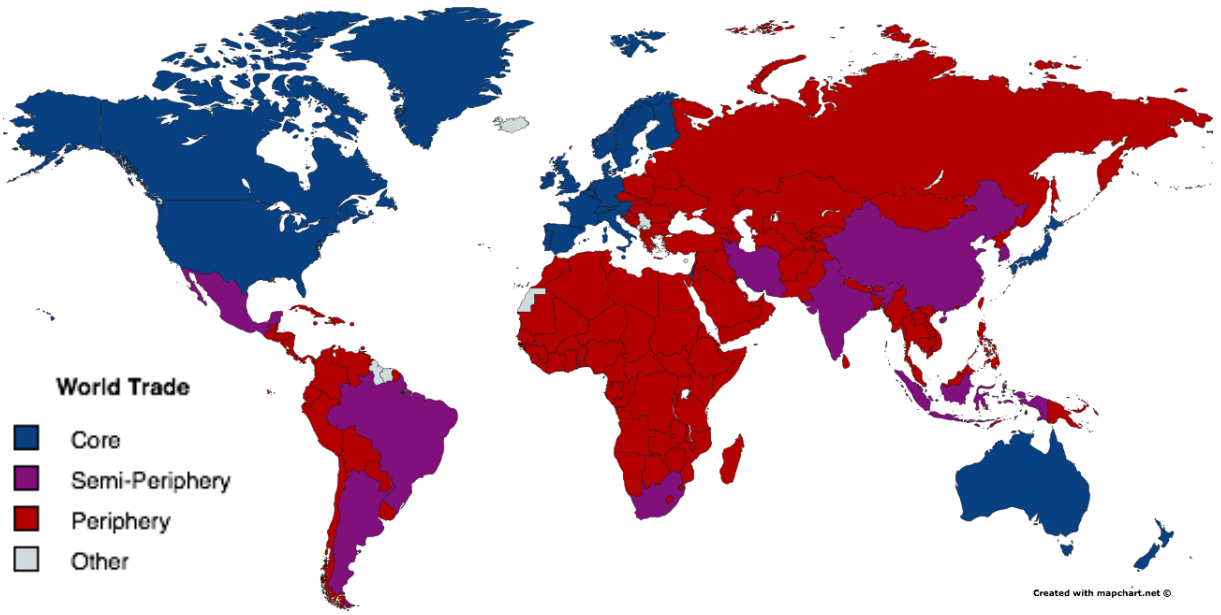

Fig. 1 World System theory [1] dividing the world into Core, Semi-Periphery, Periphery and Other based on a list of [3].

Semi-peripheral countries such as China and India attempt to improve their position in the world economy with economic growth rates above 6 %. Their growth domestic product (GDP), CO_2 emissions and their demand for electric energy grow at much higher annual rates than the global economy, which is depicted in Fig. 2 [4, Fig. 1.9]. A linear growth of traded goods, the GDP, the production of energy, the CO_2 generation and population over the past three decades can be observed. If these growth rates stay constant, it will take 55 yrs to double the population, 40 yrs to double the CO_2 emissions and 38 yrs to double the worlds demand for electricity.

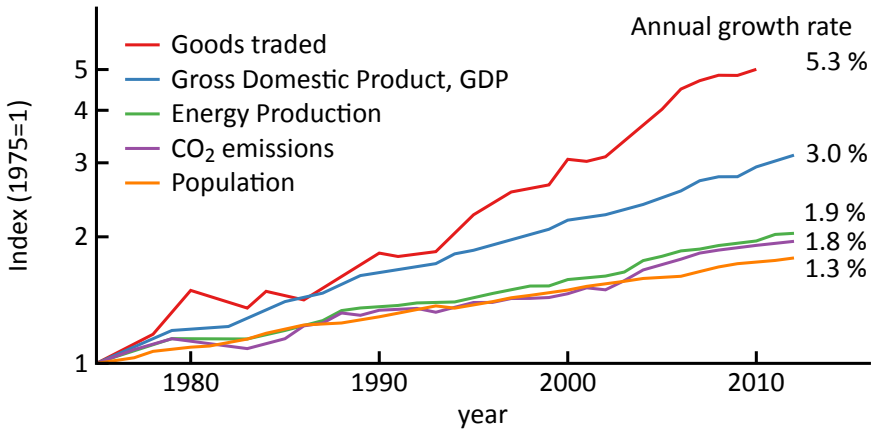

Fig. 2 Annual growth of global trade (in USD), gross domestic product (USD), energy production, CO_2 emissions and population after [4].

Fig. 3 a) shows that 86% of the total energy generated is carbon based. The major part (~70 %) is used for industry and transport (Fig. 3 b)). Coal fired power plants account for the major part of the world's generated electricity. About half of the consumed gas is used for the production of electricity in gas-fired power plants. In combined cycle power plants, the exhaust gas is used to reheat steam in boilers to temperatures up to 700 °C [5], [6]. The higher the temperature and pressure of the steam (with respect to atmospheric conditions), the higher the efficiency and the lower the specific heat rate [kJ/kWh].

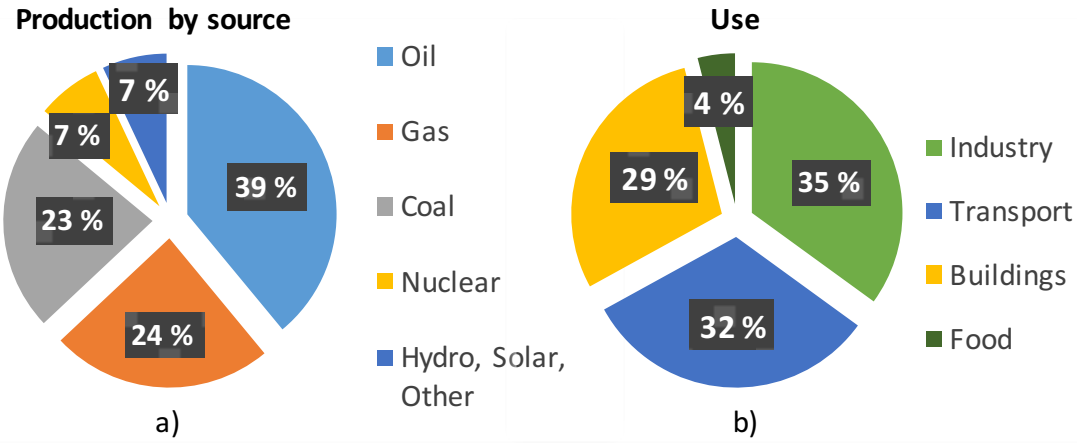

Fig. 3 World energy a) Production, by source and b) Consumption, by use [7].

For operating temperatures up to 650 °C, 9-12 % Cr containing Creep Strength Enhanced Ferritic (CSEF) steels are today chosen as the favoured creep resistant material for rotors in steam power plants due to their price, availability and good creep behaviour. In addition to the creep behaviour, the higher thermal conductivity and the lower coefficient of thermal expansion in comparison to austenitic stainless steels, makes it easier to control tolerances and thermal stresses in service.

1.2 Objectives

The objective of this thesis is to modify the microstructure of 9 % Cr containing heat resistant steels by heat treatment (HT) in order to increase the creep rupture strength. The steels with different HT are creep tested and characterized by metallography and compared to the state of the art.

1.2.1 Major criteria for qualification as a rotor steel

- Creep rupture times $t>10^5$ h up to 650 °C for stresses between 80-100 MPa

- Creep rupture ductility > 10 %
- $R_{p0.2}$>700 MPa at room temperature (RT)
- Impact work (W > 27J) at RT
- Hardenability of thick components
- Weldability
- Ultrasonic testability

1.3 Background information

The present PhD project started in April 2012 and was financially supported by the Austrian Research Promotion Agency (FFG) (Contract Number: 831995) and Böhler Edelstahl GmbH & Co KG with the aim to investigate the microstructure and creep related properties of the latest two variants of B alloyed 9 % Cr steels (NPM1-LN and FB2-2-LN). The suffix "LN" is the abbreviation for low nitrogen and will sometimes be neglected. While the alloying concept of the FB2-2-LN steel is an European COST (Cooperation in the field of Science and Technology) development [8], [9], the NPM1-LN concept is based on the research work of the National Institute of Materials Science (NIMS) adopted and refined by Prof. Peter Mayr [10]–[13]. A brief review of the historical development of this steel class for large scale forgings is provided in Paper IX.

2 Literature

The following literature review introduces HT of steels with some literature on microstructure – property relationships. It contains some basics about the displacive martensitic and reconstructive ferritic phase transformation and related creep and mechanical properties are also provided.

2.1 Heat treatments of steels

Quality heat treatments (QHT) of steels are necessary to achieve desired properties such as prior austenite grain size (PAGS), toughness, hardness or magnetic properties of metals in service [14]. Some of the possible HT of 9 %Cr steels are indicated in Fig. 4. Each QHT for high Cr steels starts with austenitizing above solution annealing temperature to determine the austenite grain size (AGS), to dissolve precipitates and to distribute the elements, which were bound to precipitates. A common QHT is austenitizing and quenching below Martensite finish (M_f) temperature, followed by tempering (Q&T) in the range between 550 - 780 °C [15]. This QHT is also described in the introduction of Paper IV. An austempering process is solution annealing followed by isothermal holding at the desired tempering temperature; ausforming includes hot working of austenite (γ), at temperatures higher than Martensite start (M_s) to influence the microstructure as well as the transformation kinetics of bainitic ferrite [16]–[20]. The QHT used within this study is known as quenching and partitioning (Q&P) and was introduced in 2003 for low alloyed steels [21], [22]. By this HT, the steel is partially quenched to temperatures between M_s and martensite finish (M_f) temperature and directly reheated to tempering temperature. Tamura et al. [23] show an improvement of creep rupture strength of a Grade 91 steel when quenching below M_s before direct reheating to tempering temperature. They reasoned an increased boundary strengthening effect due to a larger number density of MX and $M_{23}C_6$ precipitates along with a larger martensite block size for the improved creep rupture properties.

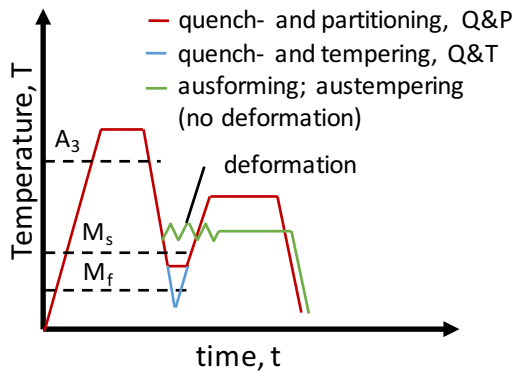

Fig. 4 Four possible HT processes for steels.

Another study [24] shows a negative effect on creep strength of a 9Cr-1Mo steel when selecting the austenitization temperature lower than 1050 °C. The reason for the decreased rupture strength between 850 °C and 900 °C is attributed to the weak ferrite in the microstructure and between 925 °C and 1000 °C to coarse MX precipitates [24]. Yang et al. [25] demonstrate the reduction of the M_s temperature when decreasing the PAGS below 60 µm. Morito et al. [26] show the microstructure related influence of the PAGS on the mechanical properties of a low alloyed steel.

2.2 Martensitic transformation in high Cr steels

The martensitic transformation in high Cr steels is a partitionless allotropic phase transformation [27]. The driving force results from a lack of time and temperature for atomic mobility to rearrange the atoms in the crystal structure of lowest energy. Having enough time, such a rearrangement could be done via nucleation and growth of two or more separate phases from a parent solution phase or without nucleation (e.g. spinodal decomposition) [28]. If the atomic mobility and/or the number of nucleation sites for new phases is limited, magnetic and non-magnetic contributions lead to an increase of the free energy [29, p. 312] with increasing undercooling. This lattice constraint (formation of lattice strain) is indirectly measurable by dilatometry and shows the different thermal expansion coefficients of body centred cubic (bcc)-ferrite and face-centered-cubic (fcc)-austenite (see sec. 2.2.2).

The characteristics of this transformation are [30]:

- Atoms move in the order of atomic distances

- Transformation speed is in the order of phonon velocities (lattice vibrations)
- Atoms move one after another in precise sequence in a so called "military transformation"
- Composition cannot change
- Specific crystallographic relationships between martensite and the parent lattice
- M_s temperature is independent from the cooling rate but dependent on alloying elements and interstitials (mainly C, N).

2.2.1 Thermodynamic point of view

To look at the martensitic transformation for steels in a brief manner from a thermodynamic point of view, Fig. 5 a) draws a quasi-binary system indicating three phases: The solution phase γ, with two product phases α and θ. The system is austenitic (γ), completely solution annealed and in undercooled (close to M_s temperature) state. For each composition x_B the γ line is above the α line, meaning that the chosen temperature in the phase diagram is below the eutectoid temperature and α is the stable phase. The high undercooling limits the diffusion of interstitial and substitutional atoms. With sufficient driving force $-\Delta G_m$ and without changing the composition, the γ phase transforms into martensite (α′) through the martensitic shear transformation as indicated in 1 of Fig. 5 a). An imaginary dotted γ line illustrates the additional driving force necessary (undercooling) to further transform γ into α′. The reason is mechanical stabilisation of γ due to the hydrostatic compressive pressure from the martensitic expansion, which will be illustrated later (Fig. 6 c)). The α′ phase lies on the α line, but is supersaturated with the component B and not in its equilibrium composition. A following temperature increase might trigger the reversion from α′ back to the parent γ phase [31], or cause partitioning of B into the γ, or the nucleation and growth of the (here stoichiometric) θ phase, which is indicated as step 3. This step is accompanied by a further release of internal energy; α′ loses component B moving by relaxing the supersaturated, distorted lattice into the direction equilibrium composition of α, which is additionally illustrated in Fig. 5 b).

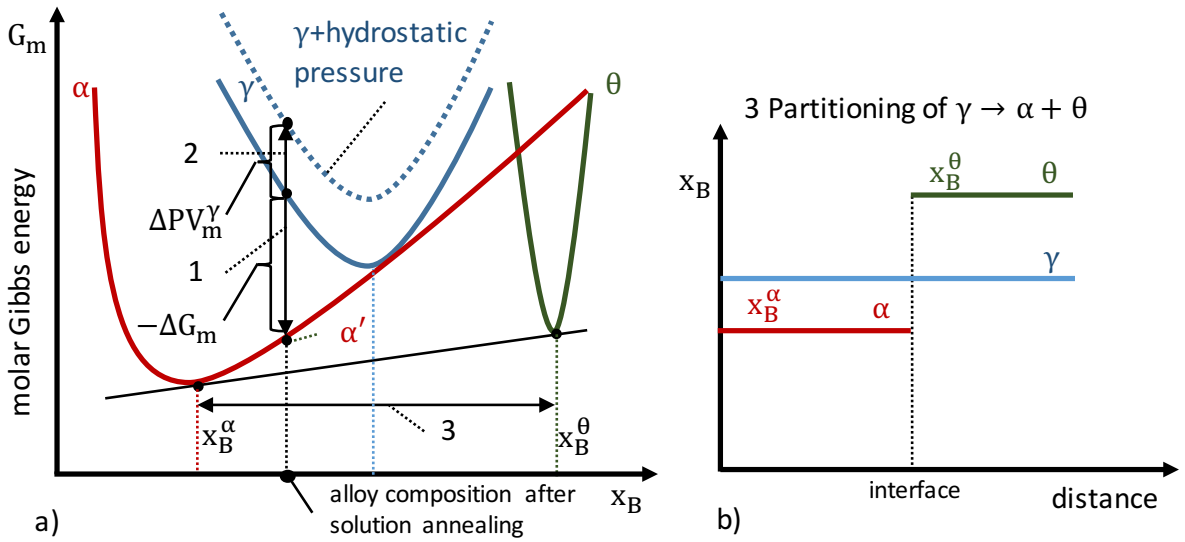

Fig. 5 Schematic illustration of the a) 1 energy decrease of the system when transforming partitionless from $\gamma \rightarrow \alpha'$ and 2 the increasing energy needed (undercooling) to further transform mechanical stabilized γ due to the volume expansion of α'; 3 illustrates in a) and b) the partitioning and growth of the equilibrium composition phases α and θ during annealing after the previous step 1.

During transformation, the stored energy from the constrained γ crystal dissipates into thermal energy (friction), dislocation strengthening (work hardening) due to shape deformation, fine twins, interfaces (lower grain-size) and stored elastic energy [29, p. 121].

2.2.2 Influence of the transformation stress

The reason for the need of subsequent undercooling to form more α' below the M_s temperature during quenching is strain hardening of γ and mechanical stabilization of the RA and is schematically illustrated in Fig. 6 a)-c) [32]. A total volume increase of ~0.7 % causes local plastic deformation of the RA of more than similar amount and elastic compression of all phases inside the transformed volume ($\varepsilon = \frac{V^{\gamma} - V^{\alpha'}}{V^{\gamma}}$) and is indicated in Fig. 6 b). This internal compressive stress is the reason for the measurable residual negative strain (0.18 %) in Fig. 6 a) and the shift of the M_s towards M_f temperature Fig. 6 c).

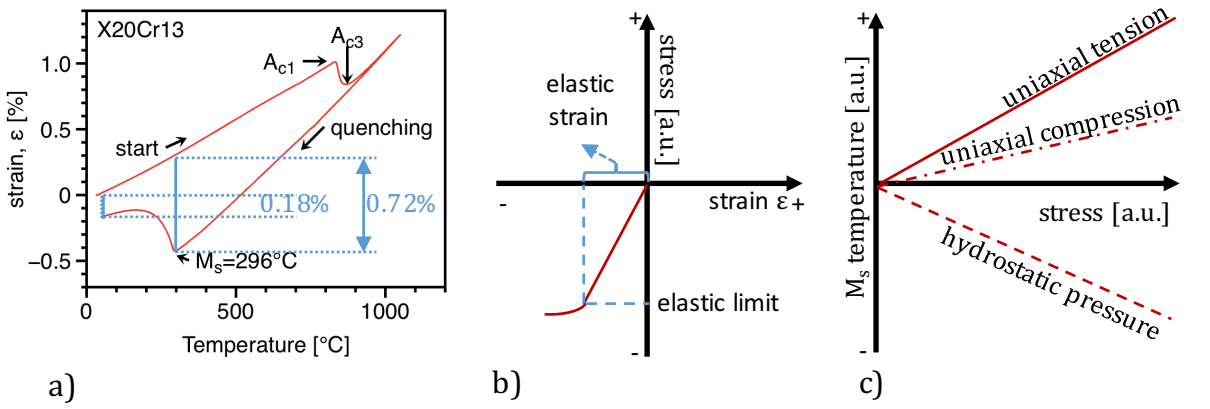

Fig. 6 a) Measured dilatometry curve of X20Cr13 to illustrate the amount of plastic strain and volume expansion, b) Compressive stress which is the reason for mechanical stabilization of deformed RA with the c) Shift of M_s to lower temperatures through hydrostatic pressure [32].

To look at this stress and additional needed undercooling from an atomistic point of view, Fig. 7 illustrates schematically the Lennard-Jones Model with attraction and repulsion forces in a) and the resulting energies in b). If the atoms (here e.g. Fe-atoms) are closer than d_0 towards each other, which is caused by the compressive transformation stress due to martensitic expansion, additional energy is required to proceed with the martensitic transformation [33]. These compressive stresses are responsible and need to be overcome by additional undercooling towards direction M_f temperature. This compressive stress relaxes during subsequent tempering due to the temperature dependent decrease of the elastic limit and the enhancement of diffusional partitioning processes.

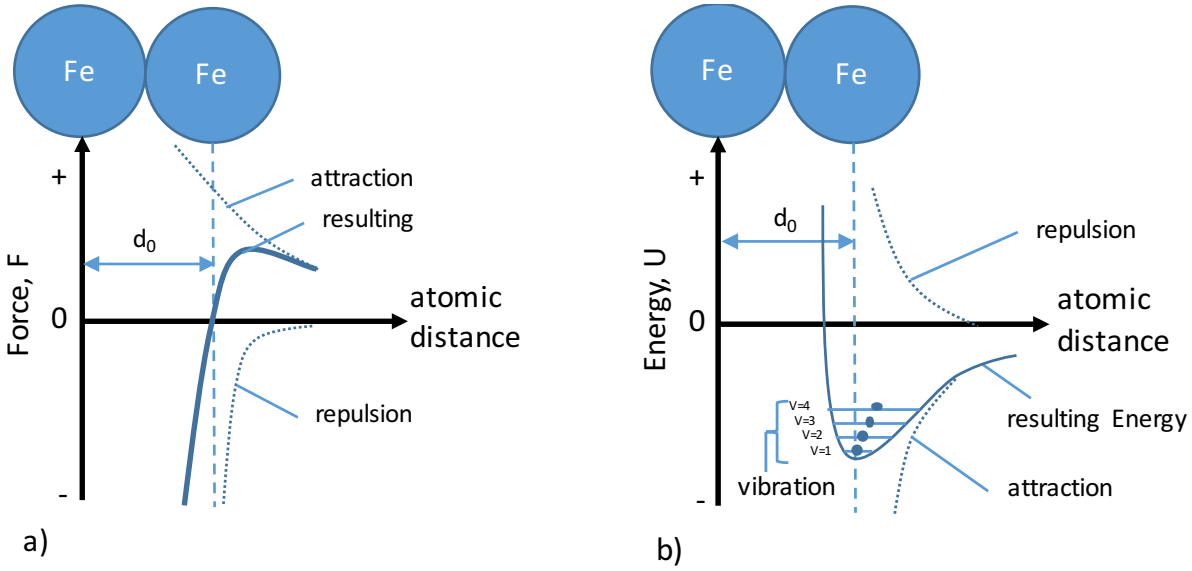

Fig. 7 Lennard-Jones Model for the attraction and repulsion a) forces and b) binding energy of a pair of atoms.

2.2.3 Crystallographic point of view

On cooling the fcc crystal structure below its equilibrium fcc->bcc transformation point (A_{r3} and A_{r1} temperature), γ contracts at larger amount than the bcc crystal structure due to the larger coefficient of thermal expansion, a quantity directly proportional to the atomic binding forces [33]. The reason for the stabilization of the α phase at lower temperatures (below A_3 temperature) is attributed to the ferromagnetism below the Curie-temperature, which stabilizes the bcc crystal structure by compensating the too low cohesive energy [34]. With increasing undercooling, the fcc crystal tries to expand and transform into its equilibrium bcc crystal structure. This sudden volume expansion (Bain strain) at the M_s point is named after Edgar Bain. To fulfil the necessary conditions of an undistorted habit plane between the parent γ and α′, the transformed volume is rotated and periodically slipped or twinned [30]. The sum of the slipped $\{111\}_\gamma$ planes with respect to austenite or $\{110\}_\alpha$ with respect to ferrite is the reason why the habit planes are planes of higher index (e.g. $\{755\}_\gamma$, $\{557\}_\gamma$, $\{575\}_\gamma$). Their index is determined by how much slip is used to correct the shapes of the lath to minimize the strain. The introduced dislocations for slip or twining are not the reason for the high dislocation density of martensite, but the plastic deformation due to the volume change (here ~1%) [29], [30].

The mathematically derived orientation-relationship (OR) with which α′ is formed is described by Kurdjumov and Sachs (KS), though deviations from this OR are reported [35]. This observed OR is only a function of the lattice parameters and parallel close packed planes, which is the reason why the calculated 24 variants stay the same despite variation of the chemical composition. The hierarchical build-up is illustrated in Fig. 8 and summarized in size order (beginning with the largest):

- **Prior austenite grain**
- A **Packet** forms on one single (111) $_{\gamma}$ –plane (4 possible $(111)_{\gamma}$ planes), while each packet consists out of 6 possible variants.
- A **Block** contains in most of the cases 2 variants where one is dominant (size ~8 µm).
- A **Sub-block** is a combination of 2 variants (two specific KS variant groups) with a boundary angle of ~10 deg [36], [37].
- **Martensite lath** interfaces are coherent between lath-lath boundaries. Their misorientation depends on the misorientation of the parent γ and is of low angle (<5 deg).

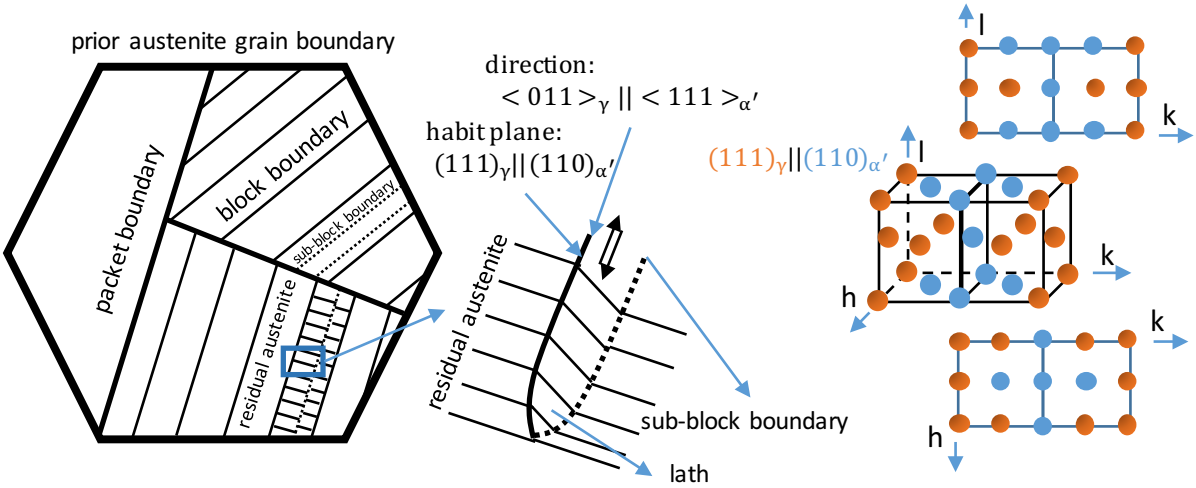

Fig. 8 Hierarchical division of the austenite decomposition starting from the packet till the smallest unit, the martensite lath.

2.2.4 Mechanical properties of martensite

Martensitic transformation is necessary for this class of steels to meet the mechanical requirements (e.g. Charpy-Impact toughness, ultimate tensile strength (UTS)) and to qualify the steel for the application as a rotor. The UTS of this type of steel is a sum of the individual contributions from dislocations (ρ), solid solution (ss), precipitates (p) and grain boundaries (gb) [38], [39]. Precipitation and ss strengthening are due to alloying, while gb and ρ hardening are the result of the martensitic transformation.

$$R_{UTS} = R_e + R_\rho + R_{ss} + R_p + R_{gb} \qquad \text{Eq. 2.1}$$

Yang and Morito [25], [26] show an increase of the packet and block size with an increasing PAGS (gb, ρ strengthening) and related mechanical properties with the M_s point. Yaso et al. [40] show the influence of the austenitizing temperature and the amount of RA on the quenching hardness of an 8 % and a 12 % Cr steel. The smaller the AGS, the lower the M_s temperature; the offset flow stress follows a Hall-Petch type relationship [38], [39].

Dislocation hardening or strain hardening is caused by the volumetric misfit between parent γ and the as-quenched α′. A linear relationship between the C content and the Vickers Hardness is shown [41]. Each ρ generates a visible stress field around the core, which increases the internal energy of an alloy and thus promotes recovery [42]. A recrystallized crystal has a typical ρ between 10^{10} and 10^{12} m/m³. Q&T steels have ρ ~10^{14} m/m³ and as-quenched or cold working steels can have a ρ up to 10^{16} m/m³ [43, p. 87] [41], [44].

Grain boundary hardening (according to Hall and Petch) uses the effect, that the mean path of a dislocation is limited to the dimensions of the grain. Thus, for a constant plastic deformation, small grains require more dislocations than large grains [43]. In α′ the path is limited by the packet and block boundaries [26], [45]. Sub-block boundaries are not immobile [36], [37]. At temperatures $T > T_H \cdot 0.4$ the Hall-Petch effect is not valid and the grain-boundaries do not act as obstacles for dislocation movements anymore. Edge dislocations can change their slip plane by climbing through voids generated on regular lattice positions [43, p. 56]. The increase in internal energy per dislocation and unit length for screw dislocations can be calculated with Eq. 2.2

$$U^{\odot}_{el,screw} = \frac{\mu b^2}{4\pi} \int_{r_0}^{R} \frac{dr}{r} \qquad \text{Eq. 2.2}$$

and with Eq. 2.3 for edge dislocations.

$$U^{\perp}_{el,edge} = \frac{\mu b^2}{4\pi(1-\nu)} \int_{r_0}^{R} \frac{dr}{r} \qquad \text{Eq. 2.3}$$

U_e Internal energy increase due to elastic stress

r_0 core radius of the dislocation

R outer radius of the cylindrical stress field

ν Poisson number

μ Shear modulus

Solid solution hardening: Beside the change of the dislocation structure on alloying, the possible interactions of solute atoms with dislocations are subdivided into two groups: dislocation locking and dislocation friction [46]. Both mechanisms depend on the concentration (c) of the solute atoms and temperature of the deformation [46]. Some of the possible interactions are illustrated here e.g. the parelastic interaction or misfit parameter δ

$$\delta = \frac{1}{c}\frac{a_L - a_M}{a_M} \qquad \text{Eq. 2.4}$$

a_L lattice parameter of the alloy

a_M lattice parameter of the pure metal

c concentration (at%) of the alloying element

with typical values for $|\delta|$ are 0.01…0.1 [43].

The dielastic interaction shows the effectivity of solute atoms according to their lattice bonding forces, the modulus–parameter η

$$\eta = \frac{1}{c}\frac{\mu_L - \mu_0}{\mu_0} \qquad \text{Eq. 2.5}$$

μ_L shear modulus of the alloy

μ_0 shear modulus pure metal

c atomic concentration of the alloying element

with typical values for $|\eta|$ between 0.5 and 1 [43]. From Eq. 2.2 and Eq. 2.3 can be seen, that a larger μ would increase the elastic strain field of a dislocation. A larger μ requires therefore a larger necessary force for dislocation movement.

Particle hardening is distinguished between precipitation hardening and dispersion hardening through their way of creation. Precipitation hardening is created via a solution phase and in most of the cases reversible, while dispersion hardening is irreversible by e.g. oxides and created through e.g. mechanical alloying [43, p. 81].

2.3 Phases in 9-12% Cr steels

Generally, phases are categorized into solution phases, intermetallic phases or stoichiometric intermetallic phases [47]. The solution phase for steels is γ, a stoichiometric intermetallic phase is e.g. M_3C; the intermetallic phases are M_2X (e.g. Mo_2C), $M_{23}X_6$, MX (Nb,V:C,N) of Haegg-type and $(Fe,Cr)_2(W,Mo)$ of Laves type [47], [48]. Their crystal structure and properties is shown in [35]. First principle studies [49], [50] on carbides and Laves phases show their mechanical and physical properties. The dissolution temperatures of these phases are sensitive to the alloying elements in the steels and are simulated with the thermokinetic software MatCalc [51] to help determining heat-treatment temperatures in the experimental part (see sec. 3).

2.4 Ferrite formation

Different from the displacive $\gamma \rightarrow \alpha'$ transformation, the reconstructive $\gamma \rightarrow \alpha$ is nucleation and diffusion controlled [30]. The forming ferrite from the solution phase (γ) (depending on the cooling conditions) is proeutectoid and can be categorized with the Dubé morphological classification according to nucleation sites and appearance [53]. Despite the same appearance and in comparison to Widmanstätten ferrite (nucleating at the PAGB or other grain boundaries [54]), acicular ferrite nucleates upon non-metallic inclusions [53]. Allotriomorphic ferrite refers to crystals with shapes not limited by their own crystal structure whereas idiomorphic ferrite refers to crystals not influenced by adjacent crystals [53]. Additions of only 100 ppm of B can cause the elimination of α morphologies grown from the PAGB. Ab initio calculations show that grain boundary segregation of C and B to the PAGB increase their cohesion by reducing the interfacial energy [55]–[57]. This leads to an increase of the activation energy for heterogeneous nucleation and a shift of the ferrite formation in a TTT or CCT diagram to longer times [57]–[59]. This increases the hardenability of the steels [60]. Other segregating elements such as P, S are embrittling elements but also lower the interfacial energies for ferrite nucleation [56], [57].

Due to the low solubility for the elements C, N, B in α, the reconstructive $\gamma \rightarrow \alpha$ transformation cannot be described without the formation of precipitates. E.g. in plain carbon steels, the reconstructive formation of proeutectoid ferrite is only possible through the segregation of C to e.g. grain boundaries or through the formation of cementite meaning that an area of γ needs to be cleared from C to the solution limit of α before α can grow

reconstructively and almost stress free. This process often starts with the help of a grain boundary. Similar transformation behaviour can also be assumed for the formation of the α phase in high alloyed 9% Cr steels. The dissolution of alloying elements during austenitization inside the γ phase with different affinities to the interstitial elements C or N. This slows down the reaction kinetics for the reconstructive γ → α transformation due to the dependency of precipitate formation. This is incorporated into classic nucleation theory in Eq. 6 where e.g. the nucleation of α can temporarily be blocked by elements, which occupy the nucleation sites (N_{het}). Another possibility is to increase the energy barrier for heterogeneous nucleation ($-\Delta G^*_{het}$) or to increase the activation energy for diffusion to "feed" the embryo ($-E_M$) [54].

$$I_v = C \cdot N_{het} \cdot \nu \cdot e^{\frac{-\Delta G^*_{het}}{kT}} \cdot e^{\frac{-E_M}{kT}} \qquad \text{Eq. 6}$$

I_v is the number of stable nuclei formed in unit time, ν is the Debye frequency, k the Boltzmann constant and the temperature T.

2.5 Creep

Creep is plastic deformation at homologous temperatures T_H>0.3-0.4 at a constant load or stress at strain rates ($\dot{\varepsilon}$) lower than 10^{-5} [s^{-1}]. The international standard ISO 204:2009 defines the valid tolerances and requirements for the measurement and illustration of interrupted and non-interrupted creep tests. The total creep strain ε_{total} after rupture (creep rupture strain) is a sum of three common recognized creep stages, written in Eq. 2.7 and illustrated in Fig. 9 a).

Within the primary stage, dislocations recover and arrange themselves into low angle boundaries (martensite laths and sgb) and form a network and dipoles to minimize the internal strain energy. Eggeler [61] ascribed the end of primary creep to the interruptions of knitting reactions between dislocations and precipitates into sgb.

During the secondary creep regime and after polygonisation of dislocations into subgrains [62], martensite laths and sgb coarse, dislocations move within this network, precipitates coarse, the creep pores orient from isolated cavities to oriented cavities and further to micro-cracks predominantly along the grain boundaries [63], [64]. The secondary creep regime is ended by the tertiary creep regime (acceleration creep region [65]).

Within acceleration creep precipitates ripe, lose their boundary pinning forces and cause the accelerated migration of sgb [10], [33], [61], [65]. The rupture is caused by the creep cavities evolving from micro- to macro-cracks, embrittle the steel by adding three dimensional tensile stress fields and block the movement of dislocations [66, p. 461] [67], [68].

$$\varepsilon_{total} = \varepsilon_{I} + \varepsilon_{II} + \varepsilon_{III} \qquad \text{Eq. 2.7}$$

The creep strain rate $\frac{d\varepsilon_{total}}{dt} = \dot{\varepsilon}_{total}$ is useful to classify creep according to the microstructural degradation mechanism [63]. For values of $\dot{\varepsilon} < 1e^{-10}$ s^{-1}, creep is predominantly governed by diffusion whereas for $\dot{\varepsilon} > 1e^{-10}$ s^{-1} dislocation creep becomes the dominant mechanism [61], [69]–[71].

The Dorn equation (Eq. 2.8) describes dislocation creep in the stress range between $0 < \frac{\sigma}{\mu} < 10^{-3}$ [72].

$$\dot{\varepsilon} = A\frac{D_{eff}\mu\vec{b}}{kT}\left\{\frac{\sigma}{\mu}\right\}^{n} \qquad \text{Eq. 2.8}$$

D_{eff} is the effective diffusivity, σ the stress, $\vec{b}$ the Burger's vector, A is a dimensionless constant and n is the stress sensitivity parameter. n and A are related with $\ln A = -10.5 + 3.4n$ [70], [72]. While A is a material constant and $n = \left(\frac{\partial \ln \dot{\varepsilon}}{\partial \ln \sigma}\right)_{T}$ valid for a constant temperature, it is used to describe the governing mechanism. By combining the dominant microstructural deformation mechanism with the corresponding strain rate ($\dot{\varepsilon}$) and temperature, the deformation mechanism map (after Ashby) in Fig. 9 b) can be drawn [73]. In this map the minimum strain rate ($\dot{\varepsilon}_s$) is calculated as an average within the secondary creep regime [66, p. 440] and taken for comparison. Grain boundary sliding (GBS) is illustrated indirectly in this Ashby map, because each map is valid for a specific grain diameter (here 200 µm). The reason is that grain boundary sliding accounts up to 50 % of the total creep strain [66, p. 445]. The governing creep mechanism can also be roughly estimated by the applied stress divided by the shear modulus for:

- Dislocation creep (dislocation glide $\frac{\sigma}{\mu} > 10^{-2}$; dislocation creep $10^{-4} < \frac{\sigma}{\mu} < 10^{-2}$)
- Diffusional creep ($\frac{\sigma}{\mu} < 10^{-4}$ Nabarro-Herring and Coble creep)

For 9 % Cr steels, the computed solidus temperature with the software [51], [52] is about 1450 °C. Creep exposure at 650 °C with a load of 150 MPa leads to a T_H of ~0.54 and from the Young's modulus of ~220 GPa, the shear modulus (μ_0) is estimated by using the Taylor factor (M) of 2.6 to about 84 GPa, both indicated into Fig. 9 b). Using Eq. 2.8 to predict the $\dot{\varepsilon}$ leads to high activation enthalpies, especially for precipitation strengthened steels [70]. This leads to the idea that not the whole externally applied stress $\frac{\sigma}{\mu}$ contributes to the plastic deformation. Only an effective stress $\frac{\sigma_*}{\mu}$ (the applied stress $\frac{\sigma}{\mu}$ minus a back stress $\frac{\sigma_B}{\mu}$) contributes to the gliding motion of dislocations during creep [74] (see Eq. 2.9).

$$\dot{\varepsilon} = A\frac{D_{eff}\mu\vec{b}}{kT}\left\{\frac{\sigma}{\mu} - \frac{\sigma_B}{\mu}\right\}^n \qquad \text{Eq. 2.9}$$

The measurement of the σ_B is achieved by the technique of small successive applied stress reductions [74]. Dimmler [75] treated the back stress σ_B as a superposition of precipitation, dislocation and sgb hardening. In later works Holzer [61] and Mayr et al. [62] focused on the contribution of precipitates.

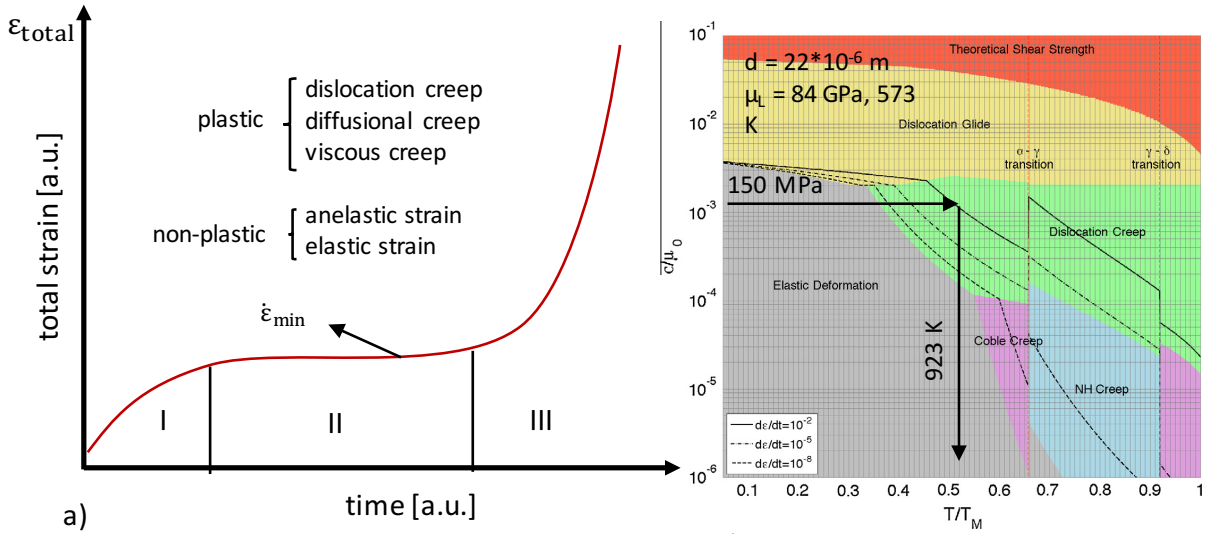

Fig. 9 a) Creep curve and b) Deformation mechanism map [73].

Fig. 10 a) and b) show creep rupture data from different published creep data sheets [76], [77], as well as data from internal laboratory sources at 650 °C. The COST alloy E911, and P92 are already in application. P93 (for pipe) F93 (for forgings) from Sumitomo became 2015 ASTM and ASME qualified [64]. These are some of the current competing materials for future application beside the COST steel FB2-2-LN for the low nitrogen variant

of the NPM1. Fig. 10 b) indicates the stress sensitivity parameter for a variety of 9-13 % Cr steels at 650 °C. The end of Harper-Dorn creep (n=1) is reached above 90 MPa. Below 90 MPa, it is assumed that the ρ does not change with an increasing stress [66]. For applications to last at least for 10 yrs in service, the steels are used within the Harper-Dorn, Coble and Nabarro-Herring creep regime (i.e. diffusion and climb controlled deformation mechanisms). Combining Fig. 10 b) with Eq. 2.9, the $\dot{\varepsilon}$ of the material can be decreased with a decreasing D_{eff} or a higher σ_B.

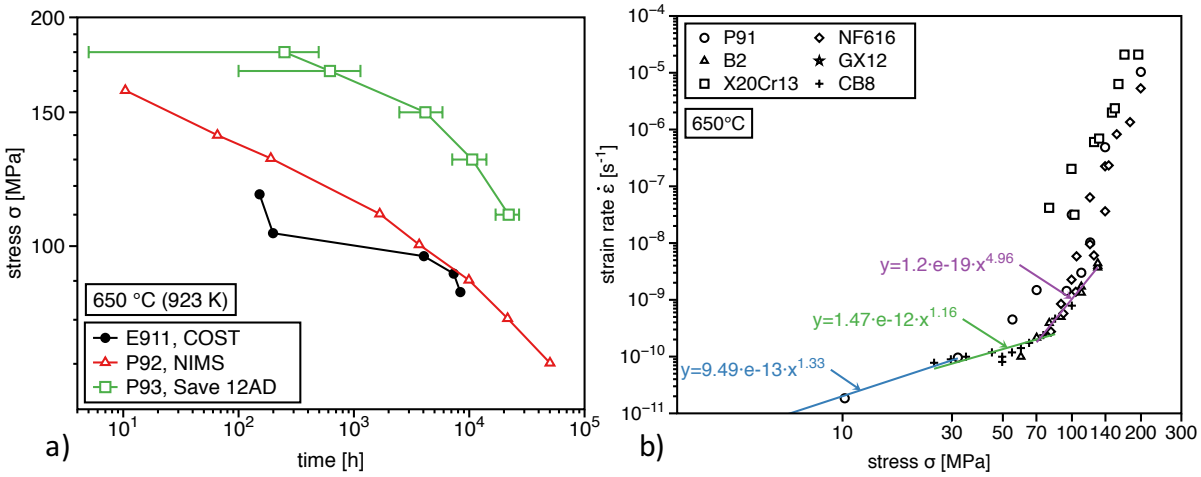

Fig. 10 Creep rupture showing a) creep rupture times for different applied stresses for competing steels [77], [78] and b) strain rate for different applied stresses of different 9-13 % Cr steels.

3 Methods

Subject of the investigations are two chemical compositions of B alloyed 9 % Cr steels (see chemical composition in Table 1), which were produced in 2008 in the course of the last COST project (COST 536). To find out how the shape deformation of martensite influences the transformation kinetics and interacts with carbide formation, a classic 13 % Cr containing X20Cr13 (1.4021) stainless steel is used as a model alloy. In comparison to 9 % Cr steels, this steel has a higher oxidation resistance, does not contain B or N or form precipitates of Laves Phase and MX type.

Table 1 Chemical composition of the investigated steels in wt %.

#	C	Si	Mn	Cr	Mo	W	Co	Ni	V	Nb	N	B	Fe
NPM1-LN	0.07	0.32	0.49	8.9	0.06	2.95	2.84	0.05	0.20	0.05	0.01	0.01	bal.
FB2-2-LN	0.16	0.19	0.31	8.8	1.43	0.05	0.97	0.18	0.21	0.04	0.01	0.02	bal.
X20Cr13	0.21	0.20	0.35	13.3	-	-	-	0.40	-	-	-	-	bal.

Material: Each of the two 9 % Cr compositions was cast to one 3.5 t ingot after a vacuum treatment (see Fig. 11). The vacuum treatment allowed to remove unwanted elements such as Carbon, Nitrogen, Hydrogen and Oxygen and to fine-tune the alloying composition. After the casting, the solidified block was forged and divided into two bars, one round with a diameter of 180 mm (~7 m length) and one quadratic with a width of 240 mm (~3.5 m length). For the round bar it was the final forging step before the preliminary HT and is referred here as the conventional route (C) due to the missing re-melting process (e.g. NPM1-LN-C). The second quadratic bar was used as an electrode for the pressure electro slag re-melting (P) process and was re-melted to a round block with a width of 407 mm. Afterwards the block was forged to a quadratic bar of 250 mm. Compared to the C-route, the re-melting process allows to reduce segregations, non-metallic inclusions, pores etc. to obtain a directional solidified structure at a higher degree of cleanliness. Both routes (C and P) were preliminary heat treated as follows: homogenization at 1050 °C for 5 h plus austenitization at 1100 °C for 3 h, air cooled to room temperature (RT) and tempered at 680 °C for 8 h followed by air cooling to RT.

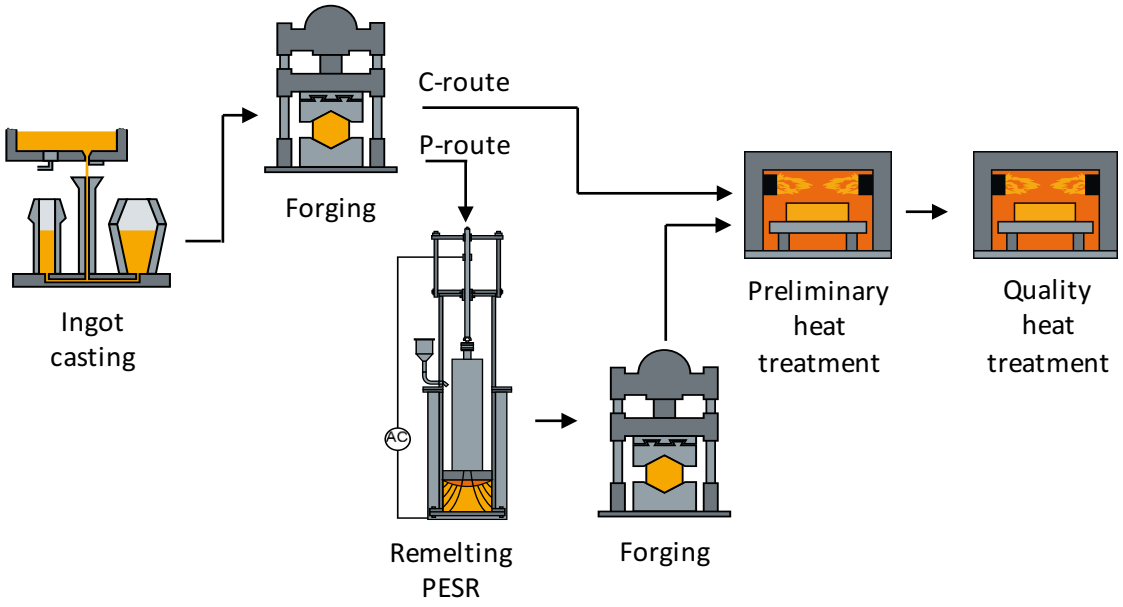

Fig. 11 Casting of the mastermelt to an ingot. The 3.5 t ingot became forged, divided and a) preliminary heat treated (C-route) or b) re-melted with an electro slag under pressure (P-route) before the final forging and HT steps [9].

The preliminary HT are followed by quality heat treatments (QHT) to determine the microstructure before service. The QHT aim to influence the martensitic substructure via the Q&P HT and the PAGS by applying different austenitization conditions, to influence the effective diffusion coefficient D_{eff} and/or the back stress σ_B. To analyse the resulting microstructure-property relationships, basic metallography, dilatometry, simulations and different electron microscopy techniques beside mechanical tests are used.

Initial thermodynamic equilibrium simulations (Fig. 12 a) and b)) are carried out for both steels (see Table 1) to determine the transformation temperatures and solution annealing temperatures for the QHT. The calculations are carried out using the thermocinetic software MatCalc (see sec. 3.6). The M_2B and BN precipitates are not considered. The dominant precipitates within these steels are $M_{23}X_6$, Laves Phase and MX (NbC and VN). According to the simulation, the dissolution temperature of Laves Phase in NPM1-LN is ~800 °C while for the FB2-2-LN this temperature is lower ~700 °C. The dissolution temperature for the MX and $M_{23}X_6$ precipitates is in the austenitic region, for both steels between 1100 °C and 1200 °C. The higher Si content of NPM1-LN stabilizes the carbide phase M_6C between the A_1 and A_3 temperature.

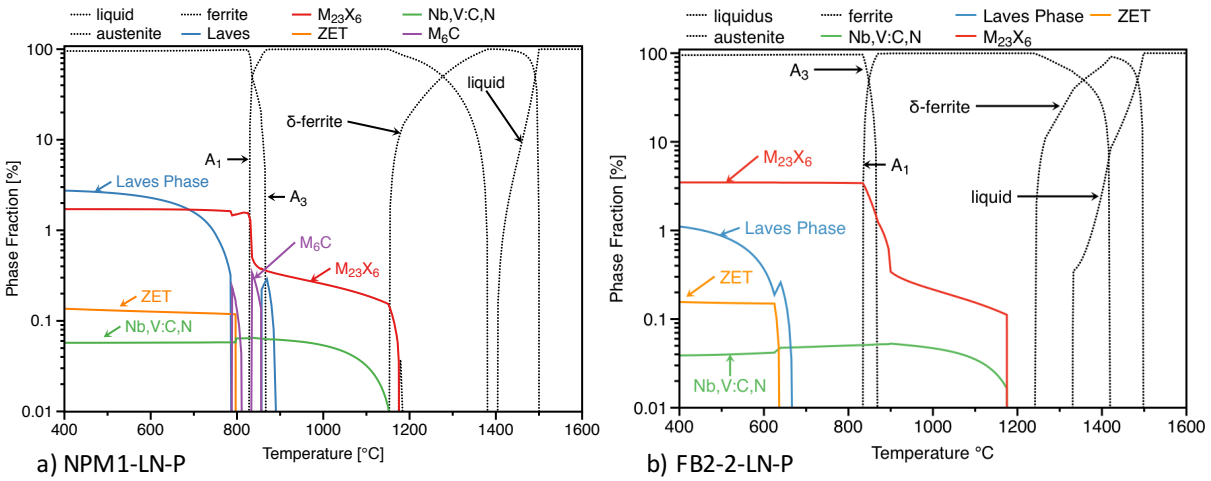

Fig. 12 Equilibrium phase fraction diagram of a) NPM1-LN and b) FB2-2-LN.

3.1 Dilatometry

Phase transformation temperatures are measured with an inductive quenching dilatometer DIL 805A/D [79]. The device offers a length resolution of 50 nm per 0.05 K with heating and cooling rates larger than 1000 Ks^{-1}, depending on the geometry of the specimen. Unless otherwise described, in this work standard cylindrical specimens are used with a nominal diameter of 4 mm and a nominal length of 10 mm.

Heating rates between 1-8 Ks^{-1} with cooling rates between 3-5 $t_{8/5}$ min time (measured time when the specimen cools from 800 °C to 500 °C) are used to determine the rate independent transformation points (A_1, A_3). A deviation from the linear tangent in the order between 2 % and 5 % of the transformed amount is considered as the transformation point.

The preliminary dilatometry experiments to determine the quenching temperatures for the Q&P HT of the creep specimen are carried out with different parameters. The amount of the RA is evaluated by fitting the derivative of the elongation according to the temperature above the temperature, though simpler evaluations by with the lever rule (see Paper VI) or Koistinen-Marburger (K-M) exist [80] [81]. The austenitization temperature of 1150 °C (selected from MatCalc calculations) and a linear heating rate of 20 Ks^{-1} with a logarithmic cooling from 800 °C to 500 °C in 20 min time is selected. The quenching temperature were 65 % of the martensite is formed is chosen from the P-route of each steel.

3.2 Heat treatment

The QHT applied to the steels are the standard Q&T [15] HT, and a Q&P [21] HT, both followed by two times tempering. Fig. 13 schematically shows the applied QHT - the red dots indicate the variation of temperature and time. Most of the applied HT within this thesis were carried out with the furnace from Nabertherm [82]. Fig. 14 a) depicts the furnace chamber and Fig. 14 b) shows the natural cooling rates (closed door) measured on two rectangular shaped specimens (dimensions: 20x20x100 mm) at the top and bottom of the furnace.

The furnace temperatures are controlled by the furnace thermocouples while it was not possible to monitor the heating and cooling rates of the specimens directly because they needed to be transferred into different preheated furnaces during the HT.

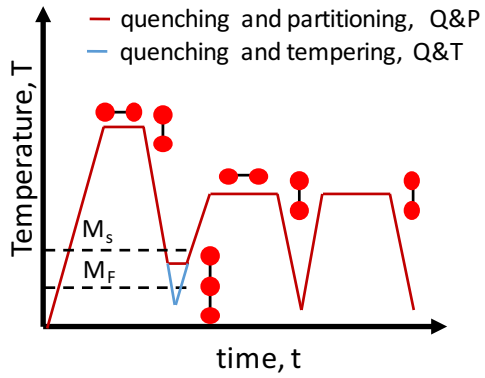

Fig. 13 HT applied on the investigated steels.

The austenitization temperatures and times were chosen at 1100 °C and 1150 °C for 30 min and 180 min to provide a good solution and distribution of elements to not inhibit the austenite grain growth by e.g. MX or $M_{23}X_6$ precipitates [83]. Table 3.2 summarizes the applied HT for the NPM1-LN and the FB2-2-LN steels. The selected quenching temperatures for the creep tests were room temperature (RT), 360 °C for NPM1-LN and 323 °C for FB2-2-LN followed by two times tempering at 700 °C for 3 h. The variation of the austenitization temperature, time and finally the quenching temperature at 2 different values leads to 8 different HT per steel. Two times tempering at 700 °C for 3 h is necessary for stress relieving and to transform the RA into α′ during cooling from the first tempering step and to temper this initially formed α′ during the second tempering step.

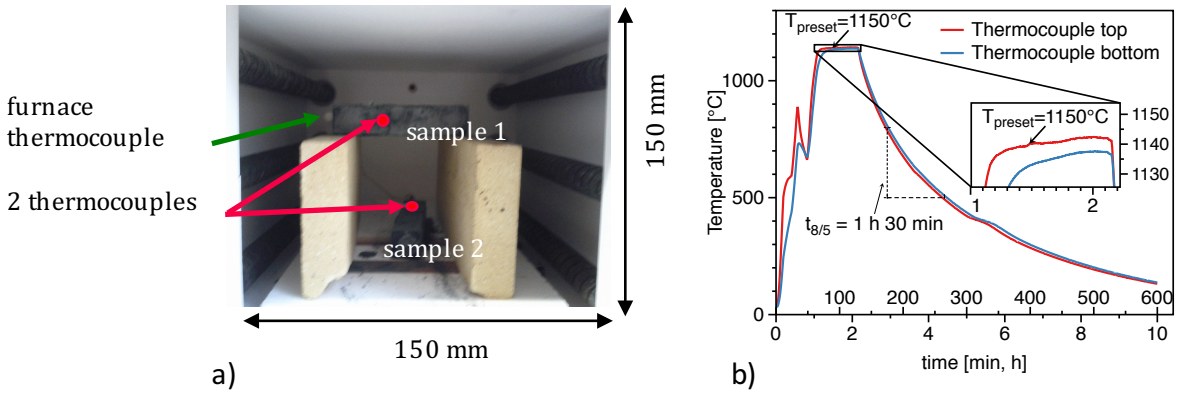

Fig. 14 a) Nabertherm furnace and b) characteristic natural cooling rate expressed as $t_{8/5}$ value.

The **prior austenite grain size** (PAGS) is measured on dilatometry specimens after the different austenitization conditions (see the first row of Table 3.2). After austenitization and quenching, the specimens are etched and evaluated with light optical microscopy (LOM). As an etchant for the PAGB 80 ml picric acid with 20 ml of Ethanol and 800 mg of Cu_2Cl is used. The etchant is mixed and heated to 50 °C and the specimen dipped for 1 min into the etchant [84]. The best results for the PAGB are observed on etching the samples after polishing and a 2 d rest inside the desiccator.

Table 3.2 Overview of the performed heat treatments for comparative interrupted creep tests.

	HT 1	HT 2	HT 3	HT 4	HT 5	HT 6	HT 7	HT 8
Austenitization,	1100 °C 30 min	1100 °C 30 min	1100 °C 180 min	1100 °C 180 min	1150 °C 30 min	1150 °C 30 min	1150 °C 180 min	1150 °C 180 min
quenching temperature	quenched to RT	quenched below M_s	quenched to RT	quenched below M_s	quenched to RT	quenched below M_s	quenched to RT	quenched below M_s
tempering	2 times 3 h at 700 °C	2 times 3 h at 700 °C	2 times 3 h at 700 °C	2 times 3 h at 700 °C	2 times 3 h at 700 °C	2 times 3 h at 700 °C	2 times 3 h at 700 °C	2 times 3 h at 700 °C

Calculation of the PAGS: The austenite grain growth can also be calculated by using the Alberry and Jones equation (Eq. 3.1) [85], [86]

$$D_t^2 - D_{t_0}^2 = Cte^{-\frac{Q_c}{RT}} \qquad \text{Eq. 3.1}$$

where t refers to the time, C is a constant and Q_c is the activation energy. The PAGS can be converted into the ASTM number [66, p. 191].

3.3 Mechanical testing

Standard Vickers hardness-, tensile- and Charpy-V impact tests [87] are carried out for selected specimens after different HT and after the creep rupture tests to show the influence of the HT on the mechanical properties to further relate them to the microstructure.

3.3.1 Creep testing

To find the best HT for the best performance of the steels during the creep tests under service conditions, comparative creep rupture tests are carried out at 650 °C. The specimens are mounted in a multi-specimen creep furnace as schematically illustrated in Fig. 15. The plastic deformation of the specimen is measured on interrupting the test (cooling to RT and disassembly) - between the two measuring edges (Fig. 15 c).

For technical creep tests the load F during the entire test time is kept constant. Hence, the physical stress σ throughout the creep test is not constant, due to the decrease of the cross-sectional area of the specimen (corrosion, plastic strain, cavity formation etc.).

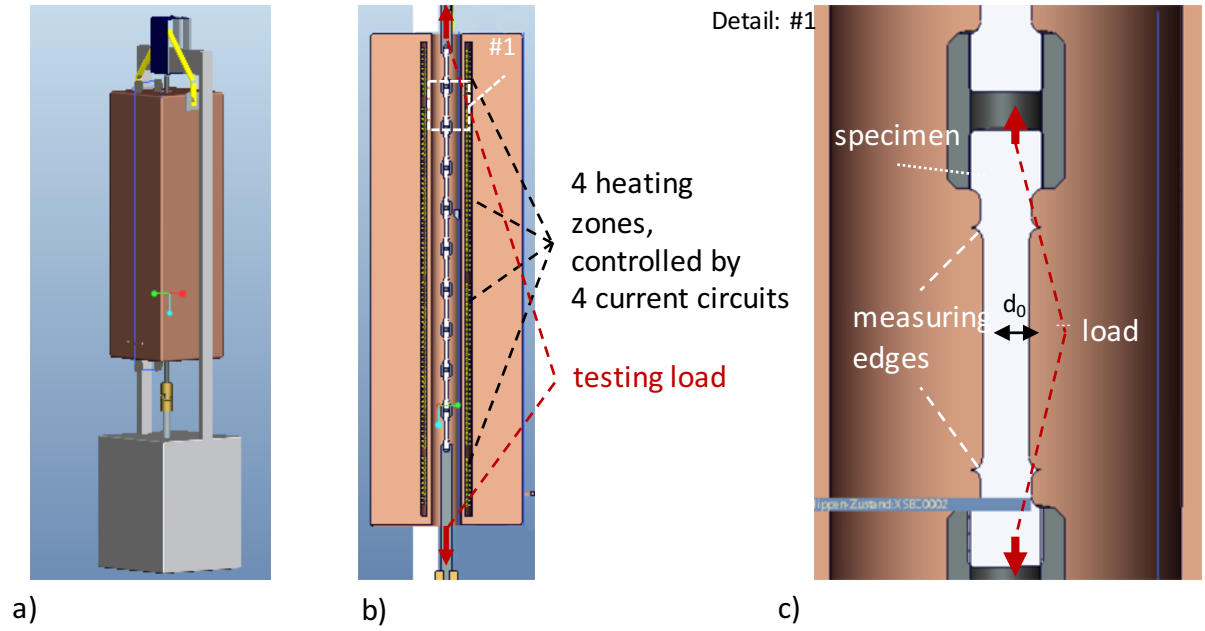

Fig. 15 a) Multi-specimen creep furnace for interrupted creep tests with the b) sectional drawing with c) detail of a mounted creep specimen inside the furnace.

The accuracy of the interrupted measuring method is monitored since 2003 and plot in Fig. 16. According to the internal calibration curve from 2012 (beginning of this project) the standard deviation of this method is ±6 µm, which is indicated as the upper- and lower control limit (UCL and LCL). The reason for the jump in accuracy is the newly installed measurement table and the improved camera equipment.

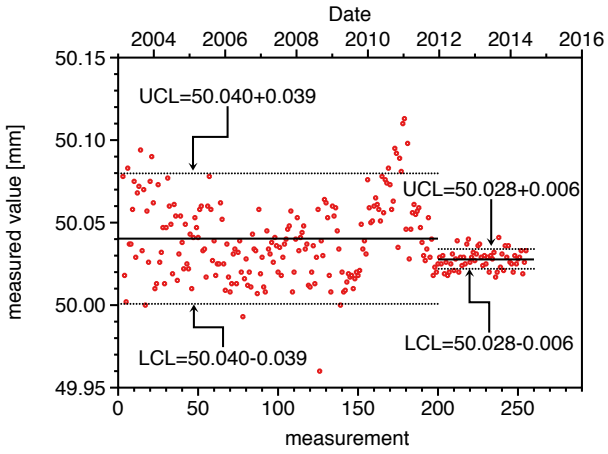

Fig. 16 Control chart for the calibration of interrupted measurements from creep testing with the mean value, the upper and lower control limits of one standard deviation of a standard test specimen.

These furnaces are used to test the influence of the HT in Table 3.2, at a temperature of 650 °C and a load F of 5 886 N with a nominal specimen diameter of (d_0=7.068 mm) corresponding to an initial stress level of 150 MPa. After these tests, further creep rupture

tests are carried out in the framework of ECCC (European Collaborative Creep Committee) at stress levels ranging between 100-150 MPa at temperatures between 625 – 675 °C in order to be able to create an engineering extrapolation (e.g. Larson-Miller parameter method [66]).

3.4 X-ray diffraction

X-ray diffraction (XRD) experiments at high temperature are carried out to detect phase transformations and to compare surface sensitive methods with volume sensitive results from dilatometry experiments. A Siemens D5005 diffractometer in the Bragg-Brentano theta-theta geometry and equipped with a high-temperature oven chamber HTK 1200 from Anton Paar GmbH is used. The HTK 1200 guarantees an excellent uniformity of the sample temperature due to its environmental heating chamber. A Cu K_{α}X-ray source operating with a generator voltage of 40 kV at a current of 40 mA allows measuring the phase transformations in dependence of the temperature. Argon at a pressure of 1 Pa is used to prevent the specimens from oxidation. The diffraction spectra are evaluated with the Diffrac. suite EVA-software from Bruker. The height displacement function of this software is used to correct the temperature dependent peak shifts. For each spectrum the specimen needs to be isothermally hold. Therefore, different specimens are used to record the spectra during heating and cooling, to exclude the measuring time during heating from the measurements during cooling.

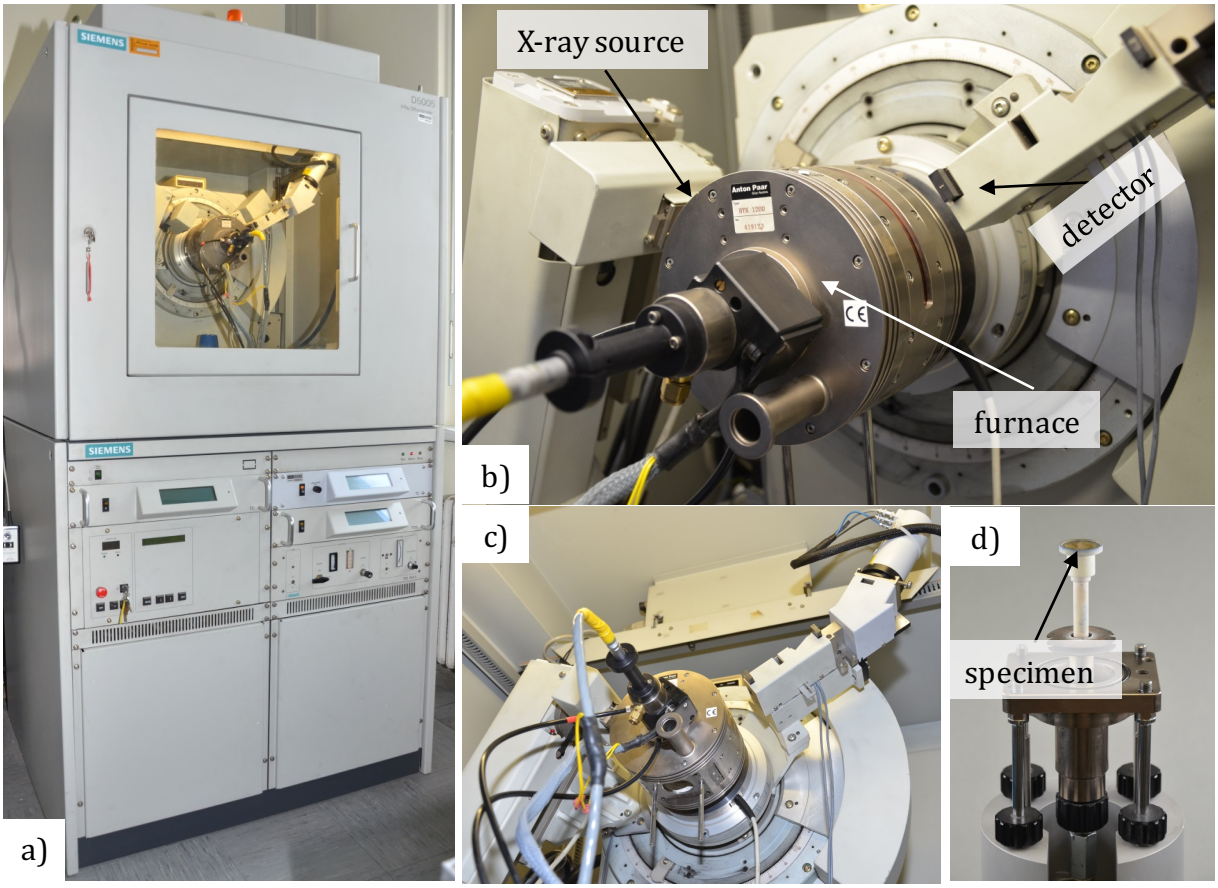

Fig. 17 a) Siemens D5005 diffractometer with the mounted b)-d) high-temperature oven chamber HTK 1200 from Anton Paar [88].

3.5 Microscopy

Beside conventional LOM and stereo microscopy experiments on etched and un-etched specimens, different methods of electron microscopy and high-temperature laser scanning confocal microscopy (HTLSCM) are used.

The etching procedure for the PAGB measurement is described in sec. 3.2. For the detection of creep pores, the longitudinal section of the creep ruptured specimen is mechanically polished and evaluated with LOM and ImageJ [89].

3.5.1 High-temperature laser scanning confocal microscopy

Fig. 18 a) depicts the Yonekura VL 2000 DX HTLSCM equipped with an SVF 17 SP which is used to observe microstructural changes of the Q&P HT (Fig. 18 b)) at the surface in-situ. The HTLSCM was invented by Minski in 1961 [90]. A review about the technique is provided by Sohn et al. [91]. The HTLSCM can be used to observe surfaces of samples

till temperatures up to 1650 °C [92]. The gold coated double elliptic mirror furnace enables heating rates of several 50 Ks^{-1}. The frame rate of 15 frames per second even enables the observation of dynamic processes at different temperatures or heating rates [92]. The microstructure is revealed by thermal etching [92]. A phase transformation becomes visible due to local changes in the position of the illuminated surface as a result of local contraction or expansions of the underlying grain segment undergoing a phase transformation [92]. For this experiment, one sample of a X20Cr13 stainless steel is subjected to the thermocycle in Fig. 18 b) for the experiment due to the higher Cr content, relative better oxidation resistance and simpler precipitation due to the lower number of alloying elements behaviour.

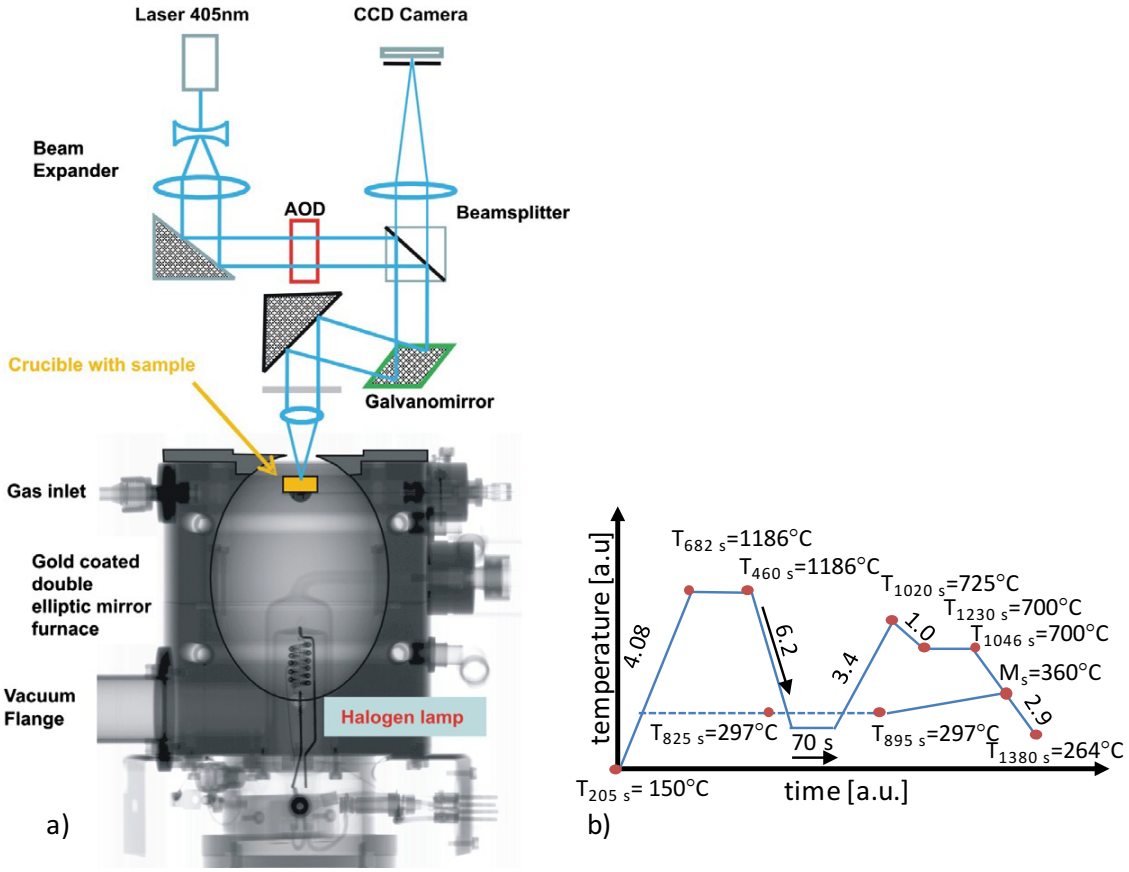

Fig. 18 a) Schematic sketch of HTLSCM Yonekura VL 2000DX and mirror furnace SVF 17 SP [92] and b) HTC applied on the X20Cr13 specimen.

3.5.2 Scanning electron microscopy

Most of the scanning electron microscopy (SEM) investigations are performed on a Zeiss Ultra 55 field emission gun equipped with a Thorlabs fast frame rate scientific camera for electron back scatter diffraction (EBSD) and an Octane super 60 mm^2 silicon drift

detector for energy dispersive X-ray spectrometry (EDXS). To investigate the size and phase fraction of precipitates, EDXS mappings for selected elements are recorded applying a typical acceleration voltage of 10 kV and a beam current of 5.8 nA using the Genesis software V6.5 from EDAX. The images are further processed to evaluate e.g. the area fraction of precipitates with the software ImageJ [89].

EDX-maps are carried out for both, the NPM1-LN-P and FB2-2-LN-P steel for the elements Fe, Cr, Mo, W, Si and C on an area of 25x20 µm for each map. The precipitates are compared in AHT stage and after creep exposure for two different austenitizing conditions (1100 °C and 1150 °C for 30 min), at two different PAGS of 50 µm and 300 µm. Fe is used to evaluate the total area fraction of precipitates. The areal resolution limit to detect contrasts with the software [89] is chosen to be 0.01 μm^2 for the applied raster step size of 50 nm within the SEM, which is too low to detect MX precipitates.

At the same microscope, comparative EBSD experiments are carried out for the Q&T and Q&P HT, (HT5 and HT6 in Table 3.2). The EBSD patterns are recorded with an acceleration voltage of 20 kV, a beam current of 9 nA and analyzed with the OIM-SoftwareV7.3 [93]. This software allows to evaluate e.g. the misorientation of kernels and to predefine the kernel size (Fig. 19). For example, if the step-size of the SEM is set to 100 nm and the 3^{rd} nearest neighbours (NN) is selected, the software calculates the deviation from the kernel center to the average 3^{rd} NN (see Fig. 19). The reference value is the arithmetic mean of the investigated kernel. Measuring points exceeding the predefined maximum misorientation angle are excluded from the evaluation. It is shown that KAM is proportional to the hardness [94], to the amount of plastic deformation and total dislocation density [95].

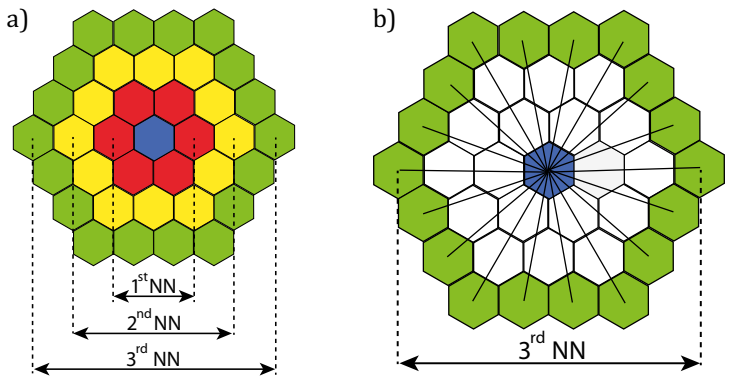

Fig. 19 Schematic illustration of kernels indicating different nearest neighbours (NN) used for KAM evaluations.

3.5.3 Transmission electron microscopy

The transmission electron microscopy (TEM) experiments are conducted with a FEI Tecnai F20 and a FEI Tital2G microscope. For both devices the necessary sample preparation steps are different and are described in detail [96]. Generally, two preparation techniques, dimpling and Focused Ion Beam (FIB) milling are used.

Dimpling: The steel specimens are cut, grinded and polished manually to a thickness below 100 nm. Discs with a diameter of 3 mm are stamped from these specimens and dimpled to 50 – 70 µm. Afterwards, the sample is ion polished until a hole in the specimen appears. In the vicinity of the hole, thin parts of the steel specimen become transparent for electrons, which are subject of the investigations.

FIB: A Dual Beam FIB-SEM FEI Nova200 [97], [98] is used to extract a single TEM lamella from the X20Cr13 steel specimen after subjecting the HTLSCM experiment. For atomic resolution, the specimen was milled with Ga^+ Ions to a thickness lower than 50 nm.

FEI Tecnai F20: For non-atomic resolution, bright field-, energy filtered TEM- imaging, electron beam diffraction, X-ray- and EEL- spectroscopy are performed using a monochromator, an Si(Li) X-ray detector and a high resolution Gatan Imaging Filter (GIF) which can be operated in both normal and scanning mode [99].

FEI Titan2G 60-300 kV: The specimen subjected to the HTLSCM experiment is used to produce images at atomic resolution. To prepare this specimen for TEM and Scanning TEM (STEM) investigations, FIB milling in a preliminary defined region is used, which was before identified by SEM measurements. The FIB lamella is approximately 8 x 4 µm large and 150 nm thick. In order to further thin the lamella to a thickness of about 50 nm and

to remove the formed amorphous layer on the surface, two subsequent low energy Argon milling post – treatments at 900 eV (56 μA at ±10 ° and each side 15 min) by using the NanoMill device is performed. Very thin regions on top of the specimen (20–40 nm) are used for imaging and analytical investigations. For atomic resolution imaging on the microscope and analytics in scanning mode, a probe aberration-corrected microscope, equipped with X-FEG Schottky field-emission electron source, FEI Super-X detector (Chemi-STEM technology) consisting of four separate silicon drift detectors [100] and Dual Electron Energy Loss Spectroscopy (EELS) - Gatan Imaging Filter (GIF) Quantum [101] is used [99].

3.6 MatCalc simulation

Equilibrium and kinetic simulations with the thermokinetic software MatCalc are carried out using Version 5.62 (rel. 1004) with the thermodynamic database mc_fe_v2.039.tdb and kinetic database mc_fe_v2.005.ddb [51], [52]. The software comes with many build-in physical models and allows the adjustment of parameters such as the dislocation density or the shape of the precipitates. To setup the calculation, main parameters such as the precipitates type, nucleation sites of the precipitates, transformation points and HT are used.

To study the nucleation and evolution of M_3C carbides at dislocations and interfaces such as the PAGB, the sgb and dislocations for X20Cr13 steel at annealing temperature during the HTLSCM experiments, simulations are carried out for a completely transformed α' matrix with a constant dislocation density (5e14 $\frac{1}{m^2}$ [44]) and a deformed γ matrix with different dislocation densities ranging between 1e14 – 1e15 $\frac{1}{m^2}$.

4 Results

Beside the results published in the papers, most of the unpublished results are shown here. The results are structured to start with dilatometry tests followed by mechanical tests and microscopy investigations.

4.1 Phase transformation of NPM1-LN and FB2-2-LN

To determine A_{c1}, A_{c3}, M_s and M_f as well as the quenching temperatures for the Q&T and Q&P HT, dilatometry tests with different heating and cooling rates are performed. Fig. 20 a) and b) show dilatometry curves for the NPM1-LN-C (Fig. 20 a)) and FB2-2-LN-C (Fig. 20 b)) steels, respectively. The lower coefficient of thermal expansion of the bcc lattice of ferrite (tempered martensite) is seen when heating from RT to A_{c1} temperature. After complete recrystallization at A_{c3} temperature, the slope is steeper and corresponds to the thermal expansion of the austenite. Undercooling with the critical cooling rate from austenitizing temperature, the fcc crystal becomes unstable and austenite transforms at M_s temperature diffusionless into body centred tetragonal (bct) martensite.

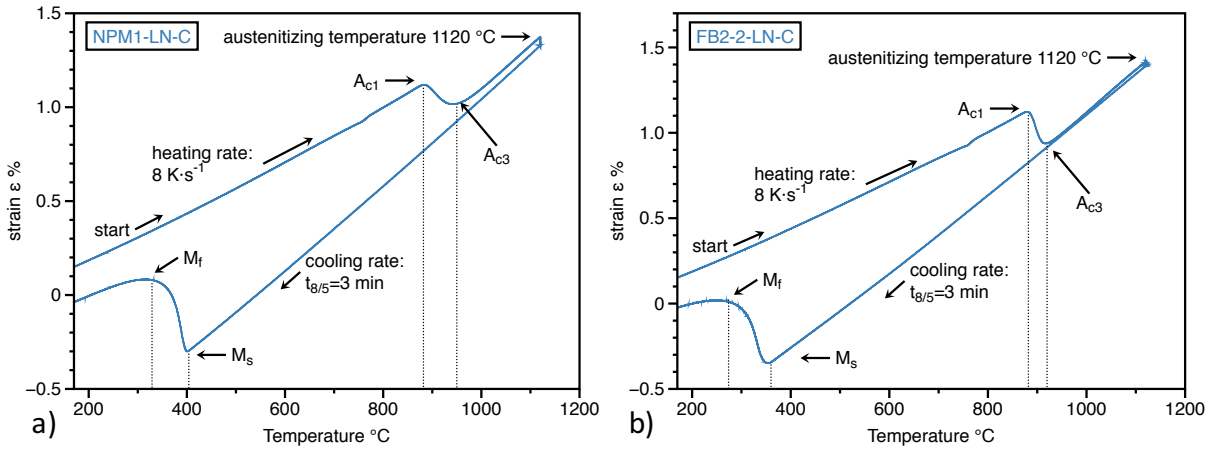

Fig. 20 Comparative dilatometry curves of a) NPM1-LN-C and b) FB2-2-LN-C for similar heating- and cooling rates.

The influence of the heating and cooling rates on the transformation points is shown in Fig. 21 and Fig. 22. For FB2-2-LN-C in Fig. 21, the extracted transformation points are fit to a power law and the factor in front is the transformation temperature at a heating

rate of x=1 Ks^{-1}. The simulated equilibrium transformation temperatures for the FB2-2-LN are A_1=833 °C and A_3=866 °C, which are at reasonable values when the heating rate moves towards 0 (see Fig. 21 a)). Below the critical cooling rate the M_s temperature does not change; the transformed amount depends on the temperature, the size and geometry of the specimen [30]. Fig. 21 b) shows the evaluation of the M_s temperature which is ~360 °C.

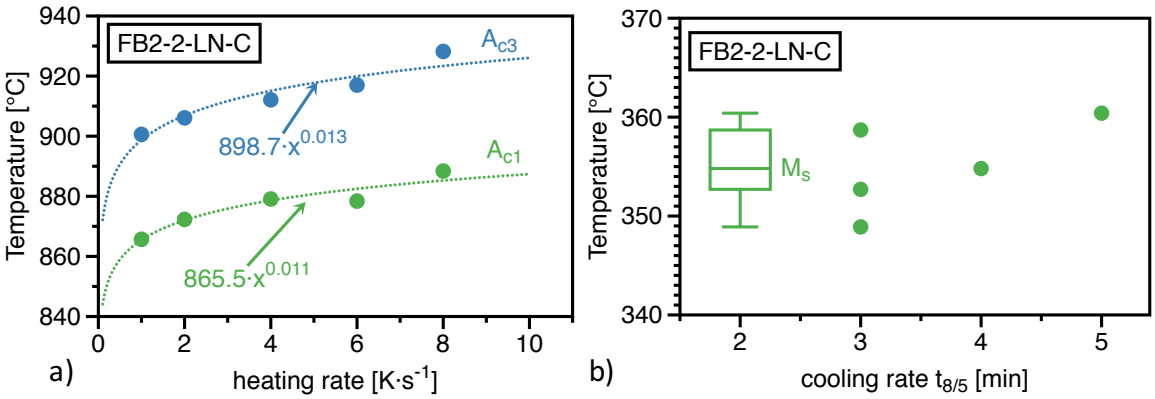

Fig. 21 Influence of a) heating rate on A_{c1} and A_{c3} temperatures and b) cooling rate, here expressed as different $t_{8/5}$ times (time from 800 °C to 500 °C), on M_s temperatures of FB2-2-LN.

In comparison to FB2-2-LN, the evaluation from equilibrium simulations for NPM1-LN shows quite similar transformation temperatures (A_1=830 °C and A_3=869 °C, see Fig. 12). Further comparing, the results of NPM1-LN-C for the A_{c1} and A_{c3} temperatures are about ~10 °C and ~30 °C higher, respectively. The evaluation of the M_s temperature for NPM1-LN-C results in ~410 °C and is shown Fig. 22 b). This is ~40 − 50 °C higher and due to the lower C content of NPM1-LN compared to FB2-2-LN (see Table 1). Measuring the necessary undercooling for martensitic transformation from A_{c3} temperature to M_s temperature, FB2-2-LN needs a ~10 − 20 °C larger undercooling compared to NPM1-LN.

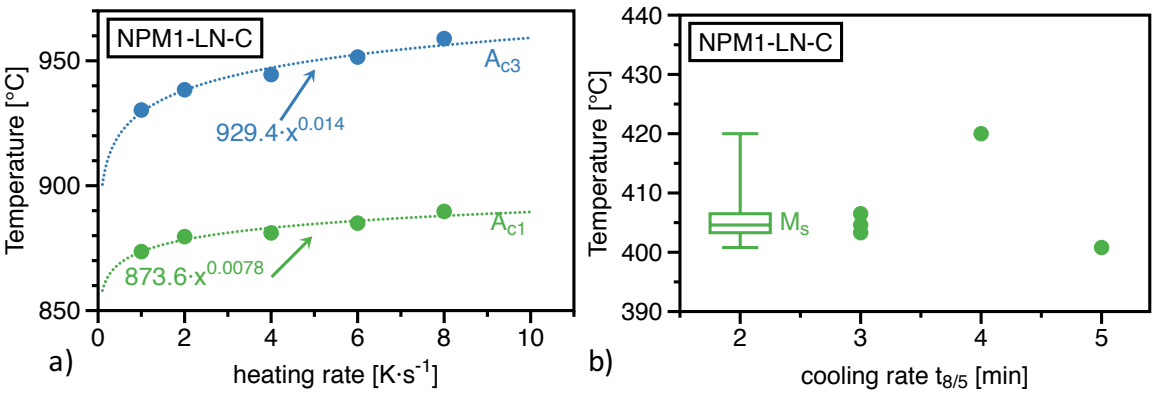

Fig. 22 Influence of a) heating rate on A_{c1} and A_{c3} temperatures and b) cooling rate, here expressed as different $t_{8/5}$ times (time from 800 °C to 500 °C), on M_s temperatures of NPM1-LN.

The quenching temperatures of the Q&P HT specimens are determined with the dilatometry experiments in Fig. 23 and Fig. 24. At the M_s point, the cooling rate is ~0.5 Kmin^{-1}. The numerical derivative of the extension dl with respect to the temperature is used to create a fit. The total area between the black horizontal line and the fit corresponds to 100 % of α'. For the FB2-2-LN-C steel in Fig. 23 a), the 0 % and 100 % lines indicate the M_s at ~370 °C and the M_f temperatures at ~275 °C, respectively. Two additional vertical lines indicate an amount of 50 % and 80 % of α'. Comparing Fig. 23 a) with b), the characteristic temperatures between the C and P-route of the FB2-2-LN differ within a range of ~9 °C.

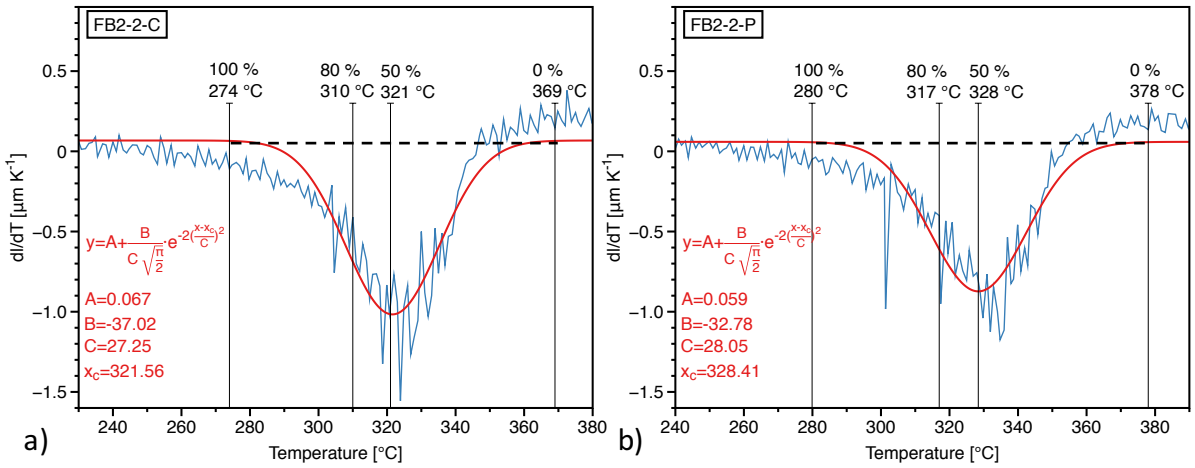

Fig. 23 Length change per temperature step indicates phase transformations by deviations from the linear thermal expansion during cooling for a) FB2-2-LN-C and b) FB2-2-LN-P material. The distance between the imaginary bottom line and the $\frac{dl}{dT}$ value is proportional to the transformed amount during the temperature step.

Fig. 24 a) and b) indicate the characteristic values of the transformed amount (0-100 %) for NPM1-LN-C and NPM1-LN-P steels within a range of ~7 K. For the NPM1-LN, the formation of α' starts ~40 °C higher than in the FB2-2-LN. For both steels, ~95 % of α' is formed in a temperature range of about 100 – 90 °C. The temperatures producing an

amount of about 65 % of α′ and of 35 % of RA (between 50 % and 80 %) in the P-specimens, i.e. $T_{NPM1\text{-}P}$=360 °C and $T_{FB2\text{-}2\text{-}P}$=323 °C were selected as quenching temperatures for the Q&P HT.

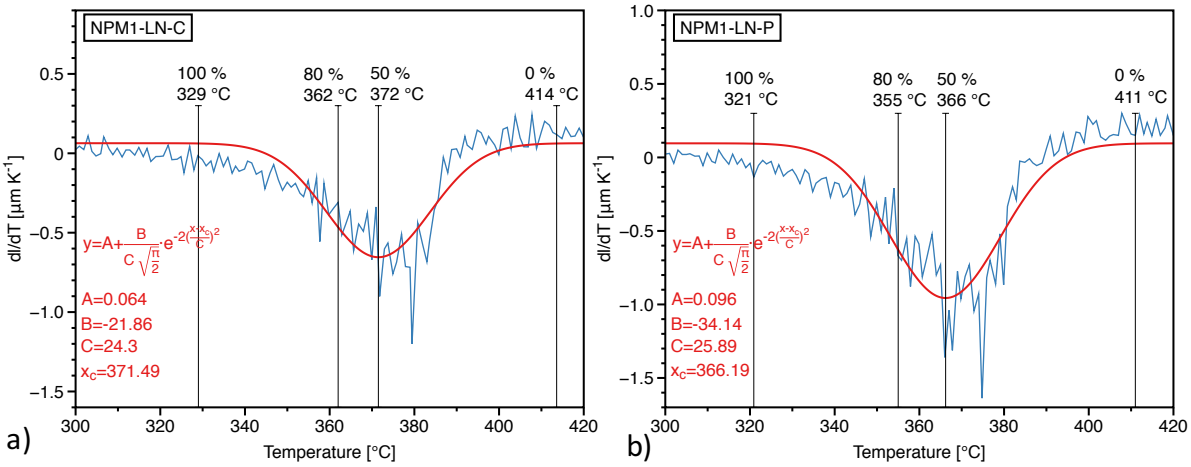

Fig. 24 Length change per temperature step indicates phase transformations by deviations from the linear thermal expansion during cooling for a) NPM1-LN-C and b) NPM1-LN-P material. The distance between the imaginary bottom line and the $\frac{dl}{dT}$ value is proportional to the transformed amount during the temperature step.

The next results show the detection of the phase transformation during a Q&P HT for two different tempering temperatures in the dilatometer. These experiments provide the basis for the evaluation with the Johnson-Mehl-Avrami-Kolmogorov (JMAK) [102] equation in Paper VI and are shown for FB2-2-LN-C in Fig. 25 a) and NPM1-LN-C in Fig. 25 b). By applying the Q&P HT - interrupted quenching upon austenitization, reheating directly to tempering temperatures of 600 °C and 700 °C and holding for 3 h - some differences become visible in Fig. 25. For both steels, the RA does not reconstructively transform into α at 600 °C, though both steels show an increased M_{s2} temperature compared to M_s. This increased M_{s2} temperature suggests recovery, relaxation of the transformation stresses from the shape deformation, and a change of the chemical composition by the formation of precipitates at the α′/γ interface and inside the RA and the α′ during tempering. The results change when increasing the temperature to 650 °C or - as indicated - to 700 °C. The temperature is high enough to reconstructively transform the RA into α and precipitates.

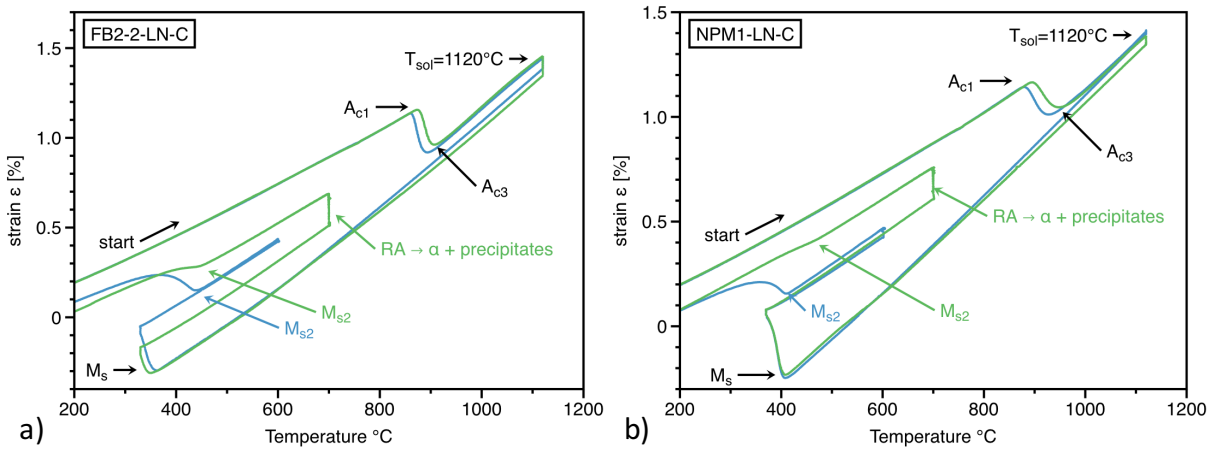

Fig. 25 Q&P HT for the tempering temperatures 600 °C and 700 °C of a) FB2-2-LN and b) NPM1-LN steel.

4.1.1 Evolution of the PAGS

As described in sec. 2.1, metallography and LOM is used to evaluate the PAGS for the as-received state from dilatometry test specimen. Selected micrographs for FB2-2-LN are published in Paper II. For the as-received state, the PAGS for both steels is between 20 - 50 µm. Fig. 26 shows the results for the a) NPM1-LN and the b) FB2-2-LN steel, fit to the square root of the time (see Eq. 3.1) and is used to estimate the PAGS. Despite lower constants for the NPM1-LN steel, the PAGS for both steels is rather similar and comparable.

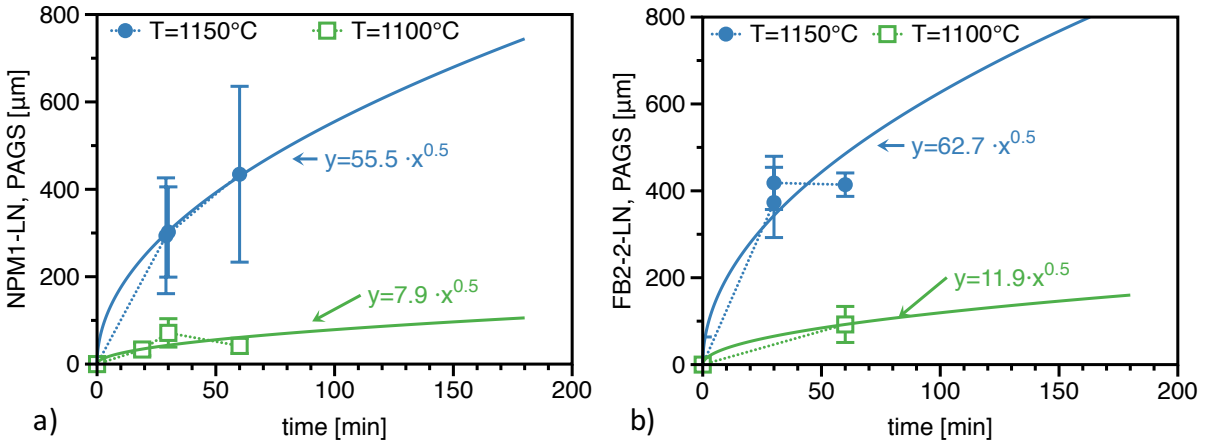

Fig. 26 PAGS evolution of NPM1-LN and FB2-2-LN for the austenitizing temperatures 1100 °C and 1150 °C.

4.2 Mechanical testing

This chapter shows results from Vickers hardness (HV) tests at a force of ten kilopond, which refers to 98,1 N (HV10 tests), Charpy-V impact tests, room temperature

fatigue tests and creep tests. Further, UTS values from tensile tests are compared to the HV10 values.

4.2.1 Hardness

Fig. 27 shows the HV10 values of steel samples quenched to RT for NPM1-LN-P and FB2-2-LN-P. Beside the indication of the applied HT, the PAGS is indicated at the bottom of Fig. 27. The applied austenitization conditions produce different PAGS (see Fig. 26), which do not systematically influence the HV10 values though the 300 µm specimen for FB2-2-LN-P shows ~20 HV10 higher values. FB2-2-LN-P shows ~40 HV10 values compared to NPM1-LN-P in as-quenched condition.

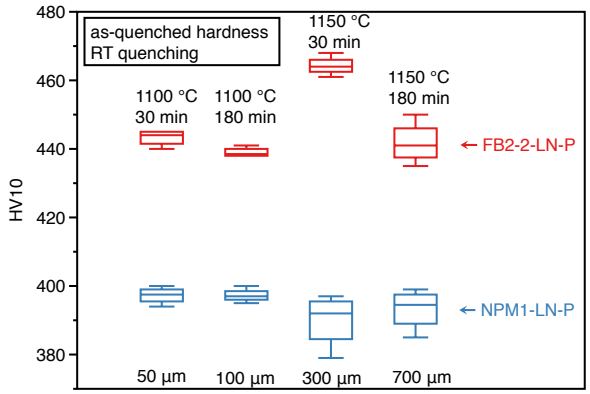

Fig. 27 As-quenched HV10 comparison between NPM1-LN-P and FB2-2-LN-P.

Fig. 28 a) and b) show HV10 values of FB2-2-LN-P and NPM1-LN-P after the Q&T and Q&P HT on specimens before the comparative creep rupture tests (see HT in Table 3.2). The difference in hardness between the Q&T and Q&P is ~30-40 HV10, similar for both steels (Fig. 28 a) and b)). Comparing the hardness difference between NPM1-LN-P and FB2-2-LN-P in the RT quenched and AHT state, the difference drops from 40 HV10 to 10-20 HV10 (compare Fig. 27 a) with Fig. 28 a) and b)).

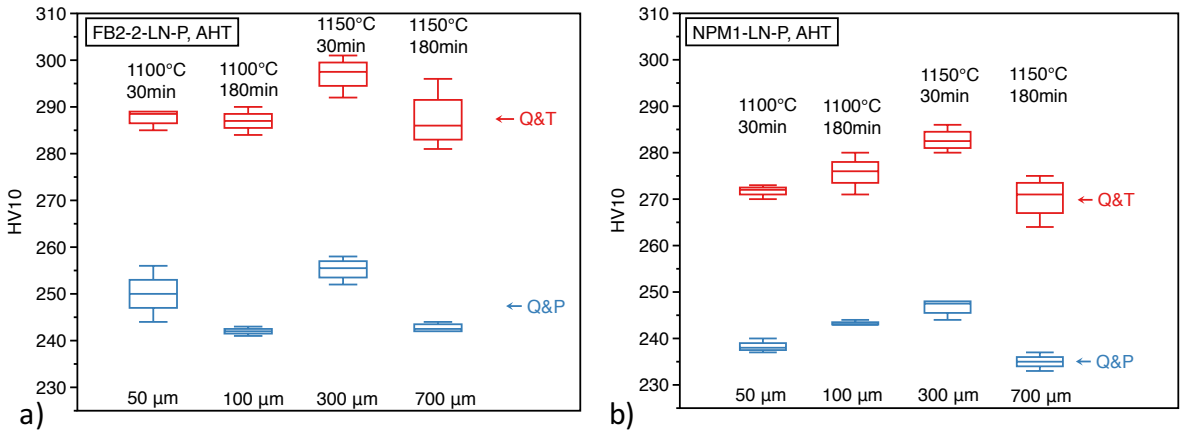

Fig. 28 HV10 comparison between Q&T and Q&P for 4 different PAGS of the a) NPM1-LN-P and b) FB2-2-P steel for the HTC in shown in Table 3.2.

Fig. 29 a) and b) show box plots of the HV10 values taken at the head of the creep ruptured specimen after the comparative tests for both steels with different HT and PAGS. Each specimen is measured after a different creep rupture time (see Fig. 34). As for the as-quenched and AHT specimen, the hardness does not show a systematic influence of the PAGS. In comparison to the AHT stage, the hardness of each specimen is lower after creep rupture due to recovery processes [42], [65], [103]. The difference between Q&T and Q&P after creep exposure for the FB2-2-LN-P steel is about 30-35 HV10 (see Fig. 29 a)). For the NPM1-LN-P, this difference is only 15-20 HV10 and suggests more recovery processes of the Q&T HT specimen due to the longer creep rupture time and related longer exposure at 650 °C compared to FB2-2-LN. Comparing the hardness values between both steels in Q&T HT condition after creep rupture, FB2-2-LN-P has 10 HV10 higher values. Despite the higher AHT values of the FB2-2-P (Fig. 28 a)) after the Q&P process, the drop of about 20 HV10 after creep exposure (Fig. 29 a)) is higher compared to the drop of NPM1-LN-P Q&P specimen in Fig. 29 b).

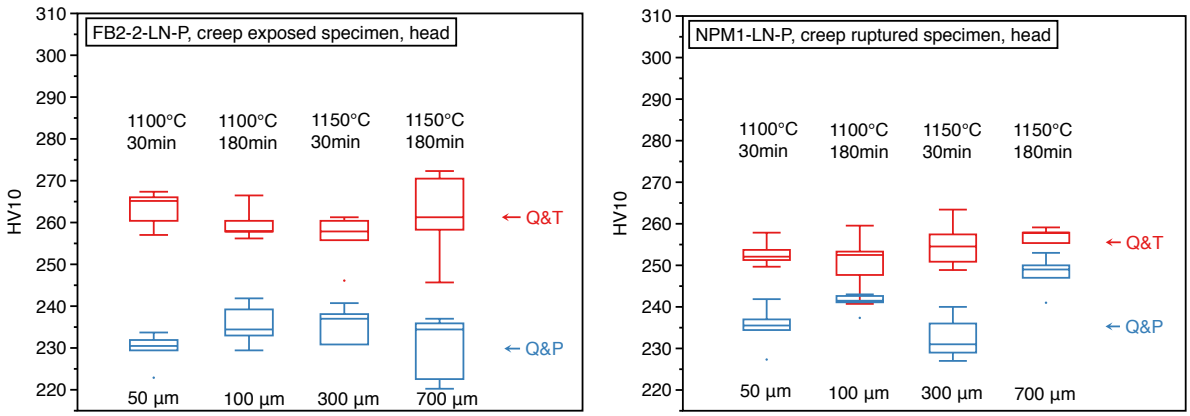

Fig. 29 HV10 measurements at the head of the creep specimen after rupture for the a) NPM1-LN-P and b) FB2-2-LN-P specimen.

Hardness measurements (HV10) are a simple way to control the transformed amount of α′ after the complete Q&P HT. Complete means after two tempering steps to not measure contributions of untempered α′. Fig. 30 a) shows the applied Q&P HT with the variation of the quenching temperatures between 430 °C and 250 °C, while keeping the two tempering steps at 750 °C for 3 h (each) constant. The HV10 values are measured after the 2nd tempering step and plot in Fig. 30 a) above the quenching temperature. Additionally, the M_s and M_f temperatures (see Fig. 24 b)) are indicated as vertical lines. Not considering the tempering temperature and time, the resulting hardness depends on the amount of initial transformed α′. The minimum HV10 value is found at 370 °C with ~215 HV10, which corresponds to the initial formation of ~50 % of α′ upon quenching as shown in the results of Fig. 24 b). If the specimen is directly reheated to tempering temperature from a quenching temperature above M_s temperature, α′ forms upon cooling after the 1st tempering step and results in a higher hardness because it is tempered only once. The transformation of mechanically stabilized RA (see sec. 2.2.2) into α'_2 after the 1st tempering step is the reason why thick walled forged components are tempered for two times. The 2nd tempering step is therefore necessary to temper the α'_2.

Fig. 30 b) compares the evolution of HV10 values after the Q&T and Q&P HT for the NPM1-LN-C steel during ~40 h of tempering at 700 °C. Because some of the RA retains and forms α'_2 after the 1st tempering step when applying the Q&P HT, the hardness of the Q&P HT samples drops within the initial 3 h tempering. Afterwards, the difference of ~30-40 HV10 between Q&T and Q&P remains even after 30 h of tempering at 700 °C.

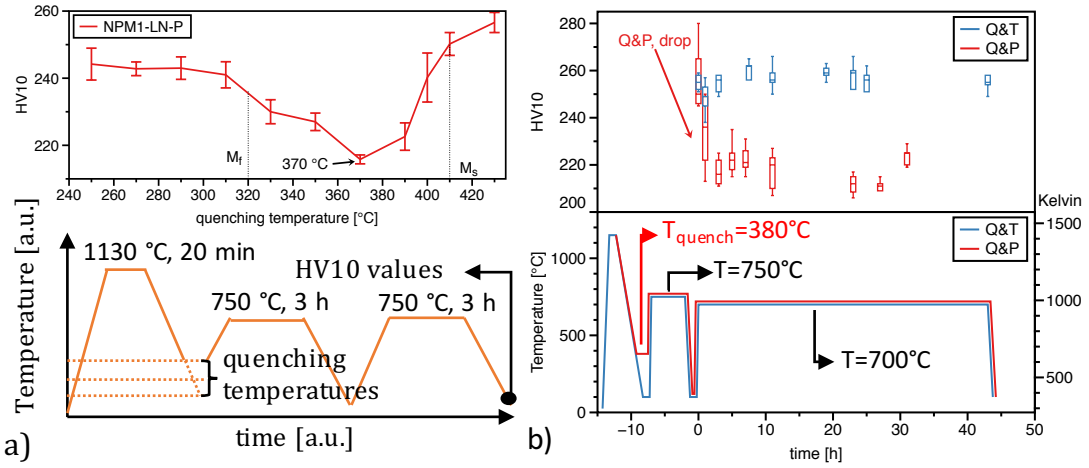

Fig. 30 a) Schematic HT with different quenching temperatures with the results from the corresponding HV10 measurements plotted above the quenching temperature, recorded with the furnace thermocouple. b) HV10 values during long time tempering of NPM1-LN steel at 700 °C for the Q&T and Q&P HT in comparison.

4.2.2 Charpy testing

Rotor steels in thermal power stations do not operate their entire service time at maximum steam temperatures within the creep regime. Mechanical properties at room temperature are also important.

Fig. 31 compares the influence of the PAGS on the impact work after the Q&T and Q&P HT. Fig. 31 a) illustrates the applied HT and the dimensions of the non-standard V-notched test specimen in mm. Fig. 31 b) shows the impact work as box plots for 4 tests of each HT. The impact work decreases with an increasing PAGS. Apart from the Q&T specimen austenitized for 30 min at 1100 °C (PAGS=50 µm), no influence of the impact work on the Q&T and Q&P HT is observed.

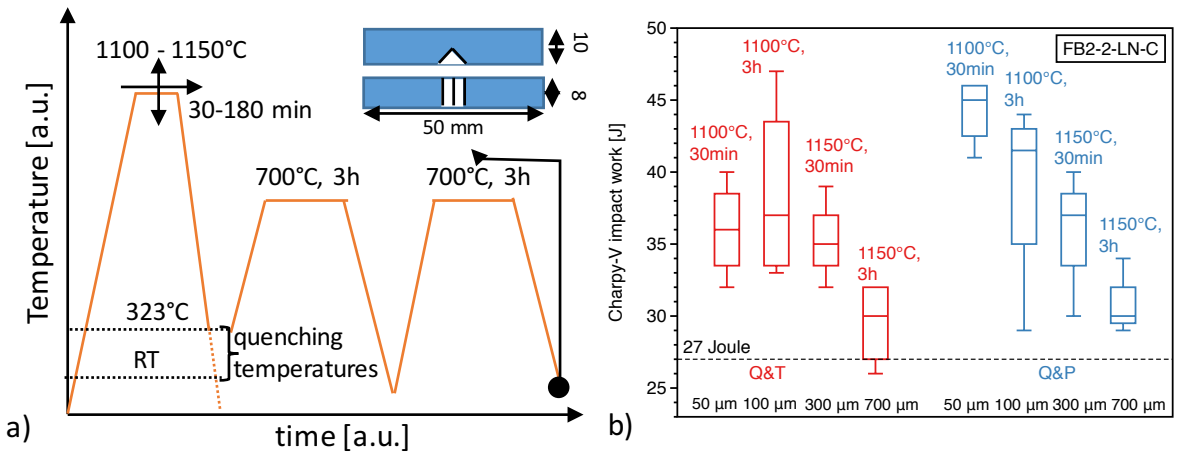

Fig. 31 a) HT for Charpy-V specimens of FB2-2-LN-C steel with the b) Charpy-V impact work of non-standard specimens (50 x 8 x 10 mm) in size order with an increasing PAGS.

4.2.3 Tensile and fatigue testing

NPM1-LN-P steel specimens are used for a series of tensile and hardness experiments to measure differences among the applied quenching temperatures and the 1st tempering time (responsible for α formation). The corresponding test matrix is illustrated in Table 3. For all specimens, the austenitization conditions are 1150 °C for 30 min (T_1, t_1). The quenching temperature (T_2) is varied at three different levels to produce three different amounts of α′ (~30 %, ~90 %, and ~100 %). The specimens are soaked at the quenching temperature for 1 h, before heating to tempering temperature T_3 for either 3 or 5 h. After quenching to room temperature (T_4) the specimens are again tempered at 700 °C for 3 h. For statistical reasons, 3 specimens are used for each HT.

Table 3 HT matrix with three different quenching temperatures and two different t_3 times.

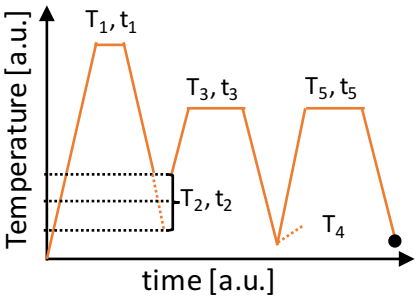

#	T_1 [°C]	t_1 [h]	T_2 [°C]	t_2 [h]	T_3 [°C]	t_3 [h]	T_4 [°C]	T_5 [°C]	t_5 [h]
1	1150	0.5	380	1	700	3	25	700	3
2	1150	0.5	380	1	700	5	25	700	3
3	1150	0.5	340	1	700	3	25	700	3
4	1150	0.5	340	1	700	5	25	700	3
5	1150	0.5	25	1	700	3	25	700	3
6	1150	0.5	25	1	700	5	25	700	3

For each tensile specimen the UTS and corresponding HV10 values after each HT are illustrated with the corresponding error bars in Fig. 32 a). It is evident that the quenching temperatures of 380 °C produce the highest UTS and HV10 values. The most probable reason for this is a too low soaking time (1 h) and no martensite formation when cooling

from the 1st tempering temperature to T_2 (see Table 3, M_s=410 °C). The second highest values are obtained on room temperature quenching and the lowest are achieved after quenching to 340 °C. While a clear effect of the tempering time is observed when quenching between M_s and M_f (#1, #2, #3, #4), almost no difference is observed among #5 and #6. The lower hardness for the specimens tempered for 5 h (#2, #4) compared to 3 h (#1, #3) is related to a higher amount of reconstructive transformed α. The created fit correlates between HV10 and UTS values with a factor of 3.0 (3.2 for HB).

Fatigue tests at RT are carried out on FB2-2-LN steel specimens to compare the fatigue limit for 10e7 cycles after the Q&T and Q&P HT. The austenitizing conditions are 1150 °C for 30 min; the quenching temperature for the Q&P HT is 340 °C (between 50 - 20 % of α′ according to Fig. 23) followed by two times annealing at 750 °C for 3 h. The machined and polished (R_a=0.2 µm) test specimens are loaded with R=-1 at a frequency between 107 – 125 Hz. Fig. 32 b) plots the applied stress amplitude versus the cycles to failure (S-N plot). The fatigue strength of the Q&P HT specimens is ~60 MPa lower in comparison to the Q&T HT specimens. The fracture surface of all specimens is analysed and evaluated.

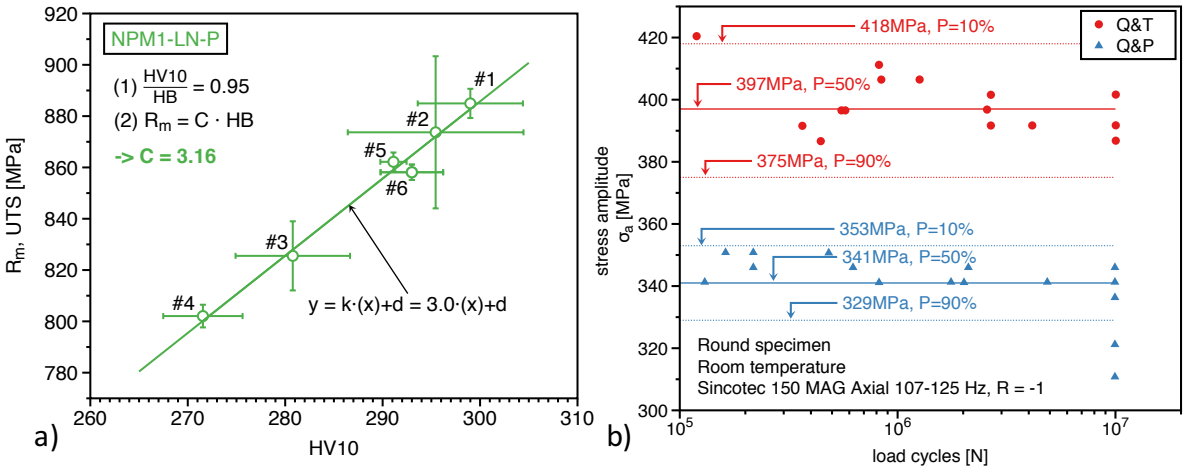

Fig. 32 a) Linear correlation between the ultimate tensile strength (UTS) and the hardness values of NPM1-LN-P tests for estimation. b) Comparative fatigue test results of FB2-2-LN-P specimen for an austenitization temperature of 1130 °C, 20 min after Q&T and Q&P HTC.

Fig. 33 shows SEM images of one selected specimen for each HT to illustrate the fracture surface after the fatigue tests in top-view. The total fracture surface is divided into two areas, the fatigue fracture surface and the residual fracture surface. After analysing

the fatigue fracture surface of each test, the fatigue crack initially started from the specimen surface and created a fracture plane macroscopically normal to the loading direction. Despite the different fatigue strength levels, the fatigue fracture surface (indicated with #1 in Fig. 33 a) and #4 in Fig. 33 b)) is evaluated after the tests to be 48.9 $\pm$ 7.5 mm^2 (62 %) for the Q&P and 43.0 $\pm$ 13.6 mm^2 (55 %) for the Q&T HT specimen. The Q&P HT specimens generally rupture at lower stress levels, show higher ductility but a lower endurance limit.

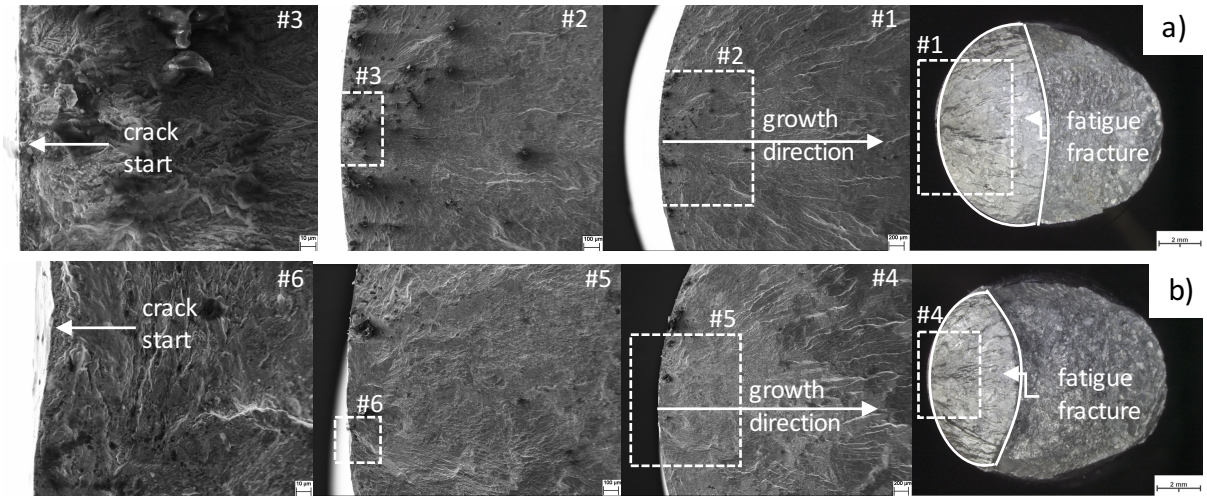

Fig. 33 a) Fracture surface of the FB2-2-P, Q&P and b) Q&T with the crack initiation for both starting from the surface.

4.2.4 Creep testing

To compare the creep results among different PAGS and their way of quenching - Q&T and Q&P HT (see Table 3.2) - FB2-2-LN-P (Fig. 34 a)) and NPM1-LN-P (Fig. 34 b)) are creep tested at 650 °C and 150 MPa. The Q&P HT lead to longer creep rupture times than the Q&T HT in both steels. A PAGS of 300 µm for the FB2-2-LN-P specimen results for both HT in the longest creep rupture times (see Fig. 34 a)). The martensitic NPM1-LN-P specimen with a PAGS of 300 µm failed prematurely from a crack initiated at the surface. The Q&P HT in NPM1-LN-P shows longer creep rupture times within each PAGS (Fig. 34 b)).

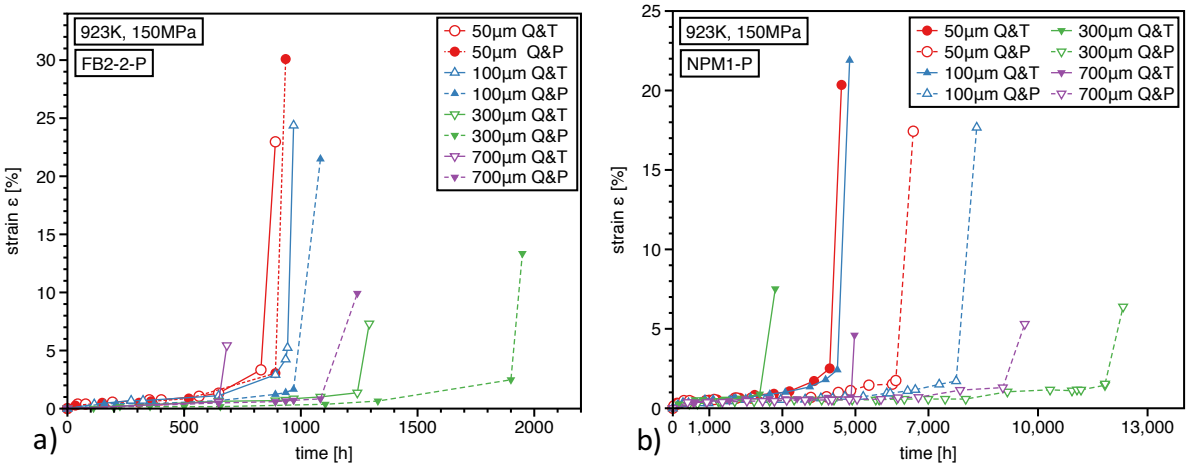

Fig. 34 Comparative creep results for the different PAGS and quenching conditions for a) FB2-2-LN-P and b) NPM1-LN-P at 650°C and 150 MPa.

Comparing the creep rupture ductility, Fig. 35 a) shows a Hall-Petch type relationship between ductility and the increasing PAGS [64], [104]. For the Q&P HT specimens, LOM is used to measure the area fraction of creep pores on a selected position (non-necking area) at the gauge section. The results of LOM with a resolution limit of ~1 µm in Fig. 35 b) show a decreasing area fraction of creep pores with an increasing PAGS. The creep rupture ductility decreases with a decreasing area fraction of pores. Comparing between NPM1-P and FB2-2 and despite a lower area fraction of pores, FB2-2 shows higher creep rupture ductility.

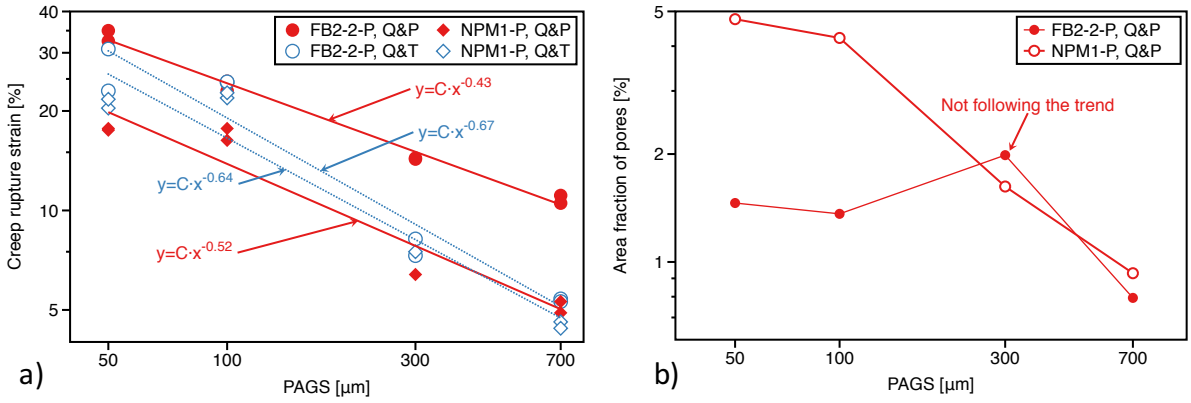

Fig. 35 Comparison of HT according to their a) creep rupture strain [104] and b) area fraction of pores [105].

With an increasing PAGS and a decreasing area fraction of pores, the perimeter of the detected pores increases (Fig. 36 a)), which is a measure for larger creep pores. This leads in combination with the lower area fraction to a decreasing number density of pores (here: number per unit area) as plot in Fig. 36 b) which is the one probable reason for the decrease in creep rupture ductility with increasing PAGS. The orientation of creep cavities

to form larger trans-granular cracks is easier at larger interfaces such as the PAGB and is shown in the images of Paper IV.

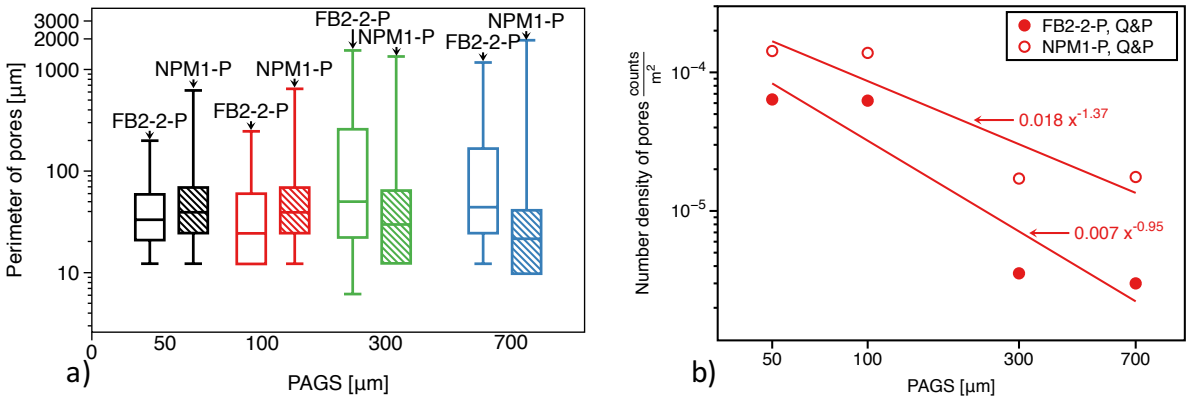

Fig. 36 a) Perimeter of pores with the b) number density of pores (number per unit area).

To compare NPM1-LN-P and FB2-2-LN-P with other 9 % Cr steels according to their creep rates and mechanism, the average creep rate ($\dot{\varepsilon}_s$) of all PAGS between 10 – 90 % of the total creep rupture life of both HT (Q&T and Q&P) is evaluated in Fig. 37 a) and b). The logarithm of the $\dot{\varepsilon}$ from the interrupted measurements follows a normal distribution and allows to indicate the standard deviations. NPM1-LN-P shows an average creep strain rate which is six times lower compared to FB2-2-LN-P.

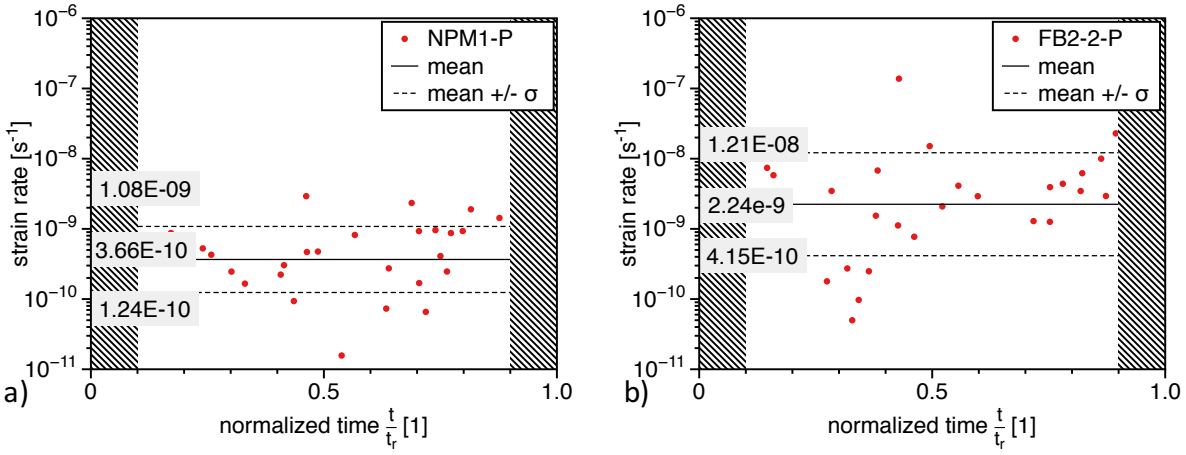

Fig. 37 Measured creep rate between 10 % and 90 % of the creep rupture life of a) NPM1-LN-P [64] and b) FB2-2-LN-P at 650 °C.

As mentioned in the section 2.5, for applications to last for 10 yrs in service, a stress exponent of n~1 at a strain rate $\dot{\varepsilon}$ < 1e-10 is required to not touch the 1 % or 2 % creep strain limit within this time. Fig. 38 a) compares the evaluated $\dot{\varepsilon}_s$ of the FB2-2-LN-P and NPM1-LN-P in the secondary creep regime (Fig. 37) to the minimum creep rate of other 9-12 % Cr creep resistant steels. The error bars indicate the standard deviations, taken

from Fig. 37. Both steels, NPM1-LN-P and FB2-2-P expand the Harper-Dorn regime to higher stresses. Comparing the two steels it can be assumed that FB2-2-LN is already in the transition from Harper-Dorn to dislocation creep.

The creep rupture curves of Fig. 38 b) compare creep results in Q&T condition to present 9 % Cr steels at 650°C. FB2-2-LN-P shows superior creep behaviour compared to P92 [76]. The conventional route of NPM1-LN-C shows similar and the NPM1-LN-P (both compared in Q&T condition) exhibits superior creep behaviour compared to P93 at 650 °C [77].

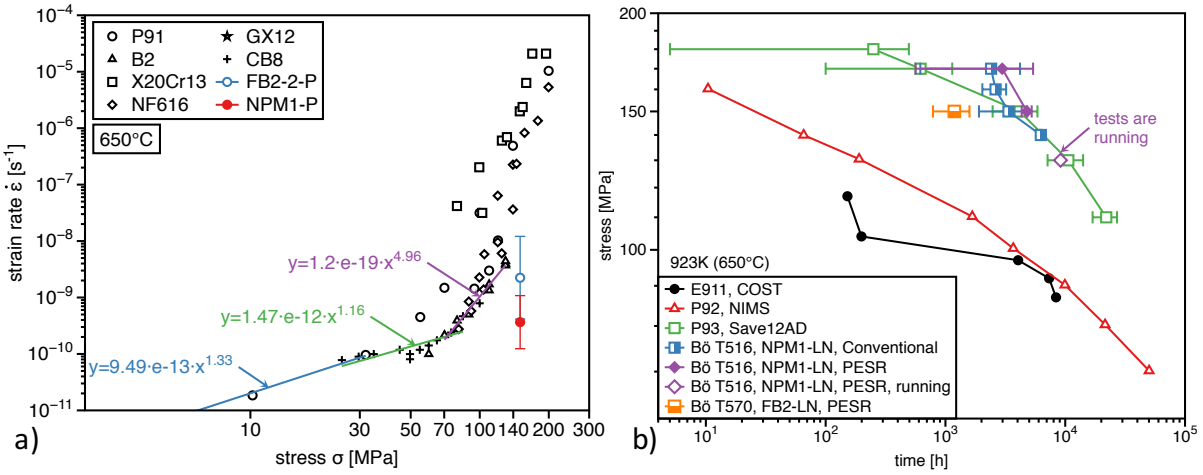

Fig. 38 a) Influence of stress on the creep rate in the secondary creep regime and b) comparing the creep strength of FB2-2-LN-P and NPM1-LN-P to other 9-12 % Cr steels.

4.3 Microscopy and simulation

To observe the phase transformation and to investigate microstructure-property relationships, microscopy investigations are carried out in AHT condition and after creep rupture for the NPM1-LN and FB2-2-LN specimens. Electron microscopy, HTLSCM investigations, MatCalc kinetic simulations on X20Cr13 are added and help to study the formation of carbides during the Q&T and Q&P HT.

4.3.1 HTLSCM, EBSD and HR-TEM investigation

The results from applying the HT of Fig. 18 b) in a laser scanning confocal microscope to a X20Cr13 stainless steel are shown in this video [106]. Fig. 39 shows extracted images during four characteristic steps: Fig. 39 a) austenitization; Fig. 39 b) the formation of α_1'; Fig. 39 c) the transformation of RA into allotriomorphic and idiomorphic ferrite at the

grain boundaries and inside the RA; Fig. 39 d) the transformation of RA into α_2' at a higher temperature than α_1'. The increase of the M_s temperature upon cooling from the tempering temperature is caused by stress recovery and the formation of carbides and will be later shown by simulation. This specimen is further used for microstructure examinations in a SEM and HR-TEM.

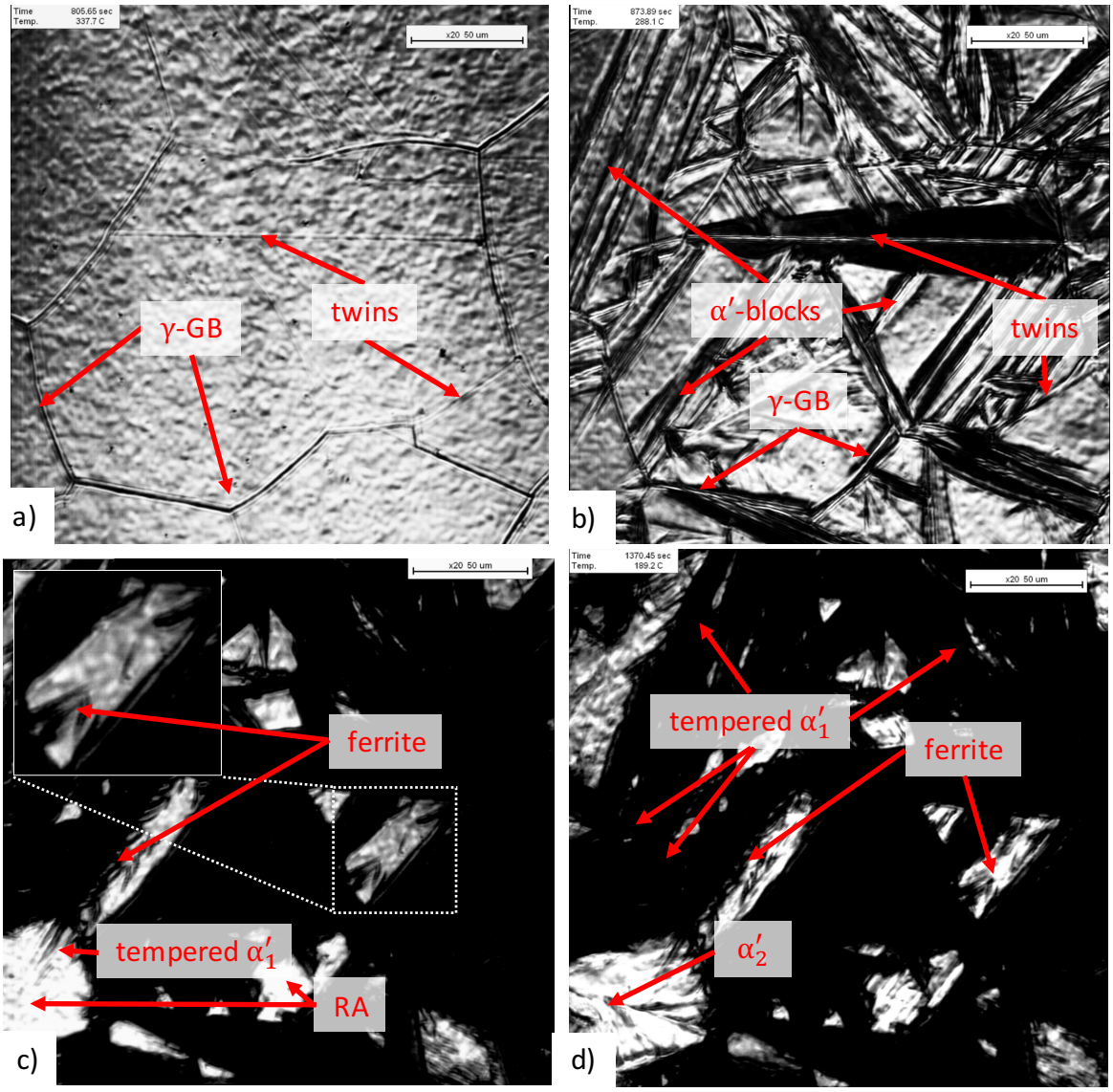

Fig. 39 Results from the LSCM experiments starting with a) austenitization, b) quenching between the M_s and M_f temperature, c) tempering above 700 °C and d) the transformation of residual austenite into α_2' during cooling formed at higher temperature than α_1'.

With the FIB, a lamella is extracted from the interface between the α_1', α and α_2' at a selected position of the LSCM specimen (see Fig. 40 a)), to investigate the tempered α_1' and the interface in high resolution. After extraction, the LSCM specimen is investigated by EBSD. The IFP map in Fig. 40 b) illustrates the crystallographic orientation and posi-

tions of allotriomorphic ferrite formed during the in-situ experiments [106]. Allotriomorphic α is found at the PAGB and at the block boundaries (indicated with #1 and #2) in Fig. 40 a) and b). #3 indicates α inside the former γ grain and is here regarded to be idiomorphic, because of non-present boundaries to limit the growth direction.

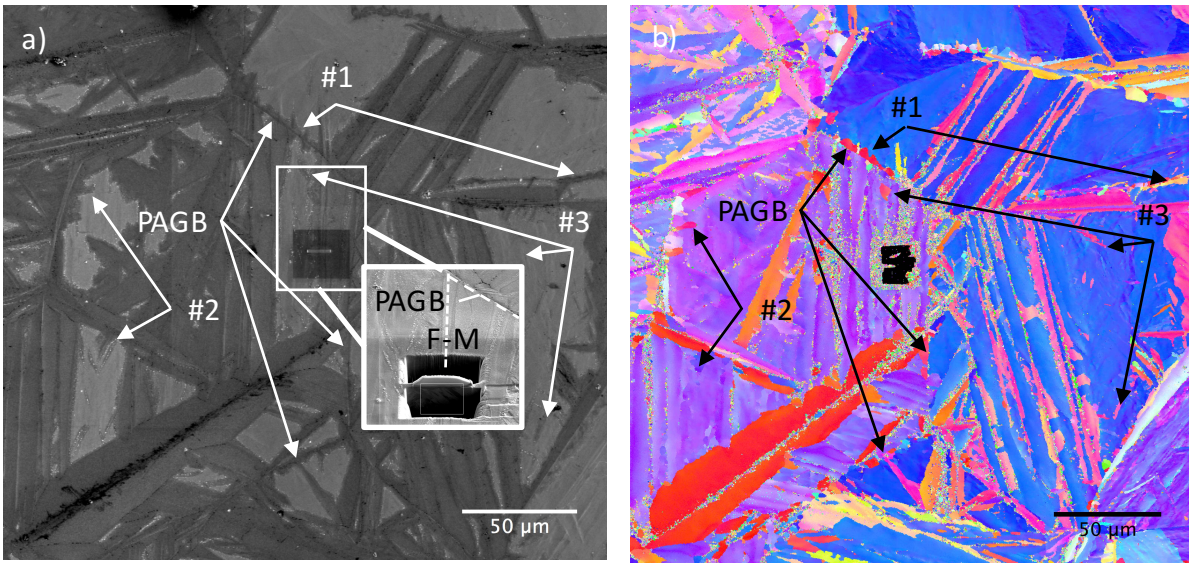

Fig. 40 a) SE-image of the LSCM sample to show the position of the FIB-cut, allotriomorphic (#1, #2) and idiomorphic ferrite (#3), with the corresponding b) inverse pole figure map indicating the same features.

The extracted FIB lamella in Fig. 41 a) is taken from the position in Fig. 40 a) and is used for the TEM investigations as depicted from Fig. 41 to Fig. 46. The magnification of Fig. 41 a), Fig. 41 b) gives an overview of the interface between the tempered α_1' and the α_2' which is formed from RA directly after tempering. The difference between tempered α_1' and the α_2' (Fig. 41 b)) is visible from the diffraction contrast due to the higher dislocation density. Depending on the location and geometry of M_3C carbides (see Fig. 41 c)) and the EFTEM image of Fig. 42 a), M_3C grows during tempering inside the α_1' block and at the interface between α_1' and α_2'.

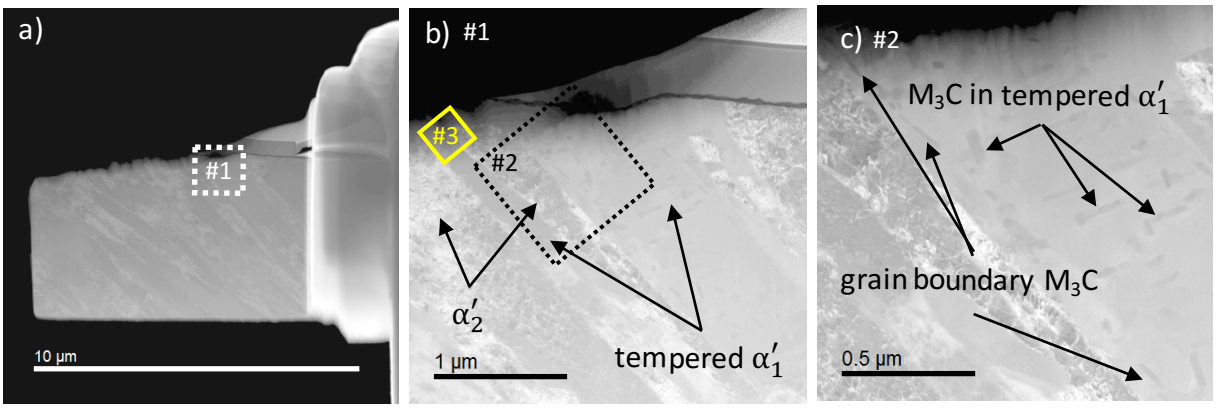

Fig. 41 HAADF images of the a) FIB lamella with the b) position of the interface magnified in c) M_3C carbides oriented along the grain boundary.

In Fig. 42 a) – c) the different growth direction of M_3C carbides inside the grain (Fig. 42 b)) compared to the block boundaries (Fig. 42 a)) becomes evident. These carbides appear longer compared to the M_3C inside the block (Fig. 42 b)). To investigate the M_3C carbides at the boundaries, Fig. 42 c) shows the magnification of position #3 in Fig. 41 b) to become further magnified in Fig. 43 a).

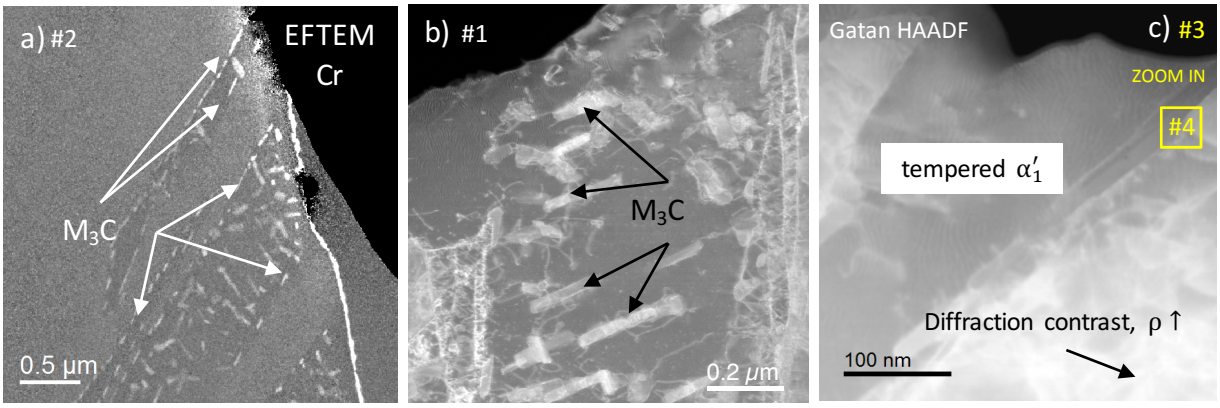

Fig. 42 a) EFTEM image at the position #2 indicated in Fig. 41 b) with b) magnification of M_3C precipitates grown inside the α′ block and a different block in c) magnification of Fig. 41 b) position #3 for further magnification in Fig. 43 a).

In Fig. 43 a) the tempered α'_1 matrix is oriented into the (111) zone axis. Fig. 43 b) and c) show a coherent interface between the tempered α′ matrix and the M_3C precipitate, which is oriented in the (001) direction. The orientation of the coherent interface at the other side of Fig. 43 c) - between the reconstructively grown α and the M_3C - is also observed. The tempered α'_1 and the reconstructively grown α are in similar orientation.

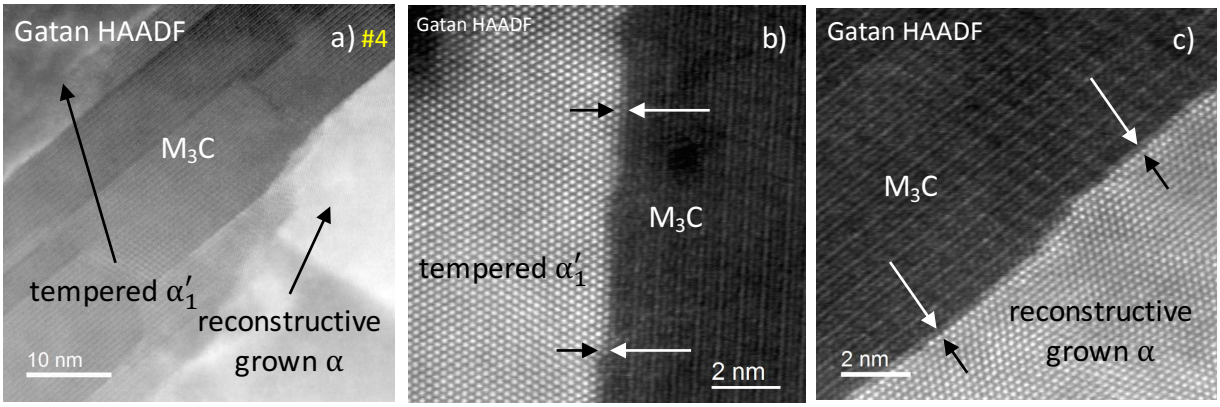

Fig. 43 a) magnification of Fig. 42 c) with the interface between b) tempered α′ and M_3C and c) M_3C and reconstructively grown α.

In addition to M_3C at the interface, Fig. 44 a) shows a M_3C grown inside the tempered α' block. The interface is coherent to the matrix. The carbide is surrounded by dislocations (indicated with dark arrows). The magnification at the tip of the M_3C in Fig. 44 b) shows a dislocation. A small shell is visible and indicated, which is in similar orientation with the matrix. Different to the orientation of the M_3C above, here the OR is $(111)_{bcc} \,||\, (-101)_{M_3C}$. Beside an overlapping EELS elemental map (see also Fig. 44 c)), a bright coherent interface between the carbide and matrix is visible. The bright diffraction contrast around the M_3C is either caused by the overlapping of matrix atoms if the carbide is not cut parallel, by coherency stresses or by voids. Fig. 44 c) shows another EELS line scan with the ordered arrangement of alternating Cr and C atoms within the orthorhombic crystal structure. The Fe signal is caused by the matrix.

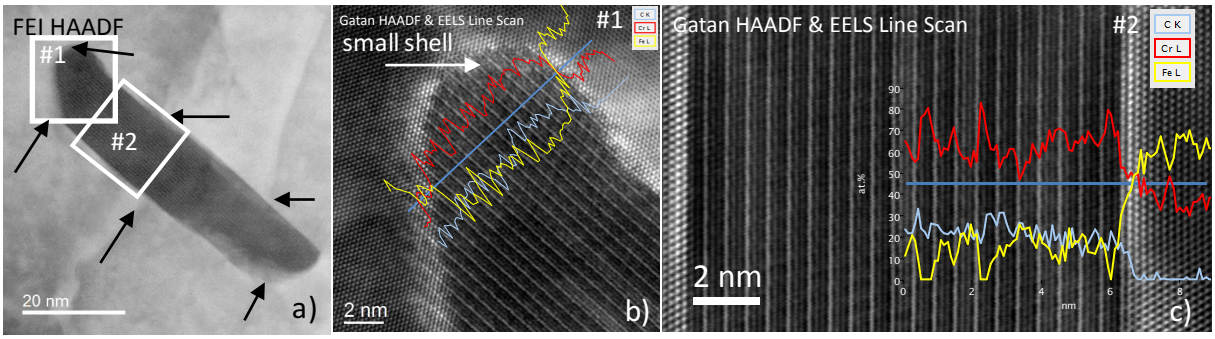

Fig. 44 a) M_3C carbide with dislocations (indicated with dark arrows) magnified at the b) tip and c) side of the carbide.

Fig. 45 a) and b) show M_3C in the early stages of precipitation. Fig. 45 a) depicts a dislocation with the marked area for the corresponding elemental map in b) which is identified as a precursor for the nucleation of M_3C. The dislocation core shows an enrichment of Cr and C atoms. By investigating different M_3C inside the block, dislocations are found

in the vicinity and attached to all carbides and are assumed to supply Cr and C through the core and accelerate the growth of M_3C.

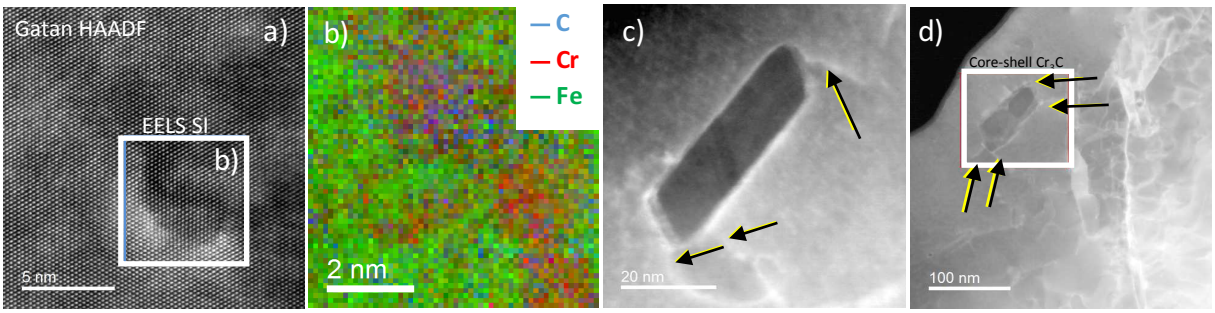

Fig. 45 a) Dislocations as nucleation sites and precursor for M_3C precipitates with the corresponding elemental map in b). c) M_3C precipitate with attached dislocations (arrows) and a small shell. The arrows in d) indicate dislocations surrounding a M_3C, which is analysed in Fig. 46.

Different to the M_3C before, Fig. 46 shows a magnification of the carbide in Fig. 45 d) surrounded by two shells. The outer shell 2 with a width of about 2 nm consists of 25 % C, 37 % Fe and Cr (at%), while the inner shell 1 (about 7 nm width) only contains about 12 % Fe. The core has a chemical composition of 25 % C and 75 % Cr and has an orthorhombic crystal structure with a lattice parameter 3 % smaller than the shell. The crystal structure and the lattice parameter of both shells are similar to the tempered α′ (111) oriented matrix. The core is (-103) oriented.

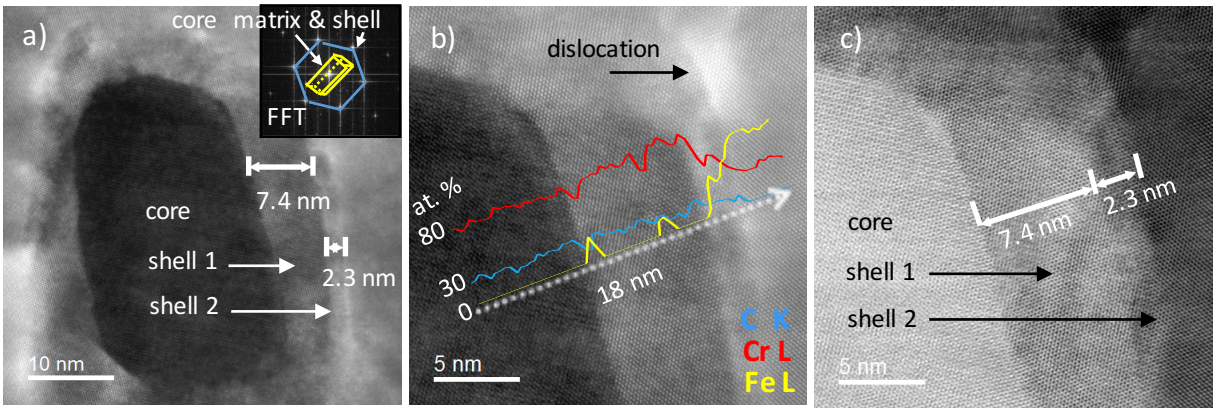

Fig. 46 a)-c) Shell type build up analysis of the shell-type M_3C precipitate at the position indicated in Fig. 45 d).

To show the nucleation and evolution of M_3C carbides at dislocations and interfaces from a kinetic perspective, the same HT is simulated as used for the HTLSCM experiments.

4.3.2 MatCalc kinetic simulation

Fig. 47 a) shows the HT, the evolution of the C-content of the α matrix, the phase fraction and the mean ecd of M_3C during the applied Q&T process (complete α′ formation at M_s temperature). The results show three populations of M_3C, one at the PAGB, one at the sgb and one at the dislocations. The largest phase fraction of M_3C grows at the dislocations and the sgb followed by the PAGB (~0.02 %). The phase fraction at the PAGB is of low amount and hardly visible in the plots and of 0.02 % during tempering. Despite different phase fractions, the populations simulated at the dislocations and sgb are of similar diameter. The release of C from the α matrix into M_3C precipitates occurs during heating to tempering temperature within 1 min time. During tempering, coarsening of M_3C is observed from the mean ecd.

Fig. 47 b) uses the similar HT as a) but a deformed γ matrix as a precipitation domain. In similar manner, Fig. 47 b) shows that carbides do not only grow by interphase precipitation or inside the α′ during tempering, but also through nucleation introduced by dislocations inside the deformed RA and corresponds to the previous results from the HR-TEM experiments. The deformation is introduced at the position indicated with ρ_{in} at M_s. Because the degree of local deformation changes with distance from the transformed block, the deformed γ with the population of M_3C precipitates at the dislocations is calculated for different dislocation densities (1e14 – 1e15 $\frac{1}{m^2}$). The reduction of the C-content inside the fcc matrix due the formation of M_3C carbides at the dislocations is observable. A dislocation density of at least 5e14 $\frac{1}{m^2}$ is necessary to significantly reduce the C content of the γ matrix within 5 min time. A horizontal line indicates the equilibrium solubility limit of the γ matrix at 800 °C. At that temperature, the simulated solubility of the α matrix is about $\frac{1}{20}$ of the γ. Below this amount the γ → α is supposed to start.

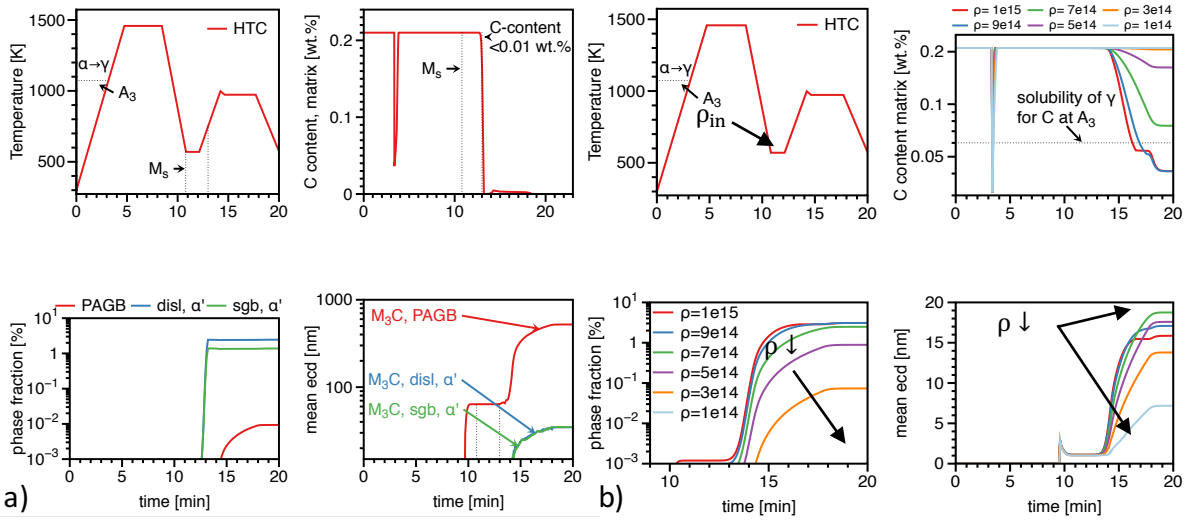

Fig. 47 Simulations to discuss the LSCM (X20Cr13) results. a) Evolution of M_3C carbides at the PAGB, at dislocations and sub-grain-boundaries after the complete $\gamma \rightarrow \alpha'$ transformation at M_s point (11 min). b) Evolution of M_3C at introduced dislocations (11 min) through the shape deformation of α'.

4.4 TEM and SEM investigations of NPM1-LN-P and FB2-2-LN-P

Table 4 gives an overview of the investigated specimens by SEM-EDX maps, SEM-EBSD and TEM. The TEM investigations included EDX and EELS analyses of precipitates and were carried out for each steel specimen at 10 positions (~50 μm^2). After illustrating one selected energy filtered TEM (EFTEM) image for each specimen, the chemical composition and size distribution are shown.

Table 4 Overview of the investigated steel specimen by SEM and TEM.

#	specimen	PAGS	Condition	Method	HTC
1	FB2-2-LN-P	50 µm	AHT	TEM + SEM-EDX mapping	Q&P
2	FB2-2-LN-P	50 µm	creep exposed	TEM + SEM-EDX mapping	Q&P
3	FB2-2-LN-P	300 µm	AHT	SEM-EDX mapping	Q&P
4	FB2-2-LN-P	300 µm	creep exposed	SEM-EDX mapping	Q&P
5	FB2-2-LN-P	300 µm	AHT	SEM-EBSD	Q&T, Q&P
7	NPM1-LN-P	50 µm	AHT	TEM + SEM-EDX mapping	Q&P
8	NPM1-LN-P	50 µm	creep exposed	TEM + SEM-EDX mapping	Q&P
9	NPM1-LN-P	300 µm	AHT	TEM + SEM-EDX mapping	Q&T, Q&P
10	NPM1-LN-P	300 µm	creep exposed	SEM-EDX mapping	Q&P
11	NPM1-LN-P	300 µm	AHT	SEM-EBSD	Q&T, Q&P

4.4.1 Precipitates analysed by TEM

TEM experiments are carried out for the Q&P and Q&T AHT state and for the Q&P creep ruptured NPM1-LN-P specimens with 50 µm PAGS. Fig. 48 a) shows STEM images for the Q&P AHT NPM1-LN-P steel after the Q&P HT. No clear distinction between Laves Phase and $M_{23}C_6$ can be made at this stage, though the STEM image for Carbon distinguishes areas of higher and lower C-content (Laves Phase). Fig. 48 b) shows an α′ interface measured with orientation imaging in scanning mode to illustrate point to point misorientation of 60 deg between the adjacent boundaries. At a nanometre scale the boundaries after tempering are bluntly shaped, which is probably due to the reconstructive transformation.

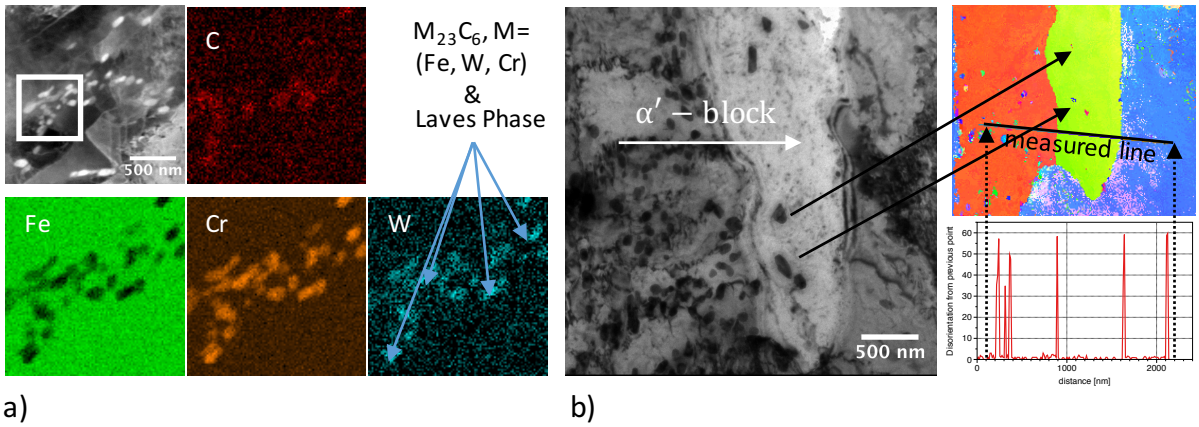

Fig. 48 a) STEM images for NPM1-LN-P 50 µm Q&P AHT specimen, b) TEM orientation imaging using the ASTAR system from Nanomegas [108].

Fig. 49 a) – d) shows histograms for the size distribution evaluated from the Cr and V EFTEM images for the a) – b) Q&P and c) – d) Q&T HT for two different PAGS. Comparing the EFTEM evaluation for Cr (a) and c)) and despite the large number of detected $M_{23}X_6$ precipitates (#398 and #146), no significant difference within the ecd of $M_{23}X_6$ is detected. The measured area for the Q&P was larger, which led to the higher number of detected $M_{23}C_6$ precipitates. The comparison of the ecd for the MX precipitates in Fig. 49 b) and d) shows for both HTs similar mean values of 13 nm and 15 nm.

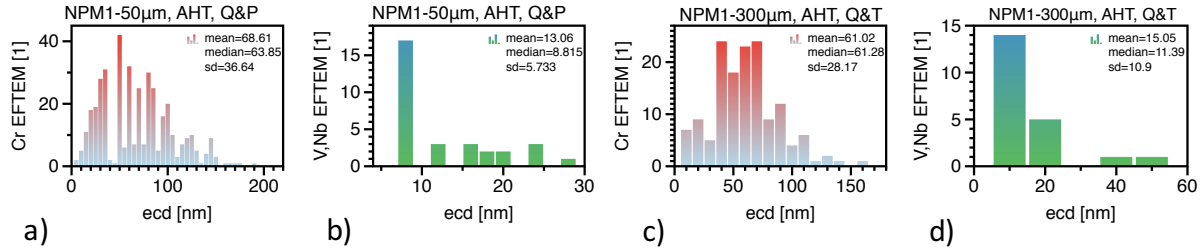

Fig. 49 Histograms of precipitates after Q&T HTC and Q&P from EFTEM images for a) – c) Cr and b) – d) V.

Table 5 shows results from comparative measurements of the chemical composition of $M_{23}C_6$ carbides after a Q&T and Q&P HT and indicating an incorporation of about 4 at% of W. The number of the measured precipitates by TEM-EDX is given in the first column. Similar values are obtained after the Q&T and Q&P HT. The TEM-EELS measurements for the $M_{23}C_6$ precipitates did not show an incorporation of B in the AHT stage. The amount of Laves Phase precipitates is too low to draw a histogram. However, TEM/EDX measurements of small Laves Phase precipitates after both HT Q&T and Q&P in AHT condition show an average content of 65 % $\pm$5 of Fe, 11 % $\pm$0.5 of Cr and 23 % $\pm$5 of W (based on 5 precipitates in at%).

Table 5 Evaluated average chemical composition of $M_{23}C_6$ carbides from TEM/EDX measurements in Q&T (300 µm) and Q&P (50 µm) AHT (in at%). # indicates the amount of measured carbides per specimen.

#	specimen	Fe	Cr	W	V	C
6	Q&T, AHT	33.1 $\pm$4.7	42.3 $\pm$4.5	3.9 $\pm$0.4	0.0	bal.
13	Q&P, AHT	31.4 $\pm$1.8	42.9 $\pm$1.5	4.3 $\pm$0.5	0.0	bal.

To compare if stress affects the size distribution of precipitates within the first 10,000 h of creep, TEM bright-field measurements are carried out for the creep exposed NPM1-P 50 µm Q&P specimen (t_r=6 580 h) at the head and gauge section of the specimen. This type of measurement does not allow a distinction among precipitates (Laves Phase, $M_{23}C_6$ and MX). The result is a large quantity of precipitates in one histogram. An example

image for the evolution of precipitates after creep rupture is shown in Fig. 50 a). The image shows that precipitates located at the boundaries are larger in comparison to the grain interior due to enhanced diffusional processes. Fig. 50 b) and c) show the size distributions for the head (435 counts) and gauge (241 counts) section of the creep exposed specimens. The histograms are rather similar, with only slight differences among their mean ecd (152 nm and 155 nm). This suggests a negligible influence of the applied stress on precipitate coarsening within the first 10,000 h of creep.

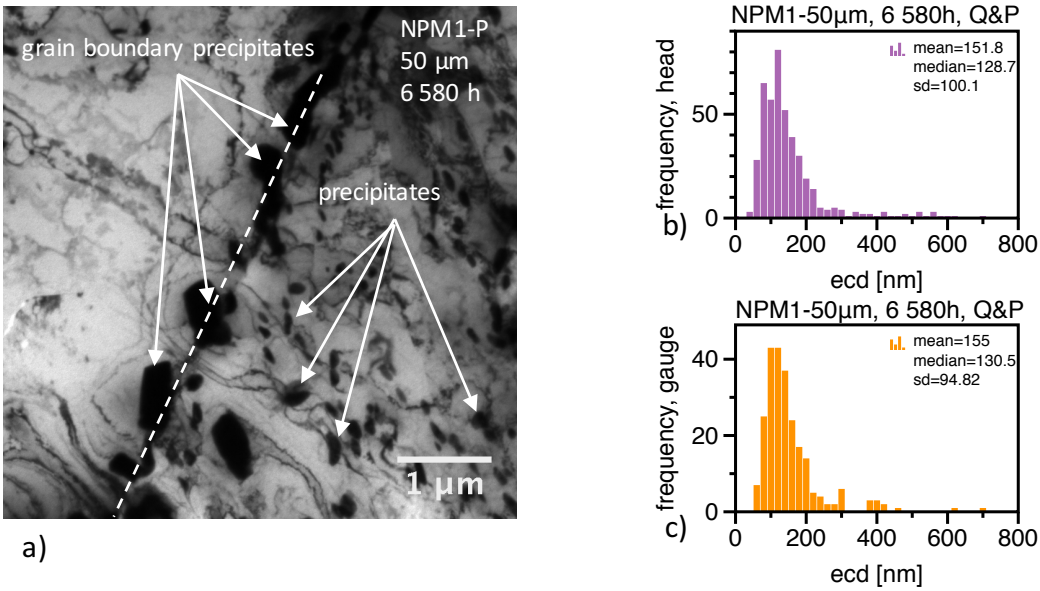

Fig. 50 a) STEM image of precipitates for NPM1-LN-P PAGS=50 µm Q&P after 6 580 h of creep exposure indicating precipitates of $M_{23}C_6$ and Laves Phase with the size distribution for all precipitates at the b) Temperature exposed head- and c) Creep exposed gauge section of the specimen.

After the TEM results for NPM1-LN-P specimens, TEM experiments for one FB2-2-LN in Q&P AHT condition and after creep rupture are shown. Fig. 51 depicts EFTEM images in AHT condition. From the contrast of the Fe EFTEM image, it is simple to recognize areas of different chemical compositions (precipitates). The precipitates found inside the steel after the Q&P HT are of MX type (V,Nb:C,N) and $M_{23}C_6$ containing Mo and Si. Si is not present in each $M_{23}C_6$ precipitate. Beside the $M_{23}C_6$, one large round shaped MX (NbC) is captured and indicated with #4.

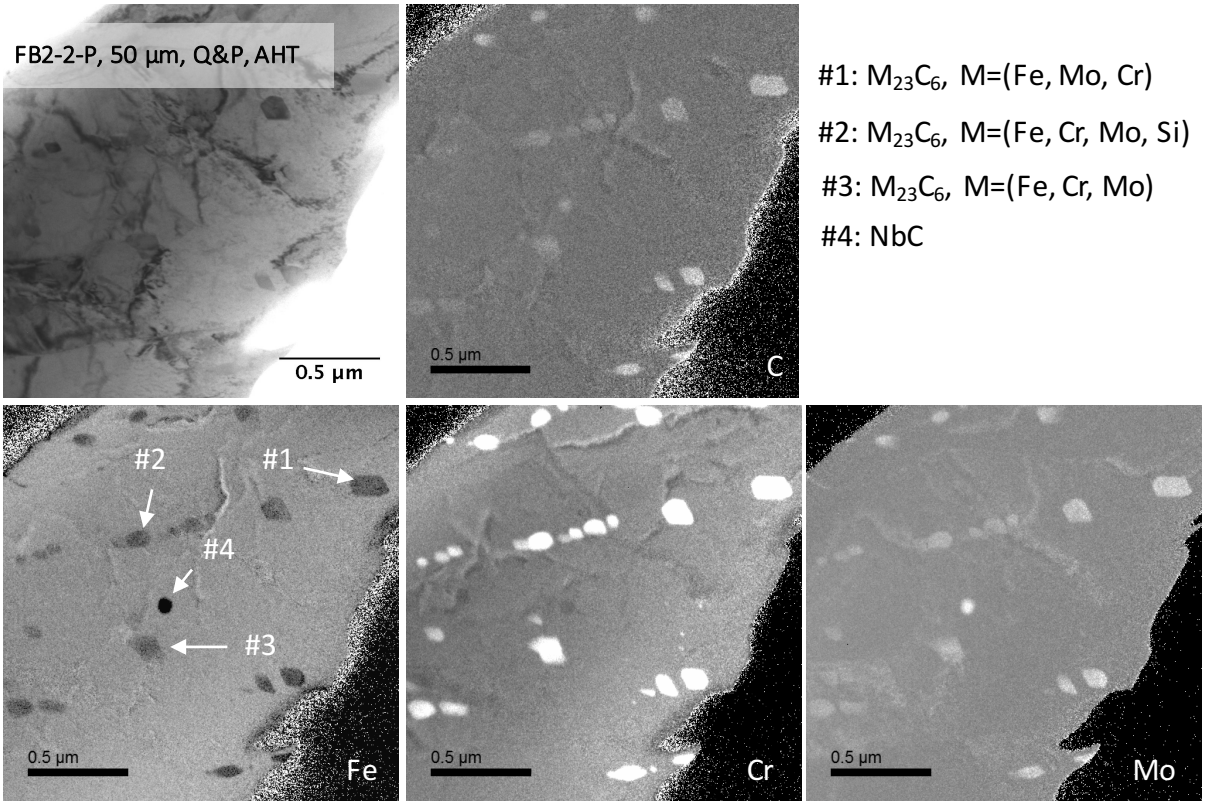

Fig. 51 EFTEM images of for C, Fe, Cr and Mo of FB2-2-P in Q&P as-heat-treated (AHT) condition at a PAGS of 50 µm.

MX (Nb,V:C,N) carbides or nitrides are typically smaller than Laves Phase or $M_{23}X_6$, which is visible in the EFTEM images of Fig. 52 for the FB2-2-LN steel after creep exposure for 940 h at 650 °C, 150 MPa. B incorporation is found with the EELS quantification in some of the $M_{23}X_6$ precipitates and summarized in Table 6.

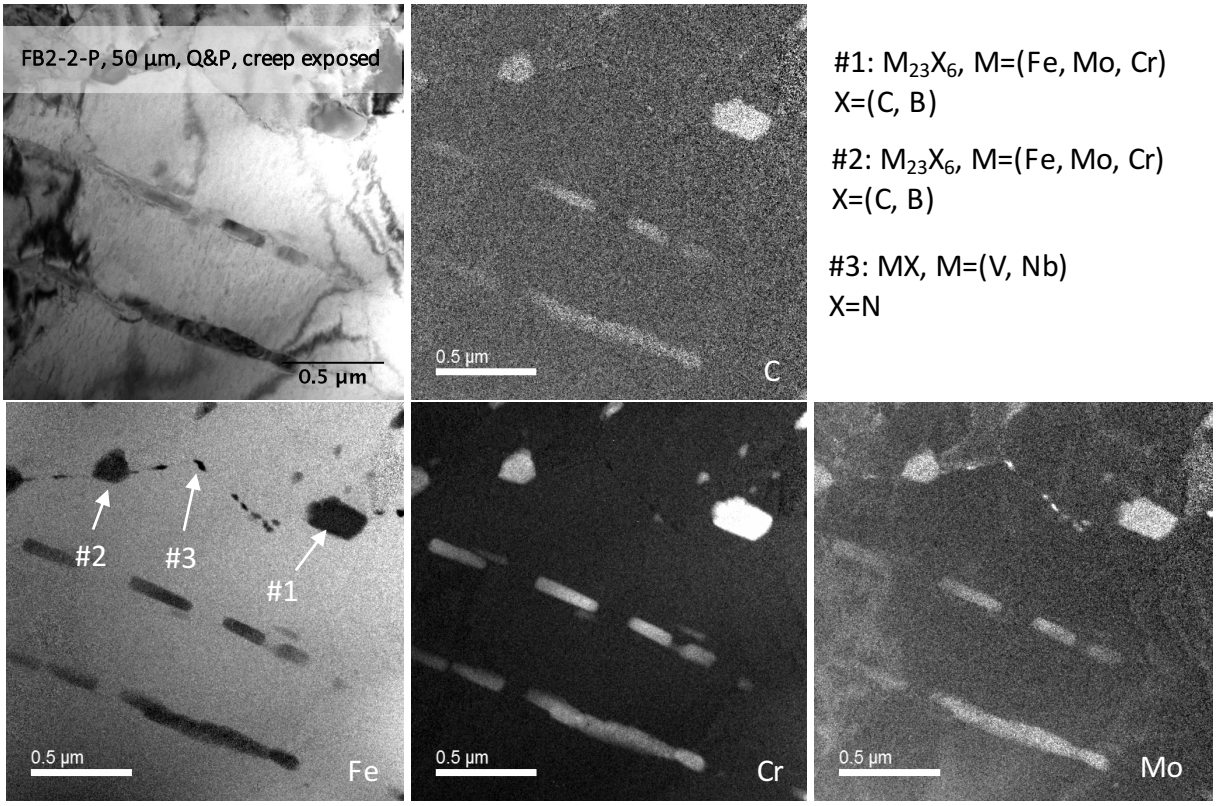

Fig. 52 EFTEM image of FB2-2-LN-P PAGS 50 µm after creep exposure of 940 h at 650 °C and 150 MPa.

The histograms in Fig. 53 a) - d) show the size distribution of all detected $M_{23}X_6$ and MX from TEM investigations in AHT condition and after creep exposure. For the $M_{23}X_6$ and MX precipitates, EFTEM images for Cr and V are used. Comparing the ecd of the Cr mappings in a) AHT and c) creep exposed condition, the mean ecd of $M_{23}X_6$ increases from 81 nm to 91 nm with an increasing standard deviation. Comparing the MX precipitates on the basis of the evaluation for V, the mean ecd increases from 16 nm to 26 nm although the statistics for the AHT specimen can be considered as weak.

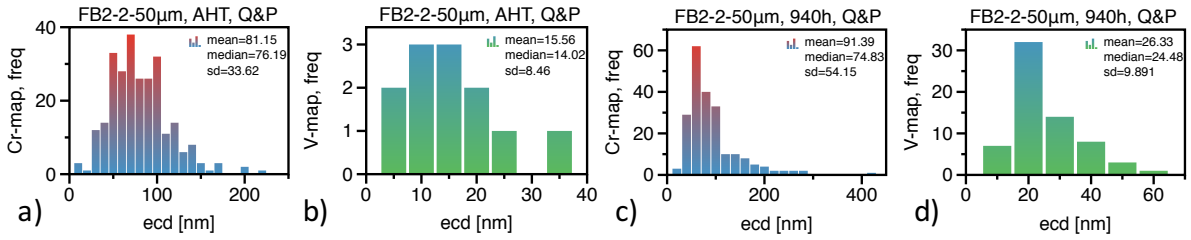

Fig. 53 Histograms of the a) Cr-map and b) V-map of the Q&P AHT stage and after creep exposure c) – d) of FB2-2-LN-P.

The evaluation of the chemical composition of $M_{23}X_6$ precipitates in AHT and creep exposed condition is summarized in Table 6 and based on 21 and 19 measurements respectively. While Si is only detected in $M_{23}X_6$ precipitates in AHT condition, a Mo content

between 3 – 5 at% is detected within each measured $M_{23}X_6$ precipitate. This means that the contribution of Mo to solid solution hardening decreases with increasing creep exposure time. B is measured in only some of the creep exposed FB2-2-LN-P specimen. In these $M_{23}X_6$ precipitates, the relation between the B and the C content was found to be 1:7 containing about 2.5 (at%) of B. The probability of detecting B inside the $M_{23}X_6$ decreases with increasing distance to the PAGB [109].

Table 6 Chemical composition of $M_{23}X_6$ precipitates measured with TEM/EDX and EELS (at%).

#	specimen	Fe	Cr	Mo	Si	C, B
21	FB2-2 P 50 µm, Q&P AHT	37.5 ±10.7	37.7 ±9.6	3.7 ±1.1	1.1 +1.6	bal.
19	FB2-2-P 50 µm, Q&P, creep exposed	28.5 ±6.4	46.1 ±6.0	4.8 ±0.8	-	bal.

4.4.2 SEM/EDX maps

In addition to the TEM investigations, SEM/EDX mapping experiments are carried out to capture precipitates at a lower resolution but for a larger area to evaluate and compare with histograms. The EDX-maps are carried out for both, the NPM1-LN-P and FB2-2-LN-P steel. The precipitates are compared in AHT stage and after creep exposure for two different PAGS of 50 µm and 300 µm.

The results for the detected area fraction of precipitates are summarized in Table 7. Cr is mapped to evaluate the area fraction of $M_{23}X_6$ and Mo (W) for the Laves Phase of FB2-2-LN-P (NPM1-LN-P). Comparing the detected area fraction for Cr ($M_{23}X_6$) and Mo or W (Laves Phase) in AHT, it becomes larger after creep exposure for almost each map. The evaluated area fraction of the Cr map for the FB2-2-P and NPM1-LN-P specimens with a PAGS of 300 µm remains at similar values before and after creep exposure. Comparing the Fe-map between NPM1-LN-P and FB2-2-LN-P, NPM1-LN-P shows a larger area fraction of precipitates after each stage. The amount of Laves Phase found in NPM1-LN-P is significantly higher than in FB2-2-LN-P.

Table 7 Summary of the SEM-EDX results for the area fraction (in % of the measured area) by mapping the elements Cr, W, Mo and Fe.

SEM/EDX, area fraction %	Cr-mapping	W-mapping	Mo-mapping	Fe-mapping
FB2-2-50 µm, Q&P, AHT	0.3	-	0.1	0.2
FB2-2-50 µm, Q&P, creep exposed, 940 h	0.4	-	0.4	1.7
FB2-2-300 µm, Q&P, AHT	0.5	-	0.1	1.4
FB2-2-300 µm, Q&P creep exposed, 1 950 h	0.5	-	0.8	1.8
NPM1-50 µm, Q&P, AHT	0.3	0.5	-	1.8
NPM1-50 µm, Q&P, creep exposed, 6 580 h	0.8	0.6	-	2.2
NPM1-300 µm, Q&P, AHT	1.4	0.1	-	1.5
NPM1-300 µm, Q&P, creep exposed, 12 330 h	1.3	3.0	-	4.6

Compared to the TEM results, the resolution limit of 0.01 µm² qualifies the evaluations from SEM only for qualitative comparison. Despite this fact, the histograms of the ecd for the Cr and Mo maps of the FB2-2-LN-P are plot in Fig. 54 a) and b), Q&P AHT and after the creep rupture. The larger analysed area within the SEM/EDX experiments allows to draw a size distribution for Laves Phase. The comparison of the ecd between the AHT specimens with PAGS 50 µm and 300 µm shows similar values. During creep, precipitates coarsen; after creep rupture, the comparison shows lower ecd values for the Cr and Mo map of the PAGS 300 µm, despite the longer creep rupture time (940 h compared to 1 950 h at 650 °C).

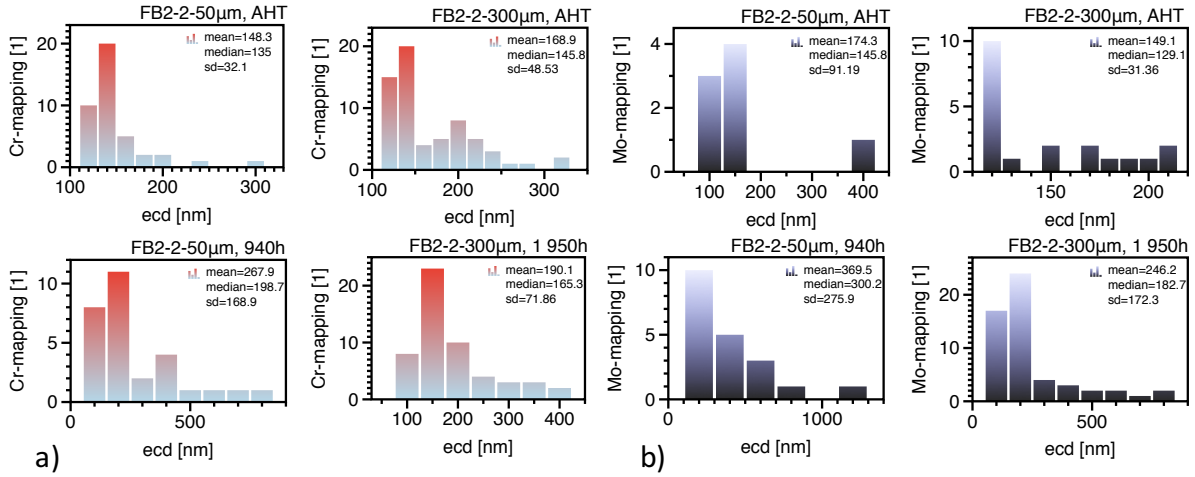

Fig. 54 Histograms of the SEM/EDX mappings Q&P AHT and after the creep rupture tests for a) Cr and b) Mo for the FB2-2-P steel.

The similar evaluation for the NPM1 steel in Fig. 55 shows similar values compared to FB2-2 (Fig. 54) for the Cr and W map in AHT condition. Despite a doubling creep exposure time when increasing the PAGS from 50 µm to 300 µm and the higher amount of detected area fraction for the Cr-map (see Table 7), the median ecd in Fig. 55 a) is rather similar (142 nm compared to 146 nm). A significant difference is visible by comparing the ecd for the W-map after creep exposure (Fig. 55 b)) and detected area fraction (0.5 % and 3.0 %) for 50 µm and 300 µm.

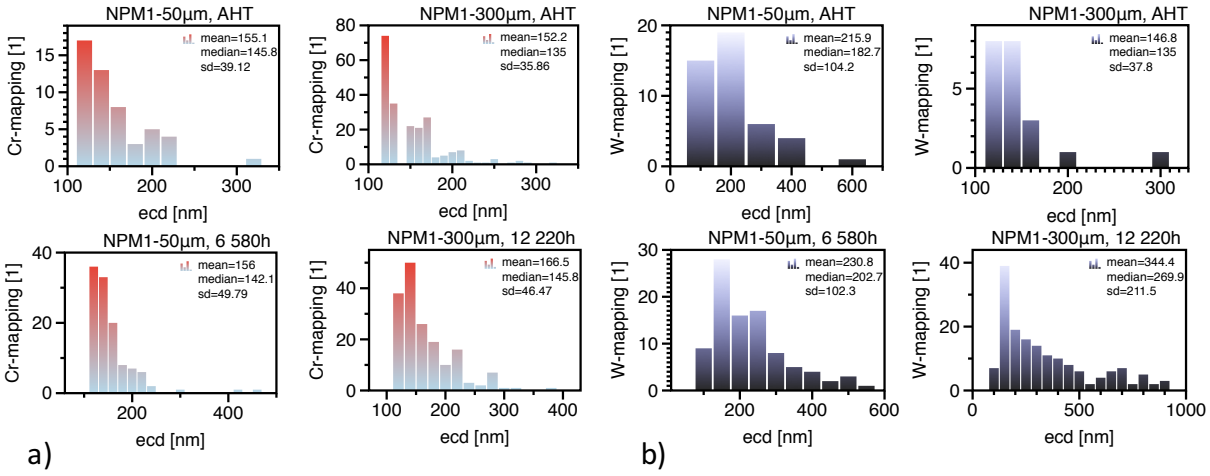

Fig. 55 Histograms of the SEM/EDX mappings Q&P AHT and after the creep rupture tests for a) Cr and b) W of the NPM1-LN-P.

After the results from the precipitates, comparative EBSD measurements are carried out for both steels at a PAGS of 300 µm.

4.4.3 SEM/EBSD of NPM1-LN and FB2-2-LN

Fig. 56 a) – d) and Fig. 57 a) – d) show inverse pole figure (IPF) maps from the EBSD experiments after the Q&T and Q&P HT for the NPM1-LN-P and FB2-2-LN-P steel respectively. Both steels with the two HT are compared at a PAGS of 300 µm with a scanning step-size between 0.4 – 0.5 µm (see sec. 3.5.2).

Comparing the IPF maps of NPM1-LN in Fig. 56 a) (Q&P) with d) (Q&T) at the same magnification, the substructure after Q&P appears larger, which becomes even more obvious in the magnified images in b) and e). The evaluation for the point to point misorientation, compared as grain boundary length is evaluated within three angular classes (5-15, 15-50 and 50-60 deg) and confirms this subjective perception, i.e. larger packet and

block boundaries after the Q&P HT (300x300 µm area for both). The misorientation measurements with KAM for small angle grain boundaries in the range between 0-5 deg for NPM1-LN in c) is fit to a normal distribution and shows a lower value after the Q&P HT i.e. less total dislocation density.

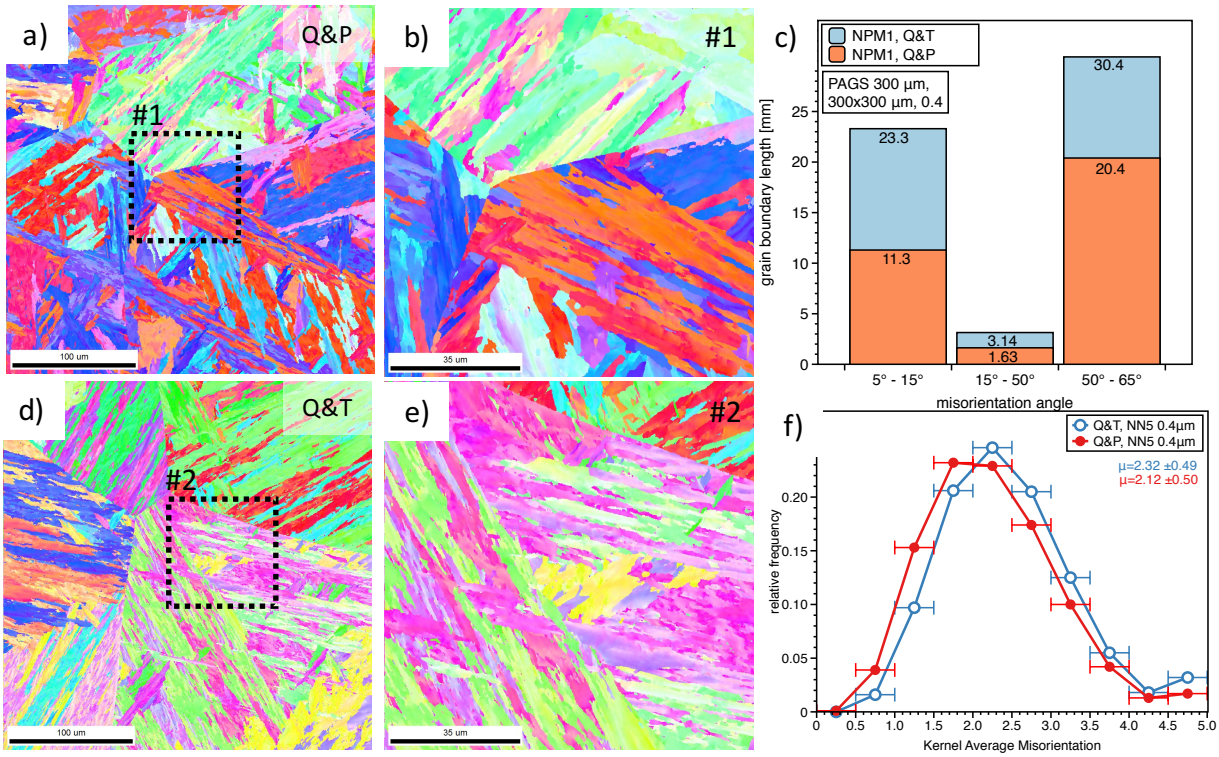

Fig. 56 NPM1-LN-P IPF maps for Q&P (a), b)) and Q&T (d), e)) PAGS of 300 µm. c) Comparison of the grain boundary length between Q&T and Q&P. f) KAM comparison between Q&P and Q&T for low angle grain boundaries.

Similar results are obtained for the FB2-2-LN steel and are illustrated in Fig. 57 a) - f). In comparison to Q&T, Q&P shows lower amount of packet and block boundaries (Fig. 57 c)) and a lower KAM angle (Fig. 57 f)). The reason for plotting the 5th NN for NPM1-LN in Fig. 56 f) and the 4th NN for FB2-2 in Fig. 57 f) was to compare the KAM at a similar scale, despite the different scanning step-size (see Fig. 19). NPM1-LN-P shows a lower KAM angle and by comparing the absolute grain boundary length (compare Fig. 56 c) with Fig. 57 c)), larger packet and block boundaries.

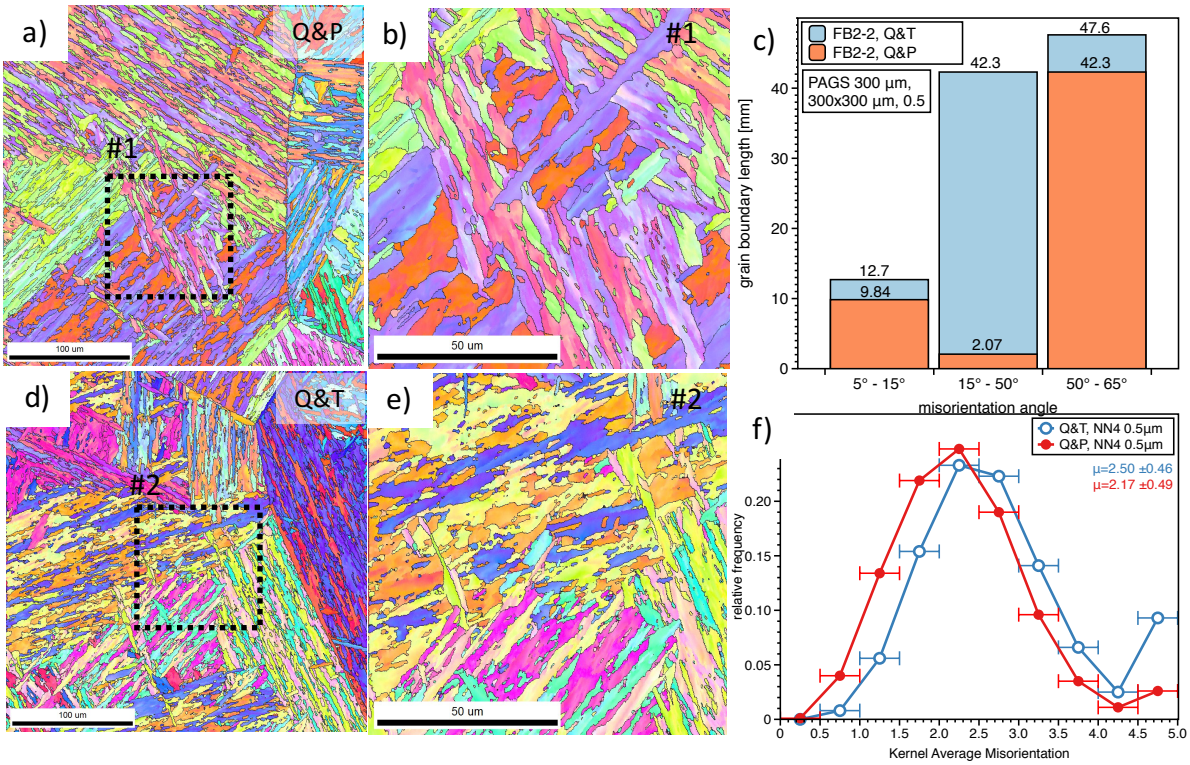

Fig. 57 FB2-2-P IPF maps for Q&P (a), b)) and Q&T (d), e)) at a PAGS of 300 µm. c) Comparison of the grain boundary length between Q&T and Q&P and f) KAM comparison between Q&P and Q&T for low angle grain boundaries.

5 Discussion

The typical microstructure of 9 % Cr heat resistant steels is tempered martensite. The applied Q&P HT combines a displacive with a reconstructive phase transformation and changes the number of interfaces, dislocations and related properties. Therefore, the Q&P HT with different PAGS is studied and compared to a conventional Q&T HT on FB2-2-LN and NPM1-LN steels. The classic X20Cr13 power plant steel is used to demonstrate the reconstructive γ → α phase transformation after

- incomplete solution annealing of chromium carbides (see Paper VIII) and
- during tempering after quenching between M_s and M_f temperature,

to study the interaction between carbide formation.

5.1 Phase transformation and heat treatment

Austenitization of X20Cr13 above the solution temperature of carbides solves higher amounts of C inside the γ solution phase than the solution limit of α. Upon cooling below the A_{r3} temperature the γ does not transform reconstructively to α without sufficient undercooling or time [29]. This delay in reaction kinetics can be attributed to the high amount of Cr and solved C (or equivalents) inside the matrix. The γ matrix needs first to reduce the excess solved C (or equivalents), which can be done through carbide formation at nucleation sites such as the PAGB. Therefore, the reconstructive γ ⟶ α transformation of high Cr steels is not discussed without considering the precipitates, especially carbides and was the reason for the simulations of M_3C carbides for the X20C13 steel in sec. 4.3.2. This idea of increased hardenability and reduction of the amount of C inside the γ matrix through the formation of carbides, might be transferable to other steels (NPM1 and FB2-2) via a physical model and/or expressed in terms of a C equivalent.

The reaction kinetics of the reconstructive γ ⟶ α transformation becomes even slower after further additions of Mn, Ni, Mo, W and B when comparing CCT diagrams between X20Cr13 and NPM1-LN or FB2-2-LN, [29, p. 148], [110], [111]. After complete solution annealing, X20Cr13 forms carbide + α during 30 min of isothermal holding at

~700 °C, while for NPM1-LN it takes longer than 40 h. The PAGB is important for the γ ⟶ α transformation. A smaller PAGS does not affect the incubation time but the nucleation rate and leads to an increased transformation rate [112]. Segregates such as B and Mo delay the nucleation and growth of carbides at the PAGB, but these elements are not found at the later formed α′- α′ block boundaries upon quenching as shown by a study of Li et al. [113]. This is an explanation why the reconstructive γ ⟶ α transformation starts subsequently after partial quenching between M_s and M_f. The presence of these segregating elements at the PAGB decreases the interface energy and retard the nucleation and growth of precipitates and allotriomorphic α to longer times [29], [57].

The volume expansion of α′ formation between M_s and M_f temperature introduces:

- 0-dimensional (D) defects e.g. voids,
- 1-D dislocations,
- 2-D compressive stress, new interfaces, and
- 3-D α′ phase with a different chemical potential compared to γ.

For X20Cr13 the volumetric expansion measured between M_s and M_f temperature is more than 0.72 % (~0.5 % for NPM1 and FB2-2) and must be local (transforming packet or block) of (at least) similar amount. Between M_s and M_f, the microstructure consists out of α′ and deformed γ. The volume expansion of α′ depends on the difference between the thermal expansion coefficients (γ and α) and the distance between A_3 and M_s temperature. The shape deformation dissipates heat, provides interfaces and dislocations for the nucleation of carbides as a necessary prerequisite for the γ → α transformation during tempering. An amount of more than 50 % of α_1' is recommended to create a deformation within each PAG, due the dependency of the M_s on the PAGS [25] and the local composition. If single PAG remain untransformed, lower amounts of nucleation sites cause the formation of large carbides at the PAGB of the untransformed PAG during tempering. A direct increase of the temperature above ~600 °C, forms precipitates (incubation time needed) at the new $\alpha' - \gamma$ interfaces and dislocations inside the γ and α′ and reduces the C inside the γ (as shown by simulations in Fig. 47). Mechanical stabilization starts to recover, the deformed γ transforms into precipitates + α without the need to soak NPM1-LN or FB2-2-LN for 40 h. The kinetics of this transformation is described by JMAK within the temperature range 600 °C – 800 °C (see Paper VI). The fastest rate is found at temper-

ing temperatures between 700 °C and 750 °C for both NPM1-LN and FB2-2-LN. The incubation time for this transformation is assumed to be limited by the kinetics of substitutional elements and is subject of further investigations.

For better oxidation resistance and simpler precipitation behaviour, X20Cr13 steel is studied by in-situ HTLSCM, EBSD and HR-TEM. The HR-TEM results in Fig. 42 a) and Fig. 43 show M_3C carbides [29, p. 89] formed along the former $\gamma-\alpha_1'$ interface with both sides coherent. The crystallographic OR between the M_3C and the tempered α_1' at the one and the reconstructive grown α at the other side are similar. Allotriomorphic α grows coherent from the M_3C and consumes the deformed γ to extend the former $\gamma-\alpha_1'$ boundaries, which is an explanation for the coarser blocks after the Q&P HT and shown by the EBSD results for the NPM1-LN and FB2-2-LN in Fig. 56 and Fig. 57. The initial α_1' interfaces should therefore only become visible by TEM due to their different carbide length and orientation. A shell type build-up of M_3C is observed in the early stages of their formation. These observations show discrete steps (intermediate stages) of M_3C carbide formation:

- dislocation cores enrich with C (Cottrell atmospheres), with a similar lattice parameter to α′ and
- formation of orthorhombic M_3C carbides in the core with a lattice parameter 3 % smaller than the α′ matrix.

The carbides inside the tempered α_1' matrix are surrounded by dislocations and are randomly orientated towards the matrix. The observation of Cottrell atmospheres within the α_1' blocks support the correct assumptions of Galindo-Nava et al. [114].

The acceleration of the $\gamma \longrightarrow \alpha$ transformation is also shown from a different perspective. The desire for a higher thermal stability of carbides (e.g. chromium carbides) results in higher dissolution temperatures, often above the $\alpha \longrightarrow \gamma$ temperature (A_{r3}). This leads not only to the replacement of the carbides from the grain boundaries [115], but also to an increased size with a lower number density. Incomplete solution annealing of precipitates causes lower C contents inside the γ matrix. This accelerates the transformation kinetics as measured by dilatometry and EBSD for the X20Cr13 steel in Paper VIII. There is a high possibility that this plays an important role in application e.g. inside the heat-affected zone of a high Cr steel weld. Martensitic transformations are of course possible at high cooling rates without solved C inside the matrix [59], but the reduction of the M_s temperature by the small AGS (~8 µm) should also be considered in the discussions [25].

The modification of the PAGS has important implications on the number of possible segregation-sites. Elements like As, P, S, Sn, Sb or Si segregate to grain boundaries and might induce reversible (equilibrium segregation) temper embrittlement [116], [117]. The Watanabe (J-Factor), Bruscato Factor are empirical measures for the susceptibility [118]. Different hardening temperatures and times create different PAGS. Ding et al. [119] investigated a 2.25Cr1Mo steel to show a double P content at the PAGB when the PAGS increases from 30 µm to 170 µm (factor of ~6). Upon linear extrapolation, a factor of 14 (50 µm PAGS and 700 µm) would lead to a 4 times higher concentration of segregating elements at the PAGB. The increase in PAGS should therefore only be performed with steels after an appropriate melting and re-melting route.

The mechanical tests, hardness, Charpy-V, tensile and fatigue test results are compared between Q&P HT and Q&T HT at four different PAGS at room temperature. The α, formed during the Q&P HT, has no negative influence on the impact work (see Fig. 31). A mixed microstructure between martensite and bainite (after a Q&P HT) has a positive influence on the impact work [120], while larger PAGS increase the DBTT and decrease the impact work (see Fig. 31 b)) [121], [122]. The hardness and UTS values depend on the shares between the initial transformed amount of α_1' and α after the complete Q&P HT. The hardness drops to minimum values of 80 %, compared to values after the Q&T HT, with a share of ~50 % α and is related to a lower dislocation density as measured by KAM (see Fig. 57 f)) [94]. Similar to the hardness, the UTS and $R_{p0.2}$ values can be related to the lower dislocation density [123], [124]. Kennett et al. [125] show an increase in as-quenched hardness and dislocation density with a decreasing PAGS (10-60 µm); after tempering less recovery and a higher hardness is shown of the larger PAGS on a micro-alloyed steel. No systematic influence of the PAGS on the HV10 hardness is observed in this study. The fatigue tests at room temperature show lower endurance limits after the Q&P HT. Du et al. [126] show that blocks and sub-blocks are barriers for dislocation movement, while the later can be overcome. Therefore, crack formation and slip of dislocations seems to be enhanced after the Q&P HT despite a different study on a 42SiCr steel [127]. Interrupted quenching seems to be affective to prevent pre-damage through hardness cracks especially when the as-quenched α′ has low ductility (high C).

5.2 Creep strength

Specimens with different PAGS are creep tested after the Q&P and Q&T HT. The tests (see Fig. 34) demonstrate an improvement of the creep rupture strength of the NPM1-LN-P and FB2-2-LN-P steels with an increasing PAGS. Comparable results are obtained by Fujita et al. [128]. The increase in creep rupture strength with an increasing PAGS is attributed to the lower number of grain boundaries (less recovery sites), though no systematic influence on the HV10 hardness is observed. Morito et al. [26] show a linear relationship between the larger PAGS, larger packet and block width. A high amount of grain boundaries provide fast diffusional pathways for microstructure degradation [26] and have more space for segregating elements [129]. A PAGS of 300 µm results in the longest creep rupture times, which is different to the observations from Kimura [130] who showed the maximum at lower PAGS. The reasons for the differences are probably related to the different chemical composition, the applied loading conditions by using a different testing diameter, the manufacturing route and/or to the number of segregating elements to the PAGB. Increasing the PAGS from 100 µm to 700 µm changes the failure mechanism from transgranular ductile to intergranular brittle which is shown in Paper IV. This must be avoided for steels in service. Despite the lower measured area fraction of creep pores and number density for a PAGS of 700 µm (see Fig. 35 b) and Fig. 36 b)), the orientation of creep cavities to form larger transgranular cracks is easier at large interfaces such as the PAGB and is the reason for the loss in rupture ductility and sudden brittle fracture.

Comparing the creep strength among the applied HT, the Q&P HT process additionally improves the creep rupture times by more than 50 % and reduces the sensitivity of the PAGS to the creep rupture ductility through the flatter slope in Fig. 35 a). The ductility is positively affected by the larger substructure after the Q&P HT but negatively by a larger PAGS. This supports the view, that dislocation motion during the creep life is limited by the PAGB. During creep exposure, precipitates, packet, block and sgb coarse and recover [94]. The secondary creep regime (transient creep) is described as coarsening of martensite laths and sub-grains [65], while the onset of the tertiary creep regime (accelerated creep) is described as recovery and coarsening of block and packet boundaries [65]. This supports the view, that a lower number of interfaces and dislocations in the AHT condition lead to less recovery effects and a lower secondary creep rate $\dot{\varepsilon}_s$. The larger the hardness drop of the AHT specimens with respect to the creep exposed specimens

treated with the Q&T HT compared to the Q&P HT again support the previous view, because the local misorientation measured by e.g. KAM between 0-5 deg is proportional to the HV10 values in AHT stage [94] (compare Fig. 28 with Fig. 56, Fig. 57 and Fig. 29). This suggests that the number of interfaces and dislocations between Q&P and Q&T HT after creep exposure becomes smaller. Systematic EBSD experiments for the same PAGS after Q&P and Q&T HT need to be conducted at similar creep exposure times to confirm that.

The principal hardening mechanism of tempered martensitic steels for creep is "precipitate stabilized substructure hardening" [61]. Stable precipitates are literally the backbone of ferritic/martensitic steels to provide obstacles, pin dislocations and grain boundaries to decelerate their recovery during creep exposure [131]. Fig. 58 summarizes the measured sizes of precipitates investigated by a) TEM and b) SEM from the histograms in the results section. Precipitates in 9 % Cr steels prevent recovery during tempering and creep exposure. Despite different solution annealing temperatures (1100 °C and 1150 °C both for 30 min), the size distributions of precipitates for the NPM1-LN-P steel after TEM investigations (see Fig. 53 a)) show similar values for precipitates treated with the Q&P and Q&T HT in AHT condition. The main difference among Q&P and Q&T HT are the precipitation domains, $\alpha'+\gamma$ and α' respectively, during the first tempering. The $M_{23}C_6$ measured by TEM contain ~4 at% of W (~4 at% of Mo for FB2-2-LN-P) and are both of comparable size as shown by Abe [109]. The composition of $M_{23}C_6$ in FB2-2-LN-P is similar but the ecd is smaller compared to the observations of Aghajani et al. [132] on a 12 % Cr steel. The higher tempering temperatures (770 °C for 2 h) lead to larger MX and $M_{23}C_6$ precipitates in AHT condition as studied by Gustafson [133] on a P92 steel. The applied stress increases the recovery rate [132] but shows no measurable difference on the coarsening of precipitates within the 6 580 h of creep exposure. The size distributions of precipitates within the head and gauge section after 6 580 h of creep exposure at 650 °C from NPM1-LN-P (compare Fig. 50 b) with c)) are also similar. The creep exposure time seems therefore be too short for a measurable effect of stress on precipitate coarsening as observed by Eggeler [61]. Similar to TEM, the SEM measurements in Fig. 58 b) show coarsening of Laves Phase and $M_{23}C_6$. Compared to the ecd evaluated by TEM, the SEM ecd values for $M_{23}X_6$ are ~100 nm larger. The resolution limit of ~100 µm increases the ecd of $M_{23}X_6$ and Laves Phase precipitates and does not allow observing small MX precipitates but therefore a larger area. The SEM-EDX results for the area fraction of all precipitates evaluated from the Fe map (see Table 7) shows a higher amount of precipitates for the NPM1-LN

steel which disagrees to the evaluations from equilibrium simulations (see Fig. 12). The simulations predict a phase fraction of 3.5 % $M_{23}X_6$ (0.85 % of Laves Phase) for the FB2-2-LN steel which is much larger compared to the 1.5 % (2.5 % of Laves Phase) for the NPM1-LN steel at 500 °C. The evaluated area fraction of Laves Phase (see Table 7) from the W and Mo map qualitatively agree to the equilibrium simulation, but the Cr map from the SEM-EDX experiments for Cr-precipitates in FB2-2-LN-P steel experiments show lower amounts of $M_{23}X_6$ precipitates compared to NPM1-LN-P. This disagreement needs to be further investigated, because the Cr-map from the TEM investigations for the FB2-2-LN-P AHT (see Fig. 53 a)) shows larger ecd of Cr precipitates compared to NPM1-LN. These precipitates should therefore be easier to detect within the SEM-EDX equipment compared to the NPM1-LN-P steel. An explanation is that the major amount of the size distribution of $M_{23}X_6$ stays below an ecd of 100 nm. Another reason might be the lower Si content of FB2-2-LN (0.2 compared to 0.35 wt.% for NPM1), which is reported to have a strong influence on the formation of carbides, Laves Phase and the corrosion resistance [29], [60], [134]. Both, TEM investigations and recorded SEM spectra and mappings indicate that not every Laves Phase precipitate contains Si, which is different to the observations of Isik et al. [134] for a 11.7 wt.% Cr steel.

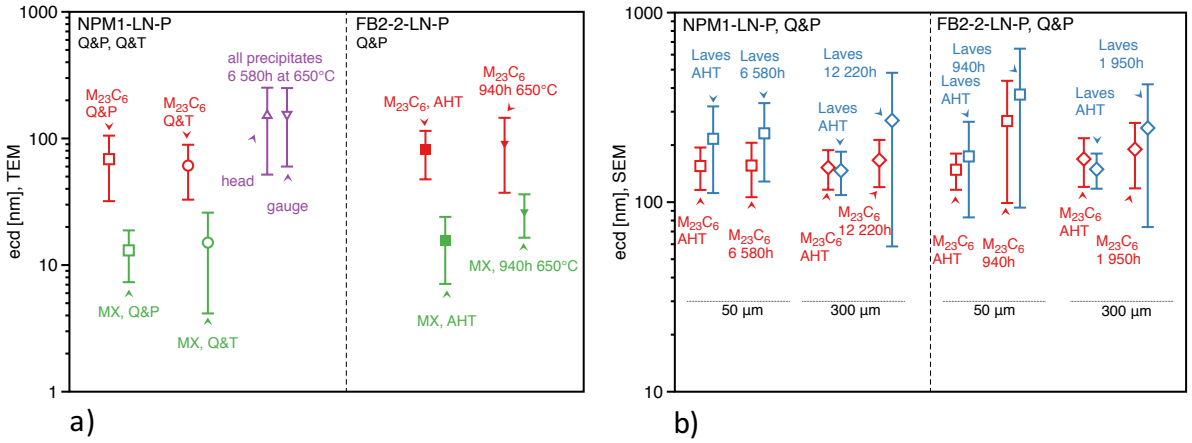

Fig. 58 Equivalent circle diameter (ecd) with one standard deviation of $M_{23}C_6$, MX and Laves Phase precipitates measured by a) TEM and b) SEM from the histograms Fig. 49, Fig. 50 b) – c), Fig. 53 and Fig. 54, Fig. 55.

A decreasing number density of precipitates leads to a loss of Orowan strengthening, less climb of dislocations and hence to faster recovery. A reduced number density of precipitates has a negative effect on the Orowan stress, which is incorporated into the back-stress model to predict the creep rupture life [63], [135], [136]. However, the contribution

of sgb hardening and dislocation hardening at high temperatures should be reviewed because a higher number of sgb increases the internal energy, promotes recovery of free lattice dislocations [137] by either annihilation or rearrangement [138] and leads therefore to coarser sgb [132]. In this context sgb refer to all low-angle grain boundaries e.g. sub-block boundaries. Based on the model of Yadav et al. [139] their contribution to an increased creep- and recovery rate in the presence of temperature plus an external stress field should also be subject for additional works.

The main reasons for the lower creep rupture strength of FB2-2-LN compared to NPM1-LN can basically be related to the different chemical composition (C, Co, Si, Mo, W, Mn; see Table 1). FB2-2-LN shows a lower total amount of precipitates (also $M_{23}X_6$, see Table 7), a higher amount of dislocations and interfaces (packet or block boundaries) due to the higher C content and the related larger shape deformation [29] and/or the simulated lower thermal stability of Laves Phase. The reason for the improved creep rupture strength after the Q&P HT within the first 10,000 h of creep exposure for both steels is attributed to less recovery due to a lower AHT total dislocation density and a lower number of interfaces. Creep strength simulations by considering precipitates only seem therefore not to be completely correct and need to be further improved to allow a dynamic change of the precipitation domain to consider recovery effects and the contribution of creep pores, which are the reason for the fracture. If the minimum creep rate could be simulated, the total creep life can be predicted through e.g. the Monkman-Grant relation [65].

The Q&P HT increases creep rupture ductility of both steels. A total creep strain of 1 % or 2 % is often regarded as design limits for components in service. Paper IX shows, that these marks are reached between 70 % - 90 % of the creep rupture time and depend on the PAGS. An increasing PAGS has not only the benefit of longer creep rupture times, but also longer times below the 1 % or 2 % strain limits. However, the brittle rupture and segregations which result from the manufacturing route should be considered. FB2-2 shows higher creep rupture ductility despite lower measured area fraction of creep pores.

6 Summary and Conclusion

The PAGS and the martensitic substructure of two selected B alloyed 9 % Cr steels, NPM1-LN and FB2-2-LN are improved for application at 650 °C by different austenitizing conditions, by a Q&P HT [21], [22] compared to a conventional Q&T HT. Additionally, to exclude effects and interactions of alloy elements, a classic power plant steel X20Cr13 was used to study interactions between carbide formation and the reconstructive γ → α phase transformation. The applied HT affect the microstructure related mechanical properties and can be used to optimize the creep properties.

Mechanical- and creep properties

- The selected Q&P HT does not influence the Charpy-V impact work.
- Q&P reduces the hardness, UTS strength and the fatigue limit at RT.
- A PAGS between 100 µm and 300 µm provides a good compromise between creep rupture time and ductility for NPM1-LN-P and FB2-2-LN-P.
- Q&P (α_1'>50 %) increases the creep rupture time for each PAGS on average by more than 50 % for exposure times less than 10,000 h.
- Q&P reduces the dependence of the PAGS on the creep rupture strain.
- The Q&P HT is expected to improve the creep properties of an entire class of 8-13 % Cr steels and is supported by different observations [23], [110].

Microstructure properties

- Q&P opens the possibility to accelerate the reconstructive transformation of RA into α and precipitates at tempering temperatures between 650 – 800 °C.
- Dislocations and interfaces formed during partial quenching (α_1') provide the nucleation sites inside the prior austenite grain, promote the formation of precipitates as a first - allotriomorphic and idiomorphic α as a second step.
- Q&P coarsens the initial martensitic substructure (α_1') with lower number of subgrain boundaries and a lower total dislocation density, measured by KAM.
- Therefore, α_1'/γ interface must move in order to transform reconstructively from γ to α.

- Interphase precipitation might occur to leave a more random orientation of precipitates [140] inside the transformed α.
- The size and chemical composition of precipitates is not different compared to precipitates treated with the conventional Q&T HT.
- The lower total dislocation density in AHT condition leads to a reduced internal energy and hence less recovery effects during creep and a lower creep rate.

Comparison between NPM1-LN and FB2-2-LN

- The comparison of the two tested steels at similar conditions (650 °C, 150 MPa), shows six times longer creep rupture times of NPM1-LN.
- FB2-2-LN shows a higher number of interfaces and a higher total dislocation density in AHT condition, which is due to the 10 – 20 °C lager undercooling between M_s and A_{c3} temperature.
- The faster recovery of FB2-2-LN during creep exposure is shown by a larger hardness drop.
- Compared to AHT condition, both steels show coarsening of $M_{23}X_6$ and Laves Phase within the first 10.000 h of creep exposure.
- W (NPM1) replaces Mo (FB2-2) in Laves Phase and $M_{23}X_6$ to similar amounts (~4 at.%).
- NPM1-LN shows a 10-20 nm smaller AHT size of $M_{23}X_6$.
- FB2-2-LN has superior creep properties compared to P92 [76].
- NPM1-LN-P is a more than competitive steel to P93 [77].
- Finally, an interruption of the quenching process in high Cr steels makes sense even after the formation of more than 90 % of α_1'. The interruption avoids damage of the un-tempered, initial-formed α_1' caused by the transforming mechanical stabilized RA. If the lower tensile, hardness and fatigue limit values present no problem for the component at RT, there should not be a reason for not using this Q&P HT for application at high temperatures, where diffusional and recovery processes limit the service life.

7 Outlook

Comparative creep tests and creep fatigue tests after the Q&P and Q&T HT at different temperatures and stresses for different 9 % steels should be carried out to confirm the improvement with the Q&P HT.

Comparative EBSD measurements on specimen heat treated with Q&T and Q&P should be carried out after interrupted creep exposure at similar temperatures and times.

The Q&P HT should be tested for tempering temperatures between 600 °C and M_s temperature, to gradually limit the diffusion of substitutional and interstitial elements, to recover the RA and α_1' from the shape deformation of α_1' and to relate this effect to the M_s temperature. Parallel to that, the effect of segregating elements on the impact toughness should be investigated.

In-situ synchrotron experiments should be carried out to illustrate the formation of α, the coarsening of the initially formed α_1' blocks, recovery of dislocations and the nucleation and growth of precipitates during the Q&P HT. The results should be correlated to results from dilatometry and electron microscopy.

The dependence of the orientation-relation between matrix and precipitates formed during the Q&P and Q&T should be compared and studied on a 9 % Cr containing model steel. Studies on the evolution of interphase precipitation during the Q&P HT are suggested.

The kinetics of the reconstructive and displacive phase transformations in high Cr steels should be attempted to be simulated and related to the nucleation, aging and dissolution of precipitates to support a comprehensive understanding during HT and welding processes.

The effect of the Q&P HT on welds should be investigated.

Surface sensitive in-situ observation methods e.g. high temperature X-ray diffraction, high temperature EBSD or LSCM are often influenced by the different stress state. This influence should be systematically studied and compared to observations in the volume.

For the future it is expected that this Q&P HT will be used in current and future 8-13 % Cr steels to create microstructures, which are more stable at elevated temperatures.

8 Literature

[1] I. Wallerstein, *The modern world-system I: capitalist agriculture and the origins of the European world-economy in the sixteenth century, with a new prologue*, vol. 1. University of California Press, 2011.

[2] A. Amirabedini, "Two development theories: Ibn-i-Khaldoun and Wallerstein," *Campus-Wide Inf. Syst.*, vol. 31, no. 1, pp. 63–74, Dec. 2013.

[3] C. Chase-Dunn, Y. Kawano, and B. D. Brewer, "Trade Globalization since 1795: Waves of Integration in the World-System," *Am. Sociol. Rev.*, vol. 65, no. 1, p. 77, Feb. 2000.

[4] M. F. Ashby, *Materials and Sustainable Development*. Elsevier, 2016.

[5] EIA, "Annual Energy Outlook 2014 with projections to 2040," *Report*, 2014. [Online]. Available: http://www.eia.gov/forecasts/aeo/pdf/0383%25282014%2529.pdf. [Accessed: 13-May-2016].

[6] IEA, "World Energy Oulook 2015," 2015.

[7] M. F. Ashby, "Data, Charts and Databases," in *Materials and Sustainable Development*, Elsevier, 2016, pp. 241–258.

[8] S. Paul, G. Zeiler, A. Putschögl, and E. Plesiutschnig, "Turbine Components of High Creep Resistant MARBN Steels for Modern High Efficient Fossil-Fired Power Plants," in *Power-Gen Europe*, 2014, p. 14.

[9] G. Zeiler, S. Paul, and E. Plesiutschnig, "9-10% Cr steel forgings for USC turbines – experiences in manufacturing and development status of MARBN steels," in *8th International Conference on Advances in Materials Technology for Fossil Power Plants*, 2016, p. 12.

[10] F. Abe, "Effect of Boron on Microstructure and Creep Strength of Advanced Ferritic Power Plant Steels," *Procedia Eng.*, vol. 10, pp. 94–99, Jan. 2011.

[11] H. Semba and F. Abe, "Alloy design and creep strength of advanced 9%Cr USC boiler steels containing high concentration of boron," *Energy Mater.*, vol. 1, no. 4, pp. 238–244, Dec. 2006.

[12] F. Abe, M. Tabuchi, and S. Tsukamoto, "Mechanisms for boron effect on microstructure and

creep strength of ferritic power plant steels," *Energy Mater. Mater. Sci. Eng. Energy Syst.*, vol. 4, no. 4, pp. 166–174, Mar. 2012.

[13] P. Mayr, "Appendix:Evolution of microstructure and mechanical properties of the heat affected zone in B-containing 9% chromium steels," Graz University of Technology, 2007.

[14] Harry Chandler, *Heat Treater's Guide: Practices and Procedures for Irons and Steels*, 2nd ed. ASM International, 1995.

[15] Harry Chandler, *Heat Treater's Guide: Practices and Procedures for Irons and Steels*, 2nd ed. ASM International, 1995.

[16] W. Gong, Y. Tomota, M. S. Koo, and Y. Adachi, "Effect of ausforming on nanobainite steel," *Scr. Mater.*, vol. 63, no. 8, pp. 819–822, 2010.

[17] L. Shao, D. Jiang, and J. Gong, "Nanoindentation Characterization of the Hardness of Zirconia Dental Ceramics," *Adv. Eng. Mater.*, vol. 15, no. 8, pp. 704–707, Aug. 2013.

[18] W. Gong, Y. Tomota, Y. Adachi, A. M. Paradowska, J. F. Kelleher, and S. Y. Zhang, "Effects of ausforming temperature on bainite transformation, microstructure and variant selection in nanobainite steel," *Acta Mater.*, vol. 61, no. 11, pp. 4142–4154, 2013.

[19] R. Honeycombe and F. Pickering, "Ferrite and bainite in alloy steels," *Metall. Trans.*, vol. 3, pp. 1972–1099, 1972.

[20] R. L. Klueh, "Elevated- Temperature Ferritic and Martensitic Steels and their Application to Future Nuclear Reactors," Oak Ridge, 2004.

[21] D. V. Edmonds, K. He, F. C. Rizzo, B. C. De Cooman, D. K. Matlock, and J. G. Speer, "Quenching and partitioning martensite—A novel steel heat treatment," *Mater. Sci. Eng. A*, vol. 438–440, pp. 25–34, Nov. 2006.

[22] J. Speer, D. K. Matlock, B. C. De Cooman, and J. G. Schroth, "Carbon partitioning into austenite after martensite transformation," *Acta Mater.*, vol. 51, no. 9, pp. 2611–2622, 2003.

[23] M. Tamura, T. Kumagai, K. Sakai, K. Shinozuka, and H. Esaka, "A new approach to improve creep resistance of high Cr martensitic steel," *J. Nucl. Mater.*, vol. 417, no. 1–3, pp. 29–32, 2011.

[24] T. C. Totemeier, H. Tian, and J. a. Simpson, "Effect of normalization temperature on the creep strength of modified 9Cr-1Mo steel," *Metall. Mater. Trans. A*, vol. 37, no. 5, pp. 1519–1525, 2006.

[25] H. Yang and H. Bhadeshia, “Austenite grain size and the martensite-start temperature,” *Scr. Mater.*, vol. 60, no. 7, pp. 493–495, Apr. 2009.

[26] S. Morito, H. Yoshida, T. Maki, and X. Huang, “Effect of block size on the strength of lath martensite in low carbon steels,” *Mater. Sci. Eng. A*, vol. 438–440, pp. 237–240, Nov. 2006.

[27] M. Hillert, *Phase Equilibria, Phase Diagrams and Phase Transformations*, 2nd ed. Cambridge: Cambridge University Press, 2007.

[28] P. Atkins and J. De Paula, *Atkins Physical Chemistry*, 8th ed. Oxford, UK: Oxford University Press, 2006.

[29] H. Bhadeshia and R. Honeycombe, *Steels: Microstructure and Properties*, 3rd ed. Elsevier Ltd, 2006.

[30] M. F. Ashby and D. R. H. Jones, *Engineering materials 2 An Introduction to Microstructures, Processing and Design*. Cambridge, U.K.: Pergamon Press, 1992.

[31] L. Yuan, “Nanoscale austenite reversion through partitioning, segregation and kinetic freezing in martensitic stainless steels,” Rheinisch-Westfälischen Technischen Hochschule Aachen, 2012.

[32] C. Simsir and H. Gür, “Handbook of thermal process modeling of steels,” in *International Heat Treatment and Surface Engineering*, H. Gür and J. Pan, Eds. Taylor & Francis Group, LLC, 2009, pp. 341–426.

[33] G. Gottstein, *Physikalische Grundlagen der Materialkunde*. Berlin, Heidelberg: Springer Verlag, 2007.

[34] I. Leonov, A. I. Poteryaev, Y. N. Gornostyrev, a I. Lichtenstein, M. I. Katsnelson, V. I. Anisimov, and D. Vollhardt, “Electronic correlations determine the phase stability of iron up to the melting temperature,” *Sci. Rep.*, vol. 4, pp. 1–8, Jul. 2014.

[35] B. Sonderegger, “Charakterisierung der Substruktur in modernen 9-12% Cr Stählen mittels der EBSD Methode,” Graz University of Technology, 2005.

[36] S. Morooka, Y. Tomota, Y. Adachi, S. Morito, and T. Kamiyama, “Hierarchical Characterization by EBSD and Neutron Diffraction on Heterogeneous Deformation Behavior of a Martensitic Steel,” *Tetsu-to-Hagane*, vol. 94, no. 8, pp. 313–320, 2008.

[37] S. Morito, Y. Adachi, and T. Ohba, “Morphology and Crystallography of Sub-Blocks in Ultra-Low Carbon Lath Martensite Steel,” *Mater. Trans.*, vol. 50, no. 8, pp. 1919–1923, 2009.

[38] L. Norström, “On the Yield Strength of Quenched Low-carbon Lath Martensite,” *Scand. J. Metall.*, vol. 5, pp. 159–165, 1976.

[39] L. Norström, “The relation between microstructure and yield strength in tempered low-carbon lath martensite with 5% nickel,” *Met. Sci.*, 1976.

[40] M. Yaso, S. Morito, T. Ohba, and K. Kubota, “Microstructure of martensite in Fe–C–Cr steel,” *Mater. Sci. Eng. A*, vol. 481–482, pp. 770–773, May 2008.

[41] Z. Cong and Y. Murata, “Dislocation Density of Lath Martensite in 10Cr-5W Heat-Resistant Steels,” *Mater. Trans.*, vol. 52, no. 12, pp. 2151–2154, 2011.

[42] F. J. Humphreys and M. Hatherly, *Recrystallization and Related Annealing Phenomena*. 2004.

[43] R. Bürgel, *Festigkeitslehre und Werkstoffmechanik*, 1st ed. Wiesbaden, Germany: Vieweg & Sohn Verlag/GWV Fachverlage GmbH, 2005.

[44] J. Pešička, R. Kužel, a. Dronhofer, and G. Eggeler, “The evolution of dislocation density during heat treatment and creep of tempered martensite ferritic steels,” *Acta Mater.*, vol. 51, no. 16, pp. 4847–4862, Sep. 2003.

[45] G. Krauss, “Martensite in steel: strength and structure,” *Mater. Sci. Eng. A*, vol. 273–275, pp. 40–57, Dec. 1999.

[46] P. HAASEN†, “MECHANICAL PROPERTIES OF SOLID SOLUTIONS,” in *Physical Metallurgy*, Elsevier, 1996, pp. 2009–2073.

[47] V. Läpple, *Wärmebehandlung des Stahls*, 10th ed. Haan-Gruiten: Verl. Europa-Lehrmittel Nourney, Vollmer, 2010.

[48] T. Massalski, “Structure and Stability of Alloys,” in *Physical Metallurgy*, vol. 20, no. 2, Elsevier, 1996, pp. 135–204.

[49] Y. Li, Y. Gao, B. Xiao, T. Min, Y. Yang, S. Ma, and D. Yi, “The electronic, mechanical properties and theoretical hardness of chromium carbides by first-principles calculations,” *J. Alloys Compd.*, vol. 509, no. 17, pp. 5242–5249, 2011.

[50] Z. Q. Lv, Z. F. Zhang, Q. Zhang, Z. H. Wang, S. H. Sun, and W. T. Fu, “Structural, electronic and elastic properties of the Laves phases WFe2, MoFe2, WCr2 and MoCr2 from first-principles,” *Solid State Sci.*, vol. 56, pp. 16–22, 2016.

[51] E. Kozeschnik and E. Povoden-Karadeniz, “MatCalc.” Prof. Kozeschnik, Vienna, p. Database Fe

Version 2.039, 1997.

[52] E. Karadeniz, "mc_fe_v2.039.tdb and mc_fe_v2.005.ddb for thermokinetic precipitation simulations using MatCalc." unpublished, Vienna.

[53] M. V Kral, *Proeutectoid ferrite and cementite transformations in steels*, vol. 1. Woodhead Publishing Limited, 2012.

[54] J. Christian, *The Theory of Transformations in Metals and Alloys*, 3rd ed. Oxford, UK: Pergamon Press, 2003.

[55] J. S. Braithwaite and P. Rez, "Grain boundary impurities in iron," *Acta Mater.*, vol. 53, no. 9, pp. 2715–2726, 2005.

[56] E. Wachowicz and A. Kiejna, "Effect of impurities on grain boundary cohesion in bcc iron," *Comput. Mater. Sci.*, vol. 43, no. 4, pp. 736–743, 2008.

[57] M. Strangwood, "Fundamentals of ferrite formation in steels," in *Phase Transformations in Steels*, Elsevier, 2012, pp. 187–224.

[58] H. Bhadeshia, *Bainite in steels*, 2nd ed. Cambridge, U.K.: Cambridge University Press, 2001.

[59] F. Brühl, R. Diederichs, S. Geisler, L. Gerlach, H. Gorgeneck, C. Herzig, F. Hippenstiel, U. Lorenz, S. Myslowicki, T. Myslowicki, M. Pant, G. Pariser, G. Picht, and J. Staudte, *Werkstoffkunde Stahl für Studium und Praxis*, 3rd ed. Aachen: Verlag Mainz, Wissenschaftsverlag, Aachen, 2010.

[60] E. Houdremont, *Handbuch der Sonderstahlkunde*, 2nd ed. Berlin, Heidelberg: Springer Berlin Heidelberg, 1956.

[61] G. Eggeler, "The effect of long-term creep on particle coarsening in tempered martensite ferritic steels," *Acta Metall.*, vol. 37, no. 12, pp. 3225–3234, Dec. 1989.

[62] M. F. Ashby and B. F. Dyson, "CREEP DAMAGE MECHANICS AND MICROMECHANISMS," in *Fracture 84*, no. March, Elsevier, 1984, pp. 3–30.

[63] R. Bürgel, H. Jürgen Maier, and T. Niendorf, *Handbuch Hochtemperatur- Werkstofftechnik*, 4th ed. Wiesbaden: Vieweg+Teubner, 2011.

[64] E. Plesiutschnig, C. Beal, S. Paul, G. Zeiler, and C. Sommitsch, "Optimised microstructure for increased creep rupture strength of MarBN steels," *Mater. High Temp.*, vol. 32, no. 3, pp. 318–322, May 2015.

[65] F. Abe, "Effect of quenching, tempering, and cold rolling on creep deformation behavior of a

tempered martensitic 9Cr-1W steel," *Metall. Mater. Trans. A*, vol. 34, no. 4, pp. 913–925, Apr. 2003.

[66] G. Dieter and D. Bacon, *Mechanical metallurgy*, SI Metric. London: McGraw-Hill book company, inc., 1988.

[67] E. E. Badiyan and A. F. Sirenko, "An investigation of the substructural changes accompanying high-temperature creep of mono- and polycrystalline nickel samples," *J. Mater. Sci.*, vol. 6, no. 12, pp. 1479–1485, Dec. 1971.

[68] G. Webster and R. Ainsworth, *High temperature component life assessment*. Chapman & Hall, 1994.

[69] L. Kloc and V. Sklenička, "Transition from power-law to viscous creep behaviour of p-91 type heat-resistant steel," *Mater. Sci. Eng. A*, vol. 234–236, pp. 962–965, Aug. 1997.

[70] J. Cadek, "Creep in Metallic Materials," *Mater. Sci. Monogr.*, 1988.

[71] G. Dimmler, P. Weinert, and H. Cerjak, "Inverstigations and analysis on the stationary crep behaviour of 9-12% Chromium ferritic martensitic steels," in *Materials for Advanced Power Engineering 2002*, 2002, vol. 21, pp. 1539–1550.

[72] R. L. Stocker and M. F. Ashby, "On The Empirical Constants In The Dorn Equation," *Scr. Metall.*, vol. 7, no. 1, pp. 115–120, Jan. 1973.

[73] N. M. Ghoniem, G. Po, and S. Sharafat, "Deformation mechanisms in ferritic/martensitic steels and the impact on mechanical design," *J. Nucl. Mater.*, vol. 441, no. 1–3, pp. 704–712, Oct. 2013.

[74] J. Čadek, "The back stress concept in power law creep of metals: A review," *Mater. Sci. Eng.*, vol. 94, no. C, pp. 79–92, Oct. 1987.

[75] G. Dimmler, "Quantification of creep resistance and creep fracture strength of 9-12%Cr steels on microstructural basis," Graz University of Technology, 2003.

[76] NIMS, "P92 Creep data sheet," Tsukuba.

[77] F. Masuyama, "Introduction to New Miracle Steel P93," in *Flexible Operation & Preservation of Power Plants - Design, Materials, Operation & Cost Issues*, 2015.

[78] NIMS, "P92 Creep data sheet," Tsukuba.

[79] TA and Instruments, *DIL 805A/D Dilatometer*. USA: TA Instruments, 2016, p. 1.

[80] D. Koistinen and R. Marburger, “A general equation prescribing the extent of the austenite-martensite transformation in pure iron-carbon alloys and plain carbon steels,” *Acta Metall.*, 1959.

[81] S.-J. Lee and Y.-K. Lee, “Finite element simulation of quench distortion in a low-alloy steel incorporating transformation kinetics,” *Acta Mater.*, vol. 56, no. 7, pp. 1482–1490, Apr. 2008.

[82] N. GmbH, “Nabertherm HTC 08/14,” 2016. [Online]. Available: http://www.nabertherm.de. [Accessed: 12-Jul-2016].

[83] P. J. Ennis and A. Czyrska-Filemonowicz, “Recent advances in creep-resistant steels for power plant applications,” *Sadhana*, vol. 28, no. 3–4, pp. 709–730, Jun. 2003.

[84] G. Petzow, *Metallographisches, keramographisches, plastographisches Ätzen*. Borntraeger, 1994.

[85] P. J. Alberry and W. K. C. Jones, “Diagram for the prediction of weld heat-affected zone microstructure,” *Met. Technol.*, vol. 4, no. 1, pp. 360–364, Jan. 1977.

[86] D. Gandy, “The Grade 22 Low Alloy Steel Handbook,” Palo Alto, 2005.

[87] B. Heine, *Werkstoffprüfung*, 2nd ed. München: Carl Hanser Verlag GmbH & Co. KG, 2011.

[88] Paar Anton GmbH, “HTK 1200N,” 2016. [Online]. Available: http://www.anton-paar.com/at-de/produkte/details/hochtemperaturkammer-htk-1200n-ofenkammer/. [Accessed: 05-May-2016].

[89] C. A. Schneider, W. S. Rasband, and K. W. Eliceiri, “NIH Image to ImageJ: 25 years of image analysis,” *Nature Methods*, vol. 9, no. 7. pp. 671–675, 2012.

[90] M. Marvin, “Microscopy apparatus,” US 3013467 A, 1961.

[91] I. Sohn and R. Dippenaar, “In-Situ Observation of Crystallization and Growth in High-Temperature Melts Using the Confocal Laser Microscope,” *Metall. Mater. Trans. B*, Apr. 2016.

[92] G. Ernst, “Private Communications,” Leoben, Austria, 2016.

[93] EDAX, “Orientation Imaging Microscopy (OIM™) Data Analysis.” EDAX, Mahwah, N.J., USA, pp. 1–3, 2015.

[94] K. Fujiyama, K. Mori, D. Kaneko, H. Kimachi, T. Saito, R. Ishii, and T. Hino, “Creep damage assessment of 10Cr-1Mo-1W-VNbN steel forging through EBSD observation,” *Int. J. Press. Vessel. Pip.*, vol. 86, no. 9, pp. 570–577, Sep. 2009.

[95] N.-N. E. and P. K. S. Zaefferer, “Electron backscatter diffraction (EBSD) techniques for studying phase transformations in steels,” vol. d, pp. 557–587, 2012.

[96] J. Ayache, L. Beaunier, J. Boumendil, G. Ehret, and D. Laub, *Sample Preparation Handbook for Transmission Electron Microscopy*. New York, NY: Springer New York, 2010.

[97] R. J. Young and M. V. Moore, “Dual-Beam (FIB-SEM) Systems,” in *Introduction to Focused Ion Beams*, Boston: Kluwer Academic Publishers, pp. 247–268.

[98] FELMI, “FIB/SEM Dual Beam Microscope FEI NOVA200,” *Web-page*, 2016. [Online]. Available: FIB/SEM Dual Beam Microscope FEI NOVA200. [Accessed: 31-Jul-2016].

[99] M. Albu, “private communcations.” Graz, 2016.

[100] P. Schlossmacher, D. O. Klenov, B. Freitag, and H. S. von Harrach, “Enhanced Detection Sensitivity with a New Windowless XEDS System for AEM Based on Silicon Drift Detector Technology,” *Micros. Today*, vol. 18, no. 4, pp. 14–20, Jul. 2010.

[101] A. Gubbens, M. Barfels, C. Trevor, R. Twesten, P. Mooney, P. Thomas, N. Menon, B. Kraus, C. Mao, and B. McGinn, “The GIF Quantum, a next generation post-column imaging energy filter,” *Ultramicroscopy*, vol. 110, no. 8, pp. 962–970, 2010.

[102] R. D. Doherty, “Diffusive Phase Transformations in the Solid State,” in *Physical Metallurgy*, 4th ed., Elsevier B.V., 1996, pp. 1363–1505.

[103] S. Furukawa, H. Ihara, Y. Murata, Y. Tsukada, and T. Koyama, “Simulation of dislocation recovery in lath martensite steels using the phase-field method,” *Comput. Mater. Sci.*, vol. 119, pp. 108–113, 2016.

[104] E. Plesiutschnig, C. Beal, C. Sommitsch, S. Paul, and G. Zeiler, “Ferritic phase transformation to improve creep properties of martensitic high Cr steels,” *Scr. Mater.*, vol. 122, pp. 98–101, Sep. 2016.

[105] E. Plesiutschnig, M. Dikovits, D. Prodinger, C. Sommitsch, S. Wallner, and G. Zeiler, “Relation between prior austenite grain size creep rupture life and pore evolution of 9% Cr steels,” in *11. Tagung Gefüge & Bruch*, 2015, p. P26.

[106] E. Plesiutschnig, S. Paul, S. Schider, and E. Gamsjäger, *Martensitic / Ferritic phase transformation of modern power plant steels*. Austria: https://youtu.be/aKM_EsZBLl8, 2014.

[107] E. Gamsjäger, J. Svoboda, and F. D. Fischer, “Austenite-to-ferrite phase transformation in low-alloyed steels,” *Comput. Mater. Sci.*, vol. 32, no. 3–4, pp. 360–369, 2005.

[108] NanoMEAGS, “ASTAR.” Nanomeags, Brussels, 2004.

[109] F. Abe, “Precipitate design for creep strengthening of 9% Cr tempered martensitic steel for ultra-supercritical power plants,” *Sci. Technol. Adv. Mater.*, vol. 9, no. 1, p. 13002, Jan. 2008.

[110] K. Kimura, “Creep Rupture Ductility Drop in the long-term of Creep Strength Enhanced Ferritic steels,” in *123HiMAT-2015*, 2015, pp. 110–113.

[111] W. Laux, *ZTA- und ZTU-Schaubilder für die Wärmebehandlung: Grundlagen und Anwendung*. 1977, p. 92.

[112] C. Capdevila, F. Caballero, and C. de Andrés, “Austenite grain size effects on isothermal allotriomorphic ferrite formation in 0.37 C-1.45 Mn-0.11 V microalloyed steel,” *Mater. Trans.*, vol. 44, no. 6, pp. 1087–1095, 2003.

[113] Y. J. Li, D. Ponge, P. Choi, and D. Raabe, “Segregation of boron at prior austenite grain boundaries in a quenched martensitic steel studied by atom probe tomography,” *Scr. Mater.*, vol. 96, pp. 13–16, 2015.

[114] E. I. Galindo-Nava and P. E. J. Rivera-Díaz-del-Castillo, “A model for the microstructure behaviour and strength evolution in lath martensite,” *Acta Mater.*, vol. 98, pp. 81–93, 2015.

[115] Y. Liu, S. Tsukamoto, K. Sawada, and F. Abe, “Role of Boundary Strengthening on Prevention of Type IV Failure in High Cr Ferritic Heat-Resistant Steels,” *Metall. Mater. Trans. A*, vol. 45, no. 3, pp. 1306–1314, Mar. 2014.

[116] K. BALAJIVA, R. M. COOK, and D. K. WORN, “Effects of Trace Elements on Embrittlement of Steels,” *Nature*, vol. 178, no. 4530, pp. 433–433, Aug. 1956.

[117] W. Zabil’skii, *Temper Embrittlement of Alloy Steels*, vol. 29. 100 Barr Harbor Drive, PO Box C700, West Conshohocken, PA 19428-2959: ASTM International, 1972.

[118] S. Pillot, C. Chauvy, S. Corre, L. Coudreuse, A. Gingell, D. Héritier, and P. Toussaint, “Effect of temper and hydrogen embrittlement on mechanical properties of 2,25Cr-1Mo steel grades - Application to Minimum Pressurizing Temperature (MPT) issues. Part II: Vintage reactors & MPT determination,” *Int. J. Press. Vessel. Pip.*, vol. 110, pp. 24–31, 2013.

[119] R. G. Ding, T. S. Rong, and J. F. Knott, “Phosphorus segregation in 2.25Cr1Mo steel,” *Mater. Sci. Technol.*, vol. 21, no. 1, pp. 85–92, 2005.

[120] B. Garbarz and B. Niżnik–Harańczyk, “Modification of microstructure to increase impact toughness of nanostructured bainite–austenite steel,” *Mater. Sci. Technol.*, vol. 31, no. 7, pp.

773–780, May 2015.

[121] W. et al Bleck, *Werkstoffprüfung in Studium und Praxis*, 15th ed. Aachen: Verlagshaus Mainz GmbH Aachen, 1999.

[122] S. F. and A. R. W., "Effect of Prior Austenite Grain Size on the Fracture Toughness Properties of A533 B Steel," in *The Physical Metallurgy of Fracture: Fourth International Conference on Fracture*, 1977, vol. 2, p. 6.

[123] I. Shakhova, A. Belyakov, Z. Yanushkevich, K. Tsuzaki, and R. Kaibyshev, "On Strengthening of Austenitic Stainless Steel by Large Strain Cold Working," *ISIJ Int.*, vol. 56, no. 7, pp. 1289–1296, 2016.

[124] Z. M. Shi, W. Gong, Y. Tomota, S. Harjo, J. Li, B. Chi, and J. Pu, "Study of tempering behavior of lath martensite using in situ neutron diffraction," *Mater. Charact.*, vol. 107, pp. 29–32, 2015.

[125] S. C. Kennett, G. Krauss, and K. O. Findley, "Prior austenite grain size and tempering effects on the dislocation density of low-C Nb-Ti microalloyed lath martensite," *Scr. Mater.*, vol. 107, pp. 123–126, 2015.

[126] C. Du, J. P. M. Hoefnagels, R. Vaes, and M. G. D. Geers, "Block and sub-block boundary strengthening in lath martensite," *Scr. Mater.*, vol. 116, pp. 117–121, 2016.

[127] I. Černý, D. Mikulová, J. Sís, B. Mašek, H. Jirková, and J. Malina, "Fatigue properties of a low alloy 42SiCr steel heat treated by quenching and partitioning process," *Procedia Eng.*, vol. 10, pp. 3310–3315, 2011.

[128] X. Liu and T. Fujita, "Effects of Austenitizing Conditions on Creep Rupture Properties of a 12Cr Heat Resisting Steel," *Tetsu-to-Hagane*, vol. 74, pp. 1065–1072, 1988.

[129] D. Raabe, M. Herbig, S. Sandlöbes, Y. Li, D. Tytko, M. Kuzmina, D. Ponge, and P. P. Choi, "Grain boundary segregation engineering in metallic alloys: A pathway to the design of interfaces," *Curr. Opin. Solid State Mater. Sci.*, vol. 18, no. 4, pp. 253–261, 2014.

[130] K. Kimura, N. Ohi, K. Shimazu, T. Matsuo, R. Tanaka, and M. Kikuchi, "Effect of prior austenite grain size on high temperature creep properties of Cr-Mo-V rotor steel," *Scr. Metall.*, vol. 21, no. 1, pp. 19–22, Jan. 1987.

[131] K. Maruyama, K. Sawada, and J. Koike, "Strengthening mechanisms of creep resistant tempered martensitic steel," *ISIJ Int.*, vol. 41, no. 6, pp. 641–653, 2001.

[132] A. Aghajani, C. Somsen, and G. Eggeler, "On the effect of long-term creep on the

microstructure of a 12% chromium tempered martensite ferritic steel," *Acta Mater.*, vol. 57, no. 17, pp. 5093–5106, 2009.

[133] Gustafson, "Coarsening of precipitates in an advanced creep resistant 9 % chromium steel — quantitative microscopy and simulations," *Mater. Sci. Eng. A*, vol. 333, pp. 279–286, 2002.

[134] M. I. Isik, A. Kostka, and G. Eggeler, "On the nucleation of Laves phase particles during high-temperature exposure and creep of tempered martensite ferritic steels," *Acta Mater.*, vol. 81, pp. 230–240, Dec. 2014.

[135] I. Holzer, *Modelling and Simulation of Strengthening in Complex Martensitic 9-12 % Cr Steel and a Binary Fe-Cu Alloy*, 2nd ed., no. May. Graz: Verlag d. Technischen Universität Graz, 2010.

[136] H. Cerjak, I. Holzer, P. Mayr, C. Pein, B. Sonderegger, and E. Kozeschnik, "The relation between microstructure and creep properties of martensitic 9-12 % Cr steels," *New Dev. Metall. Appl. High Strength Steels, 26.-28.5.2008*, pp. 247–263, 2008.

[137] T. Hasegawa, Y. Sakurai, and K. Okazaki, "Grain size effects on thermal recovery during high temperature deformation of aluminum tested at constant true strain rates," *Mater. Sci. Engng A*, vol. 346, pp. 34–41, 2003.

[138] F. J. Humphreys and M. Hatherly, *Recrystallization and Related Annealing Phenomena*. 2004.

[139] S. D. Yadav, M. Schuler, C. Sommitsch, and C. Poletti, "Physical Based Creep Strain Modelling of 9Cr Martensitic Steel," in *Proc.: Creep and Fracture in High Temperature Components: Design & Life Assessment Issues (ECCC)*, 2014.

[140] G. Miyamoto, R. Hori, B. Poorganji, and T. Furuhara, "Crystallographic analysis of proeutectoid ferrite/austenite interface and interphase precipitation of vanadium carbide in medium-carbon steel," *Metall. Mater. Trans. A Phys. Metall. Mater. Sci.*, vol. 44, no. 8, pp. 3436–3443, 2013.

9 Papers

9.1 Paper I

Type: Conference Proceedings, 2012, Thermec, Las Vegas, USA

DOI: 10.4028/www.scientific.net/MSF.783-786.1867

Title: Advanced Microstructures for Increased Creep Rupture Strength of MARBN Steels

Authors: Plesiutschnig E., Beal C., Paul S., Zeiler G., Mitsche S., Sommitsch C.

Abstract: Over the past three decades a lot of effort was made to optimize the chemical composition of 9% Cr martensitic steels, aiming to increase the operating temperature up to 923K and thus improving the efficiency of thermal power plants. Under these service conditions (high temperature and stress exposure), the creep strength of such steels is closely related to the long-term stability of their microstructure. The time to rupture can also be understood as an equivalent to the time of microstruc- ture deterioration. Optimization of the initial microstructure and understanding of the microstructure evolution during creep exposure are therefore decisive to improve the creep behavior of 9% Cr steels.

Selected chemical compositions of MarBN steels (Martensitic 9% Cr steels strengthened by Car- bides, Nitrides and Boron) were subjected to different heat treatments to produce an optimized microstructure to improve the creep rupture time. The initial microstructure before creep exposure was investigated using optical microscopy, SEM and EBSD. Short term creep rupture tests at 923K and 150MPa were performed, followed by systematic microstructure investigations.

Comparative EBSD investigations confirm an optimized microstructure for creep exposure, produced by an appropriate heat treatment. From comparative creep test results, it can be concluded that advanced microstructures increase the time to rupture of the selected MarBN steels by more than 10 percent, without reduction of the ductility.

9.2 Paper II

Type: Conference Proceedings, 2014, 10th Liège Conference on Materials for Advanced Power Engineering Liege, Belgium

Title: Microstructure for an optimized creep rupture strength of high Cr steels

Authors: Plesiutschnig E., Beal C., Paul S., Zeiler G., Mitsche S., Sommitsch C.

Abstract: Increasing the efficiency of modern steam power plants requires raising the inlet fluid temperature and pressure. To fulfill these conditions, the materials of cast, rolled and forged parts such as the case, pipes and rotor, need to be improved. Variations within the chemical composition of the material as well as appropriate processing steps are of crucial importance to meet an optimized microstructure for creep exposure. In this work, the influence of heat treatment on the microstructure of a MARBN and a modified FB2 steel was investigated. Systematic LOM, SEM and EBSD investigations were performed in order to characterize the microstructure before and after creep testing. Comparative creep tests carried out at 650°C show that, by applying appropriate heat treatment, creep rupture time can be increased by more than 100%.

9.3 Paper III

Type: Conference Proceedings, 2014, Power Gen Europe, Köln, Germany

Title: Turbine Components of High Creep Resistant MARBN Steels for Modern High Efficient Fossil-Fired Power Plants

Authors: Paul S., Zeiler G., Putschögl A., Plesiutschnig E.

Abstract: Sufficient energy availability in combination with lowest environmental pollution is a basic necessity for a high standard of living in each country. To guarantee this, power plants with improved technologies to achieve higher efficiency combined with reduced environmental impact are needed. The realization of this goal is not only a challenge for power station manufacturers, but also for manufacturers of special steels and forgings, which have to produce improved components with more advanced materials.

Böhler Special Steel is a full package supplier of high quality components for modern highly efficient power plants. The presentation shows our research activities in open die forging and materials development of high mechanical and temperature loaded components for power generation applications and reports about our experiences in the fabrication of forged components for gas and steam turbines. The highly creep resistant 10% Cr-steels used for these components are designed for operating temperature up to 625°C and were developed in the frame of the European Cost research program. Requirements for these components are excellent mechanical properties and ultrasonic detectability results. Additionally, our research activities on the latest generation of high temperature resistant steels for operating temperatures up to 650°C are shown – boron containing 9 % Cr martensitic steels (MARBN). Selected chemical compositions of MARBN steels were subjected to different heat treatments to produce an optimized microstructure. Creep exposure was investigated using optical microscopy, SEM and EBSD. Short term creep rupture tests at 650°C and 150 MPa were performed, followed by systematic microstructure investigations. From comparative creep test results, it can be concluded that advanced microstructures increase the time to rupture of the selected MARBN steels by more than 10 percent.

9.4 Paper IV

Type: Special Issue, 2015, Materials at High Temperatures

DOI: 10.1179/0960340914Z.00000000073

Title: Optimised microstructure for increased creep rupture strength of MarBN steels

Authors: Plesiutschnig E., Beal C., Paul S., Zeiler G., Sommitsch C.

Abstract: The efficiency of modern steam power plants relies heavily on the inlet fluid temperature and pressure. Thus, it is necessary to improve the materials of cast, rolled and forged parts such as case, pipes and rotor. Two chemical compositions of 9%Cr creep resistant steels were investigated. Different heat treatments were applied to modify the prior austenite grain size (to diameter of 50, 100, 300 and 700 μm) and to modify the substructure. The microstructure changes were further investigated by LOM, SEM and EBSD. Then, these different microstructures were exposed to the uniaxial creep rupture test at 650°C and 150 MPa. Comparative results reveal the influence of the modified microstructure on creep rupture time, ductility and fracture.

9.5 Paper V

Type: Conference Proceedings, 2015, 123HiMAT, Sapporo, Japan

Title: Investigations on the precipitation evolution of MarBN steels for microstructure based Life-Time assessments

Authors: Plesiutschnig E., Vujic S., Sommitsch C.

Abstract: Orowan strengthening of precipitates is one of the most effective ways to increase the creep resistance in 9% Cr steels. In a previous work, a forged MarBN steel was subjected to different heat treatments and creep rupture tests were carried out at 650°C and 150MPa. In the present work, microscopy investigations after heat treatment and creep exposure at 650°C and 150MPa are carried out using TEM and SEM to reveal the size distribution and the chemical composition of precipitates. The thermo-kinetic software MatCalc is used to calculate the precipitation evolution applying a multistage heat treatment and exposure for 25,000 hours at 650°C. Growth and coarsening of precipitates within their change in chemical composition is monitored considering a distinction between matrix precipitates and grain boundary precipitates. Local stress increase through cavity formation accompanied by the loss of Orowan strengthening due to coarsening of precipitates are the main reasons for the deterioration of creep rupture life.

9.6 Paper VI

Type: Journal Paper, 2016, Scripta Materialia

DOI: 10.1016/j.scriptamat.2016.05.033

Title: Ferritic phase transformation to improve creep properties of martensitic high Cr steels

Authors: Plesiutschnig E., Beal C., Sommitsch C., Paul S., Zeiler G.

Abstract: Creep properties of two 9% Cr steels, heat treated based on a quenching and partitioning concept are investigated. Austenite is partly transformed into martensite during interrupted quenching. Due to the new interfaces and the deformed retained austenite, it is possible to transform the retained austenite into ferrite and precipitates during subsequent tempering. The kinetics of this transformation is described by the Kolgomorov-Johnson-Mehl-Avrami equation. Creep rupture times are improved by more than 50% compared to conventional heat treated samples. It is expected that this heat treatment improves the creep properties of the entire class of 8–13% Cr steels.

9.7 Paper VII

Type: Conference Proceedings, 2016, Thermec, Graz, Austria

DOI: 10.4028/www.scientific.net/MSF.879.2100

Title: Dissimilar electron beam welds of nickel base alloy A625 with a 9% Cr-steel for high temperature applications

Authors: Wiednig C., Plesiutschnig E., Mitsche S., Beal C., Enzinger N., Lochbichler C.

Abstract: Welding of thick walled components with an electron beam has great potential due to the minimal heat input, high reproducibility and cost-efficiency. In the present work electron beam welding was used to weld 50mm thick plates of cast Ni-base alloy A625 to ferritic/martensitic 9% Cr steel plates. The welds were creep exposed at 625°C with stress levels ranging between 156 - 100MPa. Microstructure analysis of the weld-seam and the heat affected zone was carried out using metallography and scanning electron microscopy employing the EBSD technique to determine the location of the creep rupture. Creep fracture is located in the heat affected zone of the 9% Cr steel. Electron beam welded samples were compared to shield metal arc welded samples regarding welding and creep resistance. The performance and related microstructure properties of the electron beam welded specimen are more than competitive to conventional metal-arc-welding procedures.

9.8 Paper VIII

Type: Journal Paper (will be rewritten and submitted to Acta Materialia in 2017)

Title: Influence of the carbide solution on the austenite to ferrite transformation of a classic power plant steel

Authors: Plesiutschnig E., Mitsche S., Vujic S., Schlacher C., Sommitsch C., Paul S., Zeiler G.

Abstract: The austenite to ferrite phase transformation of martensitic high Cr containing steels is investigated to describe morphological changes during heat- treating and welding processes. Within these processes it is important to distinguish between the solution annealing temperature of precipitates and the ferrite to austenite transformation temperature. The aim of the present study is to illustrate the influence of the carbide solution on the austenite to ferrite or austenite to martensite transformation by subjecting a 13%Cr steel (AISI 420) to four deter- mined heat-treatment cycles. These cycles are used for comparative dilatometry, thermo-kinetic simulations and in-situ high temperature X-ray diffraction experiments. To analyse and compare the morphology with the related mechanical properties in as-received condition and after the heat treatments, different methods of scanning electron microscopy and standard hardness tests are used. If the carbides are not solved in the austenite matrix during austenitization, the critical cooling rate for martensite transformation is increased. This leads to the reconstructive austenite to ferrite transformation at Ar3 temperature, the displacement of the ferrite boundaries from the positions of the special carbides and to their coarsening. The results are discussed, compared and confirmed with investigations on the heat affected zone of a real steel weld in a 9%Cr steel (Grade 91). The consideration of this behaviour is important to understand the formation of the fine grain-, inter-critical heat affected zone and related mechanical and creep properties.

9.9 Paper IX

Type: Conference Proceedings, 2016, 8th International Conference on Advances in Materials Technology for Fossil Power Plants, Algarve, Portugal

Title: 9-10% Cr steel forgings for USC turbines – experiences in manufacturing and development status of MARBN steels

Authors: Zeiler G., Paul S., Plesiutschnig E.

Abstract: Sufficient energy availability in combination with lowest environmental pollution is a basic necessity for a high living standard in each country. To guarantee power supply for future generations, improved technologies to achieve higher efficiency combined with reduced environmental impact are needed. This challenge is not only aimed to the power station manufacturers, but also to the producers of special steel forgings, who have to handle with more and more advanced materials and complex processes.

Bohler Special Steel is a premium supplier of forged high quality components for the power generation industry. This paper reports about experiences in the fabrication of forged components for steam turbines for ultra-supercritical application - from basic properties up to ultrasonic detectability results. The materials used so far are the highly creep-resistant martensitic 9-10% Cr steel class for operating temperatures up to 625°C developed in the frame of the European Cost research program.

Additionally, our research activities on the latest generation of high temperature resistant steels for operating temperatures up to 650 degree Celsius – the boron containing 9% Cr martensitic steels (MARBN) - are discussed. In order to improve the creep behavior, MARBN steels with different heat treatments and microstructures were investigated using optical microscopy, SEM and EBSD. Furthermore, short term creep rupture tests at 650 degree Celsius were performed, followed by systematic microstructural investigations. As a result it can be concluded, that advanced microstructures can increase the time to rupture of the selected MARBN steels by more than 10 percent.